**Investigations on Void Formation in Composite Molding Processes and Structural Damping in Fiber-Reinforced Composites with Nanoscale Reinforcements**

Caleb Joshua DeValve

Dissertation submitted to the Faculty of the
Virginia Polytechnic Institute and State University
in partial fulfillment of the requirements for the degree of

Doctor of Philosophy
In
Mechanical Engineering

Ranga Pitchumani, Chair
Scott W Case
Mark R Paul
Shashank Priya
Pablo A Tarazaga

February 27, 2013
Blacksburg, Virginia

Keywords: fiber-reinforced composites, carbon nanotubes, analytical longitudinal permeability, void formation, material damping

**Investigations on Void Formation in Composite Molding Processes and Structural Damping in Fiber-Reinforced Composites with Nanoscale Reinforcements**

Caleb Joshua DeValve

## Abstract

Fiber-reinforced composites (FRCs) offer a stronger and lighter weight alternative to traditional materials used in engineering components such as wind turbine blades and rotorcraft structures. Composites for these applications are often fabricated using liquid molding techniques, such as injection molding or resin transfer molding. One significant issue during these processing methods is void formation due to incomplete wet-out of the resin within the fiber preform, resulting in discontinuous material properties and localized failure zones in the material. A fundamental understanding of the resin evolution during processing is essential to designing processing conditions for void-free filling, which is the first objective of the dissertation. Secondly, FRCs used in rotorcraft experience severe vibrational loads during service, and improved damping characteristics of the composite structure are desirable. To this end, a second goal is to explore the use of matrix-embedded nanoscale reinforcements to augment the inherent damping capabilities in FRCs.

The first objective is addressed through a computational modeling and simulation of the infiltrating dual-scale resin flow through the micro-architectures of woven fibrous preforms, accounting for the capillary effects within the fiber bundles. An analytical model is developed for the longitudinal permeability of flow through fibrous bundles and applied to simulations which provide detailed predictions of local air entrapment locations as the resin permeates the preform. Generalized design plots are presented for predicting the void content and processing time in terms of the Capillary and Reynolds Numbers governing the molding process.

The second portion of the research investigates the damping enhancement provided to FRCs in static and rotational configurations by different types and weight fractions of matrix-embedded carbon nanotubes (CNTs) in high fiber volume fraction composites. The damping is measured using dynamic mechanical analysis (DMA) and modal analysis techniques, and the results show that the addition of CNTs can increase the material damping by up to 130%. Numerical simulations are conducted to explore the CNT vibration damping effects in rotating composite structures, and demonstrate that the vibration settling times and the maximum displacement amplitudes of the different structures may be reduced by up to 72% and 50%, respectively, with the addition of CNTs.

## Acknowledgements

I give honor and praise to my lord and savior Jesus Christ, who has blessed me with the ability and determination that I have applied to complete the research contained in this dissertation. My advisor, Dr. Pitchumani, was instrumental in encouraging me to pursue my doctoral degree, and I am extremely thankful for his patient guidance and belief in me as a student. Helpful discussions and resources lent to me by Drs. Scott Case, Mark Paul, Pablo Tarazaga, and Shashank Priya were invaluable, and I am appreciative of their assistance and guidance. I could not have completed this degree without the support and love of my wife Keri, and I cannot thank her enough for standing behind me and my studies. I am also indebted to my parents and grandparents, who taught me how to live life to the fullest with a balance of discipline, hard-work, and fun. My parents-in-law, brothers, lab mates, and friends are a source of enjoyment and fulfillment, and I love spending time with them. I am indebted to each and every one of the aforementioned individuals, and I thank God daily for their presence and influence in my life.

**Table of Contents**

## List of Figures

**List of Tables**

**Chapter 1: Introduction**

This dissertation addresses several fundamental issues pertaining to composites technology, specifically void formation in composite molding processes and structural damping in fiber-reinforced composites with nanoscale reinforcements. First, a review of research involving the analytical modeling of the permeability of fibrous media is presented, along with a discussion of past research concerning the simulation of void formation in liquid composite molding (LCM) processes. An examination of the previous experimental and analytical studies regarding the damping behavior of fiber-reinforced composites with matrix-embedded CNTs is presented to complete the introduction in this chapter.

**1.1 Analytical Modeling of the Longitudinal Permeability of Aligned Fibrous Media**

Longitudinal fluid flow through an arrangement of aligned rigid cylindrical fibers occurs in most composite processing techniques including liquid molding processes. Resin flow through fiber tows during the resin infiltration stage of composite fabrication is often described as flow through a porous medium characterized principally by the fiber volume fraction and a permeability tensor. The permeability tensor can be constructed based on the transverse and longitudinal permeability of the aligned fiber bundle and the local orientation of the fiber bundle within the preform. Therefore, the evaluation of the transverse and longitudinal permeability of aligned rigid fibers has been the focus of many studies in the literature.

Fundamentally, the permeability of a porous fibrous medium is a geometric parameter and a measure of the resistance offered by the porous microstructure to the fluid flow as a function of the relative arrangement of the fibers, the fiber volume fraction, and the individual fiber radii. A comprehensive review of the previous analytical and experimental work on transverse and

longitudinal flow through aligned fibrous media is summarized in [1], from which, a few of the reviewed analytical longitudinal permeability models are reiterated here. An analytical solution for the transverse and longitudinal permeability of randomly packed fiber arrangements up to a fiber volume fraction of 0.7 was developed in [2]. Lubrication theory was used to predict transverse permeability values close to the fiber packing limit along with a simplified cell model to predict the transverse permeability at low fiber volume fractions in [3]. The longitudinal fluid flow problem was solved in [4] by simplifying the fluid boundary of the unit cell domain from a square to a circle, and an approximate solution for the flow was obtained. A solution for the pressure drop and the shear stress distribution along the fiber wall for longitudinal flow through aligned rigid fibers was developed in [5], and the method of distributed singularities was used in [6] to arrive at an approximate solution in the form of a power series.

In [7,8] the longitudinal permeability was solved for by modifying the fiber geometry based on the fiber packing arrangement, i.e., approximating the circular fibers as square in cross section for square packing and hexagonal in cross section for hexagonal packing. Other studies have proposed the superposition of three fundamental solutions which approximately satisfy the boundary conditions of the longitudinal flow configuration [9]. Fractal geometry was applied in [10,11] to characterize the dual-scale nature of flow through porous preforms in order to evaluate permeability values. In [12] the method of fundamental solutions was applied using a Stokeslet-based model and low Reynolds number flow to model the flow across an array of cylinders oriented transverse to the flow, where the results can be combined with Darcy's law to predict permeability values. A three-dimensional finite element model of a simplified plain weave unit cell was used to simulate the resin flow through a preform in [13], and an effective permeability based on the simulation results was reported. The research in [14] developed an analytical algorithm to

2

predict the transverse permeability of fiber tows considering the unsaturated flow length in the fiber perform.

A common method for experimentally determining the permeability of fibrous reinforcements is to physically force resin through a preform mat and monitor the pressure and flow rate throughout the mold, combining these results with Darcy's law or an empirically fit equation to determine the permeability of the preform as a function of the fiber volume fraction (e.g. [15–21]). A full review of these experimental methods for determining permeability was presented in [22], and this review also includes a short summary of the permeability prediction models documented in the literature. Experiments have demonstrated that the capillary forces within a fiber tow increase with an increase in fiber volume fraction (e.g. [23]), indicating the relative importance of including capillary effects in permeability calculations at high fiber volume fractions.

It is evident from the foregoing review that the analytical approaches in the literature are based on approximations of either the geometry or the governing flow physics, which leads to permeability values that substantially deviate from the actual values, particularly for arrangements with high fiber volume fraction. Chapter 2 of this dissertation presents an analytical series solution for the problem of fluid flow through aligned rigid fibers and, in turn, evaluation of the longitudinal permeability. The governing equations for the fluid flow in a representative volume element are solved using the separation of variables technique combined with a boundary collocation method [24,25], in which the boundary conditions are satisfied along the outside edges of the fluid domain at discrete points. Using this approach, the analytical results are shown to be in excellent agreement with a numerical finite element solution for rectangular and hexagonal packing arrangements of the fibers and for all fiber volume fractions, $v_f$. Chapter 2 presents the analytical model development and the permeability results in a dimensionless form as a function of

3

the fiber volume fraction and fiber packing arrangement, demonstrating a general applicability and easy use of the results for predicting the longitudinal permeability of fiber tows consisting of aligned rigid fibers

## 1.2 Simulation of Void Formation in Liquid Composite Molding Processes

It is well known that composite materials fabricated through liquid composite molding (LCM) processes and similar methods often exhibit defects from air entrapment during the resin infiltration process, leading to flaws in the resulting cured composite material such as potential failure locations and discontinuous material properties. These air voids undermine the property and performance benefits of fiber reinforced composites and are sought to be avoided during composites manufacturing. Air entrapment occurs during the preform infiltration step of LCM processes by virtue of the dual scale nature of the resin flow through and around the fiber tows in the preform. The resin flow is primarily influenced by the fiber preform geometry, mold complexity, and resin properties. In addition, the processing parameters imposed on the system, for example the vacuum pressure in vacuum assisted resin transfer molding (VARTM) and the injection flow rate in resin transfer molding (RTM), have a significant effect on the resin flow and consequently influence the relative size and location of the entrapped air voids in the resulting composite material.

The flow through fibrous preforms is effectively modeled as a porous medium and is fundamentally governed by the preform permeability, which is a measure of the resistance offered to the flow by the porous structure of the preform. Toward describing the flow in liquid molding processes, the model developed in Chapter 2 as well as numerous studies in the literature relate the transverse and longitudinal permeability of the porous structure to the fiber bundle volume fraction

and the fiber diameter for idealized rectangular and hexagonal packing arrangements of fibers within the tow bundles [1,3,6,26,27]. A detailed review of experiments and theoretical studies on low Reynolds number flow through fibrous porous media and the permeability relationships is presented in [22]. The infiltration of the resin into the fiber bundles is further affected by the capillary pressure at the resin flow front, which is fundamentally a function of the fiber bundle volume fraction, the individual fiber filament radius, and the surface tension and wetting angle of the infiltrating resin with respect to the fiber surface [28]. These effects are increasingly significant at the relatively high fiber bundle volume fractions generally found in the preform fabrics used as reinforcements in advanced composites [29].

A summary of the physics associated with modeling flow through porous media and a review of the advancements in numerical simulation tools used to model LCM processes in two- and three-dimensional geometries, including investigations concerned with micro- and macro-void prediction in fibrous preforms, are given in [30–32]. The formation of entrapped air locations is primarily the result of the dual-scale nature of the resin infiltration, consisting of flow through the macro-scale channels around the fiber bundles (the inter-tow regions) combined simultaneously with flow through the micro-scale pores within the fiber bundles (intra-tow regions) around the individual fibers [33]. Several techniques have been explored in the literature to model the resin infiltration and the consequent air entrapment in LCM and similar processes. Darcy's law was used in [34] to predict air entrapment within a cylindrical fiber bundle by considering resin flow radially inward in the fiber bundle cross-section and using an ideal gas assumption to determine the entrapped air volume within the bundle. This model was further developed to study the effect of varying the individual fiber diameter and number of fibers in each bundle on the resulting size of the entrapped air void within a single fiber bundle [35]. A similar study utilizing Darcy's law was

conducted to predict the void formation over time by using the finite element method to simulate resin flowing transversely over a fiber tow [36]. Darcy's law was also used in [37] to predict processing conditions that led to macro-void formation, and the results were presented as a function of the Capillary number. The model in [37] was extended to include the effects of injection pressure and distance from the mold inlet and the analytical predictions were validated experimentally [38]. Simplified cross-sections of various multi-layer woven fabrics were analyzed in [39] using a control volume to predict void formation. The Lattice Boltzmann Method was used to model air entrapment location and size considering transverse flow through arrays of square-packed fiber bundles when compared with similar experimental results [40]. Optimization of VARTM processing parameters based on dual-scale flow analysis was presented in [41] to minimize the void formation and mold fill time. In addition, a simulation of LCM processes was developed which considered the different permeabilities in the warp and weft directions as well as air bubble formation and migration, where the results were able to predict voids throughout the local zones of the flow domain as a function of the Capillary number [42].

The studies in the literature have focused primarily on simplified two-dimensional fiber preform geometries (e.g. [43]) or three-dimensional geometries described by a bulk permeability (e.g. [31]), whereas the flow in actual processing is both fully three-dimensional and contains multi-scale flow. Towards a realistic prediction of void entrapment during liquid molding processes, a numerical model is developed in Chapter 3 to describe resin permeation through a preform comprised of multiple layers of the plain weave fabric architecture. Considering flow through a three-dimensional unit cell and representative two-dimensional slices of the plain weave geometry, the analysis accounts for the capillary forces at the resin-air interface, and additionally, the effects of nesting between adjacent layers of fabric. Simulations are performed for a wide

6

range of the Capillary and Reynolds numbers in order to explore their individual effects on the location and relative size of air entrapment within the preform architecture. Based on the numerical simulation results, the effects of the resin flow conditions and preform parameters on the final void content and processing time are discussed in Chapter 3 along with the most favorable flow conditions for void minimization.

**1.3  Experimental Investigation of the Damping Enhancement from CNTs**

Fiber-reinforced composites offer a strong and lightweight alternative to traditional building materials and are increasingly being used across a broad spectrum of engineering applications, including aerospace structures, sports equipment, and wind turbines [44–46]. Composite materials used in such applications often suffer from vibrations caused by dynamic loads acting on the system, resulting in reduced efficiency and comfort, undesirable noise, and a shortened lifespan of the structure. Previous research has shown that various types of nano-scale fillers—such as carbon nanofibers, ceramic nanoparticles, and carbon nanotubes (CNTs)—can be incorporated into the composite matrix to enhanced the electrical, thermal, and mechanical properties of the material, including vibration damping augmentation [47–50]. In particular, the addition of CNTs to composite matrices has been found in several studies to provide significant damping enhancement to the material, allowing for the fabrication of composite structures with increased resistance to vibrations [51,52].

Carbon nanotubes as matrix-reinforcement have been the focus of the majority of composite nano-filler studies based upon their theoretical upper limit of specific strength, modulus, and conductivity [53]. Many reports concerning CNTs embedded in composite materials have noted evidence of a weak bond at the interface of the CNT-matrix, which undermines the mechanical and

7

conductive property benefits provided to the material by the CNTs [54,55]. Consequently, much work has been dedicated to investigating various surface treatments of CNTs in order to improve the bond between the CNT and composite matrix and better attain the valuable properties of the CNTs in the overall material [56–59]. However, this weak interfacial bond may alternatively be exploited to increase the damping in the composite material as a result of the stick-slip action which occurs at the CNT-matrix interface as the material is put under strain [60–62]. Numerous studies in the literature, as reviewed in [63], have focused on embedding CNTs in the matrix of composite materials for damping augmentation. Experimental measurements utilizing a thin film of CNTs grown by vapor deposition on a silica substrate have reported a 200% increase in
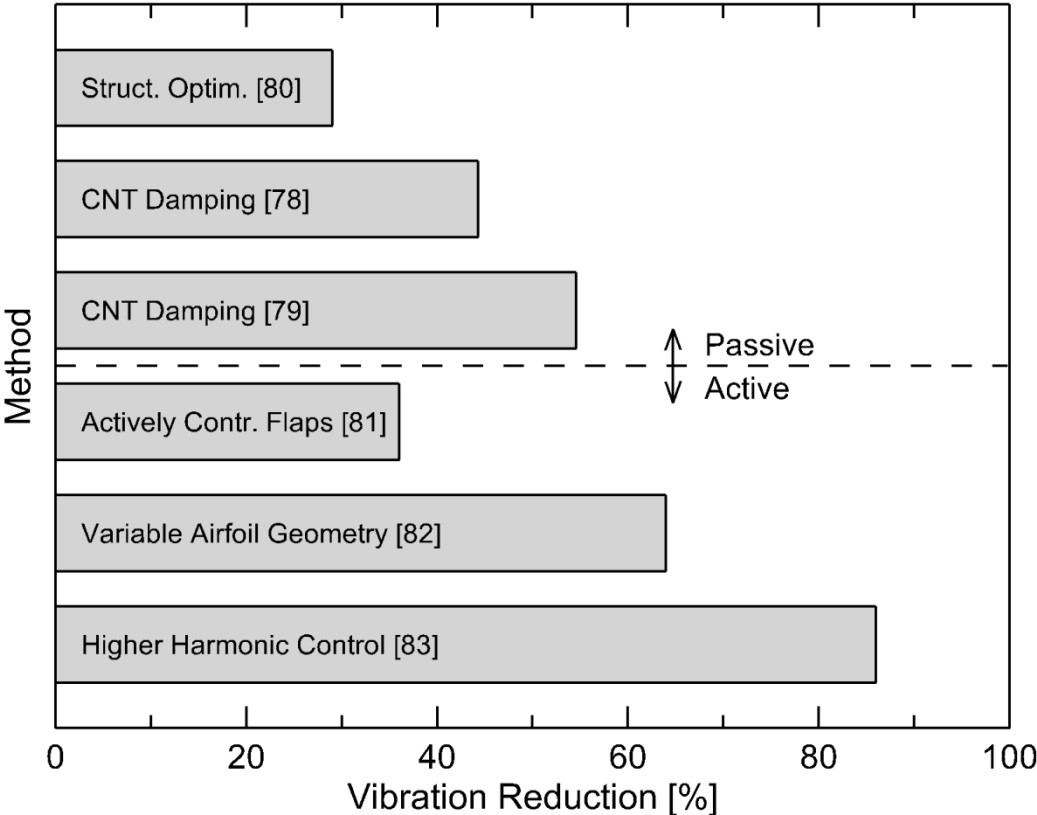


Figure 1: Comparison of the active and passive vibration control schemes used in rotor technology [80–83] and the damping effects of embedded carbon nanotubes [78,79] in fiber-reinforced composites

damping over the baseline system without nanotubes [64,65]. Active constrained layer damping (ACLD) treatments utilizing CNTs and sandwich beams with a CNT-epoxy core have demonstrated a damping increase of 40–1400% compared to the same beam fabricated without CNTs [66–71]. A 400–1100% augmentation in material damping was measured when CNTs were incorporated into the matrix of neat resin composites [52,55,60,61,72–75], and fiber reinforced composites with matrix-embedded CNTs have exhibited a damping increase of 50–130% [76–79].

Several of the aforementioned published studies in the literature have noted that passive CNT damping would benefit numerous applications which are currently made using composite materials and experience undesirable vibrations, notably rotating structures such as wind turbine blades and helicopter rotors. Although vibrations in rotating composite structures may be mitigated by other passive damping techniques (e.g. structural optimization [80]), these systems are predominantly controlled by active suppression methods including actively controlled flaps (ACF) [81], variable airfoil geometry [82], and the higher harmonic control (HHC) algorithm [83]. Figure 1 presents the vibration reduction achieved in various rotor blades by these different control schemes compared to the CNT damping studies in [78,79], where the vibration reductions achieved by active and passive techniques vary between 36–86% and 29–55%, respectively. It is evident from the data in Figure 1 that the vibration damping capability of CNTs is less than the active control techniques documented in [81–83]; however, matrix-embedded CNTs are integral to the structures and do not add any considerable weight or complexity to the system as with active control schemes. Therefore, CNT-based damping may be considered a viable passive damping mechanism to inherently augment the performance of rotating composite structures, with or without the use of additional active damping schemes, which serves as the motivation for the present study.

Although much work in the literature has focused on the damping characteristics of CNTs in composites, there has been a lack of emphasis on experimental studies of embedded CNTs in high fiber volume fraction composites, which are essential for achieving the necessary strength and modulus values for practical engineering structures. In addition, there is a need to experimentally explore the effects of CNT damping in a physical rotating composite beam in order to better understand how this CNT damping phenomenon may be exploited in rotating composites. Chapter 4 reports the results of an experimental study measuring the damping in CNT-reinforced composites as a function of strain, fiber volume fraction, and nanotube type and weight percentage loading, focusing on functional high fiber volume fraction composites in (1) a stationary frame, using DMA and modal analysis techniques, and (2) a rotating frame, to provide greater insight into passive CNT-damping capabilities in structures such as helicopter blades and wind turbine rotors.

## 1.4  Simulation of Rotating Composite Structures with CNT Damping

In order to characterize this CNT damping phenomena, several models have been proposed in the literature to describe the damping mechanism of the CNTs within the composite matrix. As discussed above, the additional damping provided by the CNTs in the composite may be explained in part by the poor bond that is exhibited between the surface of the CNTs and the surrounding composite matrix [84], resulting in energy dissipation through an interfacial stick-slip mechanism as these two surfaces slide over one another under strain [60,61,72,78]. A structural damping model for polymer composites containing single-walled carbon nanotubes (SWCNTs) was presented in [73], describing the energy dissipation using the assumption of stick-slip motion caused by friction between a debonded SWCNT and the surrounding resin. A similar study was developed in [62], which considered the nanotube-nanotube interactions as well as the interfacial

stick-slip action at the nanotube-matrix interface. A distributed CNT friction model which incorporated the spatial distribution of nanotubes using a statistical approach was established in [85], and reported a nonlinear relationship between the predicted damping and the applied excitation amplitude. In [72] a numerical simulation of CNTs embedded in an epoxy matrix was presented which explored the effects of various CNT orientations within the resin at different strain levels, applied to predict a material loss factor as a function of strain. Other approaches have modeled CNT damping using the Kelvin-Voigt model of nonlinear viscoelastic systems, where a closed form solution using this method is presented in [69]. A study concerning the effect of CNT-infused material coatings on the damping characteristics of a metal fan blade was developed in [74] using numerical simulations, where the results demonstrated an overall improvement in the blades modal characteristics when using the coating infused with CNTs.

In Chapter 5, the stick-slip damping model presented in [78] is applied along with viscous damping to investigate the effects of CNT-based damping on the dynamic response of a rotating composite beam. The model is developed using the dimensionless form of the Euler-Bernoulli equation and solved by means of the finite element method (FEM). The effect of rotation on the beam is considered by deriving the equations of motion in a rotating frame of reference and applying dynamic body forces that are dependent on the angular speed and acceleration experienced by the beam. The geometry is excited by a dimensionless angular speed profile related to the typical operating conditions of functional rotor blades [80–83,86,87], and the effects of CNT-based damping expressed in terms of coulomb and viscous damping parameters as well as the geometry and angular speed on the dynamic response of the rotating composite beam are explored in the results presented in Chapter 5.

11

Chapter 6 explores the effects of matrix-embedded CNTs in rotating composite structures using numerical simulations by applying empirical CNT-damping functions and the finite element method (FEM). Three different cantilevered composite structures of increasing complexity are studied: (1) a simple rectangular beam, (2) a helicopter rotor based on a Boeing VR7 airfoil [88], and (3) a wind turbine blade modeled according the theoretical NREL 5 MW wind turbine specifications [89]. A stick-slip damping mechanism described by the coulomb friction model is assumed to describe the CNT damping phenomena, and the damping in the composite structure considering only the fiber-matrix material (i.e. without CNT-reinforcement) is described with a viscous damping term [78]. The effect of rotation on the structure is modeled using a dynamic body force which is dependent on the angular speed and acceleration experienced by the structure, and the three geometries are excited by an angular speed profile specific to the typical operating conditions of each respective structure. Additionally, the relative geometric dimensions of each structure are varied to study their effect on each simulation case. The model development along with the effects of CNT damping, angular speed, and geometric variation on the dynamic response of different rotating composite structures are presented in Chapter 6.

**Chapter 2: Analytical Longitudinal Permeability Prediction of Aligned Rigid Fibers**

This chapter presents the analytical modeling of the longitudinal permeability of aligned rigid fiber bundles. Two different fiber bundle packing configurations are considered along with various fiber volume fractions, and the resulting permeability values are presented in dimensionless form for general applicability.

## 2.1 Modeling

The goal of the modeling in this chapter is to develop an analytical relationship between the longitudinal permeability, $\kappa$, and the governing geometric parameters for a porous medium comprised of a periodic arrangement of aligned rigid fibers. To this end, the problem of a viscous fluid flowing longitudinally through a bundle of aligned rigid fibers, presented schematically in Figure 2, is considered first. Two different fiber packing arrangements are analyzed, described as rectangular-packed or hexagonal fiber tows, shown, respectively, in Figure 2a and Figure 2b. By virtue of the symmetry of the fiber packing arrangements, the geometry can be simplified as a representative unit cell of width, $a$, height, $b$, and length, $L$, for each packing configuration with an associated fiber radius, $R$, and packing angle, $\delta$, as shown in Figure 2a and Figure 2b.

The flow is assumed to be laminar and the inertial forces are considered to be much less than the viscous forces, or equivalently, that the flow Reynolds number, $Re \ll 1$, such that the fluid motion is described by Stokes flow [90]. Further, for a fully-developed flow in the representative volume element, the pressure gradient in the direction of the flow can be expressed as $\frac{\partial P}{\partial z} = -\frac{\Delta P}{L}$, where $\Delta P$ is the pressure difference between the inlet and the outlet planes of the unit cell, and $L$ is the length of the unit cell in the flow ($z$-) direction. The governing equation can then be written in
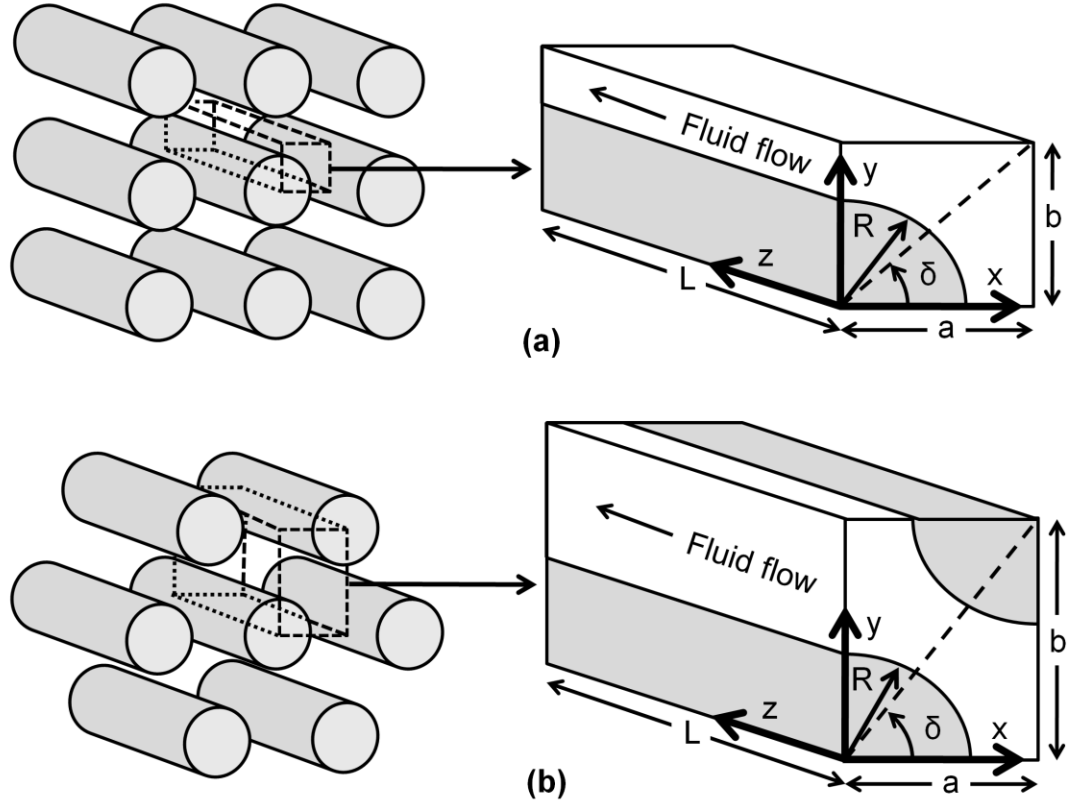
Figure 2: Schematic illustration of aligned fibers arranged in a (a) rectangular array and (b) hexagonal array, with the associated representative unit cell configurations and geometric parameters.

cylindrical polar coordinates, in a nondimensional form, as

$$\frac{1}{\bar{r}}\frac{\partial}{\partial\bar{r}}\left(\bar{r}\frac{\partial\bar{u}}{\partial\bar{r}}\right) + \frac{1}{\bar{r}^2}\frac{\partial^2\bar{u}}{\partial\theta^2} - 1 = 0 \qquad (1)$$

where, referring to Figure 2, all the unit cell parameters are normalized with respect to the fiber radius, $R$, as $\{\bar{a}, \bar{b}, \bar{x}, \bar{y}, \bar{r}\} = \{a, b, x, y, r\}/R$, $\theta$ is the angular coordinate and the dimensionless axial flow velocity, $\bar{u}$, is given by $\bar{u} = uL\mu/R^2\Delta P$, in which $u$ is the axial velocity in the $z$-direction along the fibers, and $\mu$ is the fluid viscosity.

Of the four boundary conditions needed to solve Equation 1 uniquely, three are identical for both the rectangular and the hexagonal fiber packing arrangements shown in Figure 2, namely, (1)

14

the fluid velocity at the fiber-fluid interface $(r = R)$ must satisfy the no-slip condition and the fluid shear stress must be zero (i.e. symmetry lines) along both (2) the bottom edge $(\theta = 0)$ and (3) the left edge $(\theta = \pi/2)$ of the unit cell. These conditions are defined mathematically in dimensionless form as:

$$\bar{u}(\bar{r} = 1, \theta) = 0 \tag{2}$$

$$\frac{\partial \bar{u}}{\partial \theta}(\bar{r}, \theta = 0) = 0 \tag{3}$$

$$\frac{\partial \bar{u}}{\partial \theta}\left(\bar{r}, \theta = \frac{\pi}{2}\right) = 0 \tag{4}$$

The fourth boundary condition is dependent on the fiber packing arrangement. For the rectangular-packed fiber arrangement shown in Figure 2a, the velocity field is symmetric about the boundary, $\bar{R}_b(\theta)$, where $\bar{R}_b(\theta) = R_b(\theta)/R$ denotes the dimensionless radial distance to the outer fluid boundary, $R_b(\theta)$, of the rectangular unit cell geometry defined by $\bar{x} = \bar{a}$ and $\bar{y} = \bar{b}$, as shown in Figure 3a, such that

$$\frac{\partial \bar{u}}{\partial \bar{x}}(\bar{x} = \bar{a}, \bar{y}) = \frac{\partial \bar{u}}{\partial \bar{y}}(\bar{x}, \bar{y} = \bar{b}) = 0 \tag{5}$$

For the hexagonal fiber arrangement presented in Figure 2b, the velocity field is symmetric with respect to the center of the unit cell along any line drawn through the central point $\left(\frac{\bar{a}}{2}, \frac{\bar{b}}{2}\right)$. Additionally, the gradient of the velocity field exhibits an anti-symmetry with respect to the central point $\left(\frac{\bar{a}}{2}, \frac{\bar{b}}{2}\right)$ along this same line. For simplicity, this line passing through the unit cell center, $\bar{R}_b(\theta)$, on which the two aforementioned boundary conditions are satisfied, is taken to be the diagonal line connecting points $(0, \bar{b})$ and $(\bar{a}, 0)$, as shown by the dashed line in Figure 3b. In this case, the boundary conditions are expressed mathematically in a dimensionless form as:

$$\bar{u}(\bar{R}_b(\theta_1)) = \bar{u}(\bar{R}_b(\theta_2)) \tag{6}$$
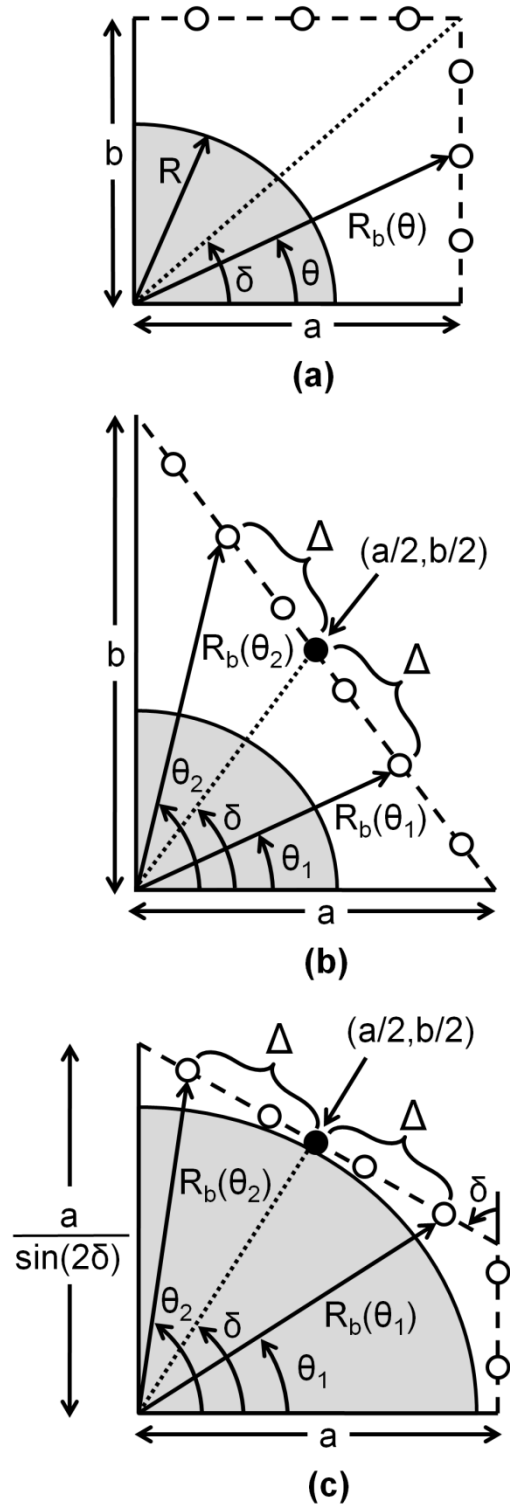
Figure 3: Schematic of the flow domain used in the analytical solution for a (a) rectangular array, (b) hexagonal array at low fiber volume fraction, and (c) hexagonal array at high fiber volume fraction. Also illustrated are the boundary collocation points, shown as open circles on the outer boundary for each unit cell configuration.

$$\frac{\partial \bar{u}}{\partial \bar{x}}\left(\bar{R}_b(\theta_1)\right) = -\frac{\partial \bar{u}}{\partial \bar{x}}\left(\bar{R}_b(\theta_2)\right) \qquad \frac{\partial \bar{u}}{\partial \bar{y}}\left(\bar{R}_b(\theta_1)\right) = -\frac{\partial \bar{u}}{\partial \bar{y}}\left(\bar{R}_b(\theta_2)\right) \qquad (7)$$

where

$$\bar{R}_b(\theta_i) = \bar{a}\frac{sin(\delta)}{sin(\delta + \theta_i)}, i = 1,2; \qquad \theta_2 = tan^{-1}\left[\frac{tan^2(\delta)}{tan(\theta_1)}\right] \qquad for\ \delta > \theta_1 > 0 \qquad (8)$$

Equivalently, the boundary conditions in Equations 6 and Equations 7 can be expressed by considering any two points on the boundary line defined through $\left(\frac{\bar{a}}{2},\frac{\bar{b}}{2}\right)$ which are on opposite sides of the center $\left(\frac{\bar{a}}{2},\frac{\bar{b}}{2}\right)$ and equidistant from this point, denoted by $\Delta$ in Figure 3b and Figure 3c, where, at these two points, the velocities are equal and the velocity gradients are equal in magnitude but opposite in sign.

As the fiber volume fraction, $v_f$, for the hexagonal unit cell is increased towards the fiber packing limit, the fiber will eventually intersect the diagonal dashed line defining the boundary in Figure 3b. For this configuration, it is necessary to modify the boundary, $\bar{R}_b(\theta)$, as shown by the dashed lines in Figure 3c, on which Equations 6 and Equations 7 are satisfied in order to ensure a continuous fluid presence along the outer edge of the unit cell. This is accomplished by defining the upper boundary to be a line drawn at an angle of $\delta$ from vertical, as indicated in Figure 3c, which passes through the unit cell center, $\left(\frac{\bar{a}}{2},\frac{\bar{b}}{2}\right)$, for which $\bar{R}_b(\theta_i), i = 1,2$; and $\theta_2$ are written as

$$\bar{R}_b(\theta_i) = \frac{\bar{a}}{2\big(cos(\delta)cos(\delta - \theta_i)\big)}, i = 1,2; \quad \theta_2 = 2\delta - \theta_1 \quad for\ \delta > \theta_1 > \begin{cases} 2\delta - \frac{\pi}{2} & if\ \delta > \frac{\pi}{4} \\ 0 & if\ \delta \leq \frac{\pi}{4} \end{cases} \qquad (9)$$

In addition, as a result of this boundary modification, a vertical line segment at $\bar{x} = \bar{a}$ becomes necessary to completely define the fluid domain boundary, on which the first part of Equation 5 is applied to complete the boundary condition specifications.

Expressing the dimensionless velocity as a superposition of two function, $f(\bar{r})$ and $g(\bar{r}, \theta)$, $\bar{u}(\bar{r}, \theta) = f(\bar{r}) + g(\bar{r}, \theta)$, it follows from Equation 1 and the associated boundary conditions, Equation 2–Equation 4, that

$$\frac{1}{\bar{r}} \frac{d}{d\bar{r}} \left( \bar{r} \frac{df(\bar{r})}{d\bar{r}} \right) + 1 = 0; \ f(\bar{r} = 1) = 0 \tag{10}$$

$$\frac{1}{\bar{r}} \frac{\partial}{\partial \bar{r}} \left( \bar{r} \frac{\partial g(\bar{r}, \theta)}{\partial \bar{r}} \right) + \frac{1}{\bar{r}^2} \frac{\partial^2 g(\bar{r}, \theta)}{\partial \theta^2} = 0 \begin{cases} g(\bar{r} = 1, \theta) = 0 \\ \frac{\partial g}{\partial \theta}(\bar{r}, \theta = 0) = \frac{\partial g}{\partial \theta}\left(\bar{r}, \theta = \frac{\pi}{2}\right) = 0 \end{cases} \tag{11}$$

Solving Equation 10 for $f(\bar{r})$ and using the method of separation of variables [91] to solve Equation 11 for $g(\bar{r}, \theta)$, the solution for $\bar{u}(\bar{r}, \theta)$ can be written as

$$\bar{u}(\bar{r}, \theta) = \underbrace{\frac{1}{4}(1 - \bar{r}^2) + C_0 \ln \bar{r}}_{f(\bar{r})} + \underbrace{\sum_{n=1}^{\infty} C_{2n}(\bar{r}^{2n} - \bar{r}^{-2n}) \cos(2n\theta)}_{g(\bar{r}, \theta)} \tag{12}$$

where $C_0, C_2, \cdots, C_{2n}$ are the coefficients to be determined using the boundary conditions, Equation 5–Equation 7, on the outer edge of the fluid domain, $\bar{R}_b(\theta)$, for each of the two fiber packing arrangements. The boundary conditions on $\bar{R}_b(\theta)$ were enforced using the boundary collocation method in which Equation 5–Equation 7 were satisfied at a finite number of discrete points chosen along the boundary of each of the domains depicted in Figure 3, resulting in a system of equations which were solved simultaneously to find the constants in Equation 12. Figure 3 illustrate this technique for rectangular and hexagonal arrangements of fibers, in which six boundary collocation points are shown by the open circles, excluding $(0, \bar{b})$ and $(\bar{a}, 0)$ and equally spaced to minimize the error in the resulting solution. In general, choosing $N$ discrete points to enforce the boundary conditions will result in $N$ equations to be solved concurrently for $C_0, \cdots, C_{2(N-1)}$ in Equation 12.

For the rectangular-packed unit cell in Figure 2a, using the relationships $\bar{r} = \sqrt{\bar{x}^2 + \bar{y}^2}$ and $\theta = tan^{-1}(\bar{y}/\bar{x})$, Equation 5 is converted to cylindrical polar coordinates as:

18

$$\frac{\partial \bar{u}}{\partial \bar{x}}(\bar{x}=\bar{a},\bar{y}) = \left(\frac{\partial \bar{u}}{\partial \bar{r}}\frac{\partial \bar{r}}{\partial \bar{x}} + \frac{\partial \bar{u}}{\partial \theta}\frac{\partial \theta}{\partial \bar{x}}\right)_{\bar{x}=\bar{a},\bar{y}} = 0 \Rightarrow$$

$$\bar{a}\left(\frac{C_0^R}{\bar{r}^2} - \frac{1}{2}\right) + \sum_{n=1}^{\infty} 2nC_{2n}^R \frac{\bar{a}}{\bar{r}^2}[(\bar{r}^{2n} + \bar{r}^{-2n})\cos(2n\theta) + (\bar{r}^{2n} - \bar{r}^{-2n})\sin(2n\theta)\tan\theta] = 0 \quad (13)$$

$$\frac{\partial \bar{u}}{\partial \bar{y}}(\bar{x},\bar{y}=\bar{b}) = \left(\frac{\partial \bar{u}}{\partial \bar{r}}\frac{\partial \bar{r}}{\partial \bar{y}} + \frac{\partial \bar{u}}{\partial \theta}\frac{\partial \theta}{\partial \bar{y}}\right)_{\bar{x},\bar{y}=\bar{b}} = 0 \Rightarrow$$

$$\bar{b}\left(\frac{C_0^R}{\bar{r}^2} - \frac{1}{2}\right) + \sum_{n=1}^{\infty} 2nC_{2n}^R \frac{\bar{b}}{\bar{r}^2}\left[(\bar{r}^{2n} + \bar{r}^{-2n})\cos(2n\theta) - (\bar{r}^{2n} - \bar{r}^{-2n})\frac{\sin(2n\theta)}{\tan\theta}\right] = 0 \quad (14)$$

where the coefficients in Equation 13 and Equation 14 are superscripted by R as $C_0^R$ and $C_{2n}^R$ to denote the rectangular-packing geometry. Using the boundary collocation method, Equation 13 and Equation 14 are evaluated at $N = 10$ discrete points along the top and right faces of the unit cell in Figure 3a for several values of the fiber volume fraction, $v_f$, and fiber packing angle, $\delta$, and the values of the coefficients $C_0^R, \cdots, C_{18}^R$ are presented in Table 1.

For the hexagonal fiber arrangement as in Figure 3b and the definitions in Equation 8 and Equation 9 mentioned above, Equation 6 and Equation 7 may be expressed as:

$$\frac{1}{4}\left(\bar{R}_b^2(\theta_2) - \bar{R}_b^2(\theta_1)\right) + C_0^S \ln\left(\frac{\bar{R}_b(\theta_1)}{\bar{R}_b(\theta_2)}\right)$$

$$+ \sum_{n=1}^{\infty} C_{2n}^S\left[\left(\bar{R}_b^{2n}(\theta_1) - \bar{R}_b^{-2n}(\theta_1)\right)\cos(2n\theta_1) - \left(\bar{R}_b^{2n}(\theta_2) - \bar{R}_b^{-2n}(\theta_2)\right)\cos(2n\theta_2)\right] = 0 \quad (15)$$

$$\sin\theta_1\left(\frac{C_0^S}{\bar{R}_b(\theta_1)} - \frac{\bar{R}_b(\theta_1)}{2}\right) + \sin\theta_2\left(\frac{C_0^S}{\bar{R}_b(\theta_2)} - \frac{\bar{R}_b(\theta_2)}{2}\right)$$

$$+ \sum_{n=1}^{\infty} 2nC_{2n}^S\left[\frac{\sin\theta_1}{\bar{R}_b(\theta_1)}\left\{\left(\bar{R}_b^{2n}(\theta_1) + \bar{R}_b^{-2n}(\theta_1)\right)\cos(2n\theta_1) - \left(\bar{R}_b^{2n}(\theta_1) - \bar{R}_b^{-2n}(\theta_1)\right)\frac{\sin(2n\theta_1)}{\tan\theta_1}\right\}\right.$$

$$+ \frac{\sin\theta_2}{\bar{R}_b(\theta_2)}\left.\left\{\left(\bar{R}_b^{2n}(\theta_2) + \bar{R}_b^{-2n}(\theta_2)\right)\cos(2n\theta_2) - \left(\bar{R}_b^{2n}(\theta_2) - \bar{R}_b^{-2n}(\theta_2)\right)\frac{\sin(2n\theta_2)}{\tan\theta_2}\right\}\right] = 0 \quad (16)$$

where the coefficients in Equation 15 and Equation 16 are superscripted by S as $C_0^S$ and $C_{2n}^S$ to denote the rectangular-packing geometry. As the packing limit is approached and the diagonal line

19

Table 1: First ten coefficients in Equation 12 for a rectangular fiber arrangement

| $\delta$ | $v_f$ | $C_0^R$ | $C_2^R$ (x $10^{-1}$) | $C_4^R$ (x $10^{-2}$) | $C_6^R$ (x $10^{-3}$) | $C_8^R$ (x $10^{-4}$) | $C_{10}^R$ (x $10^{-5}$) | $C_{12}^R$ (x $10^{-6}$) | $C_{14}^R$ (x $10^{-7}$) | $C_{16}^R$ (x $10^{-8}$) | $C_{18}^R$ (x $10^{-9}$) |
|---|---|---|---|---|---|---|---|---|---|---|---|
| | 0.10 | 0.637 | 0 | -3.13 | 0 | -13.2 | 0 | -49.4 | 0 | -175 | 0 |
| | 0.20 | 0.637 | 0 | -3.13 | 0 | -13.0 | 0 | -46.5 | 0 | -154 | 0 |
| | 0.30 | 0.637 | 0 | -3.10 | 0 | -12.2 | 0 | -34.0 | 0 | -63.2 | 0 |
| 45° | 0.40 | 0.637 | 0 | -3.02 | 0 | -10.1 | 0 | -1.44 | 0 | 175 | 0 |
| | 0.50 | 0.636 | 0 | -2.86 | 0 | -6.08 | 0 | 62.4 | 0 | 643 | 0 |
| | 0.60 | 0.636 | 0 | -2.62 | 0 | 0.277 | 0 | 161 | 0 | 1350 | 0 |
| | 0.70 | 0.636 | 0 | -2.29 | 0 | 8.29 | 0 | 270 | 0 | 2030 | 0 |
| | 0.79 | 0.638 | 0 | -1.94 | 0 | 15.3 | 0 | 321 | 0 | 1960 | 0 |
| | 0.10 | 0.909 | -1.21 | -3.10 | -4.24 | -8.59 | -13.8 | -25.2 | -35.4 | -40.0 | -24.3 |
| | 0.20 | 0.909 | -1.16 | -2.93 | -3.56 | -6.62 | -8.10 | -12.4 | -12.0 | -10.4 | -2.49 |
| 55°/35° | 0.30 | 0.909 | -1.09 | -2.64 | -2.40 | -3.04 | 2.49 | 12.4 | 34.1 | 49.1 | 41.1 |
| | 0.40 | 0.908 | -0.997 | -2.25 | -0.792 | 2.24 | 18.4 | 50.9 | 106 | 144 | 110 |
| | 0.50 | 0.908 | -0.891 | -1.78 | 1.17 | 8.88 | 38.4 | 99.2 | 196 | 260 | 193 |
| | 0.54 | 0.910 | -0.840 | -1.56 | 2.05 | 11.8 | 46.9 | 119 | 232 | 307 | 224 |
| | 0.10 | 1.366 | -3.02 | -4.22 | -5.73 | -8.27 | -10.7 | -11.4 | -9.00 | -4.62 | -1.15 |
| 65°/25° | 0.20 | 1.358 | -2.82 | -3.48 | -3.60 | -3.46 | -2.43 | -0.878 | 0.362 | 0.576 | 0.221 |
| | 0.30 | 1.345 | -2.54 | -2.43 | -0.514 | 3.59 | 9.88 | 14.9 | 14.4 | 8.40 | 2.29 |
| | 0.36 | 1.341 | -2.34 | -1.66 | 1.74 | 8.76 | 18.9 | 26.5 | 24.8 | 14.2 | 3.83 |

$C_1^R, C_3^R, C_5^R, C_7^R, C_9^R, C_{11}^R, C_{13}^R, C_{15}^R, C_{17}^R, C_{19}^R = 0$

Table 2: First ten coefficients in Equation 12 for a hexagonal fiber arrangement

| $\delta$ | $v_f$ | $C_0^S$ | $C_2^S$ (x $10^{-4}$) | $C_4^S$ (x $10^{-4}$) | $C_6^S$ (x $10^{-3}$) | $C_8^S$ (x $10^{-5}$) | $C_{10}^S$ (x $10^{-5}$) | $C_{12}^S$ (x $10^{-6}$) | $C_{14}^S$ (x $10^{-7}$) | $C_{16}^S$ (x $10^{-8}$) | $C_{18}^S$ (x $10^{-9}$) |
|---|---|---|---|---|---|---|---|---|---|---|---|
| | 0.10 | 0.551 | -0.921 | -0.701 | -8.46 | -3.89 | -3.13 | -89.2 | -105 | -254 | -815 |
| | 0.20 | 0.551 | -0.893 | -0.667 | -8.46 | -3.79 | -3.05 | -88.6 | -102 | -251 | -813 |
| | 0.30 | 0.551 | -0.604 | -0.444 | -8.44 | -2.73 | -2.20 | -81.3 | -76.2 | -213 | -785 |
| | 0.40 | 0.551 | 0.813 | 0.524 | -8.35 | 2.51 | 1.99 | -44.5 | 53.9 | -23.6 | -639 |
| 60°/30° | 0.50 | 0.552 | 5.31 | 3.40 | -8.03 | 19.3 | 15.7 | 76.8 | 481 | 585 | -191 |
| | 0.60 | 0.554 | 19.4 | 11.9 | -7.10 | 72.5 | 59.9 | 454 | 1930 | 3230 | 2330 |
| | *0.70* | *0.551* | *-0.0696* | *-0.0301* | *-7.37* | *-16.2* | *-18.4* | *149* | *-12.7* | *-61.4* | *14300* |
| | *0.80* | *0.551* | *0.0658* | *0.0338* | *-6.39* | *18.1* | *14. 5* | *327* | *6.32* | *27.4* | *22700* |
| | *0.90* | *0.551* | *0.997* | *0.378* | *-5.13* | *1.90* | *1.95* | *452* | *117* | *542* | *9690* |
| | 0.10 | 0.875 | -1100 | -276 | -4.79 | -67.8 | -13.8 | -20.2 | -26.3 | -24.1 | -9.18 |
| | 0.20 | 0.874 | -1070 | -263 | -4.51 | -61.6 | -14.0 | -24.3 | -38.1 | -40.3 | -17.6 |
| 70°/20° | 0.30 | 0.871 | -1020 | -243 | -4.07 | -53.2 | -15.3 | -35.0 | -65.9 | -75.8 | -34.8 |
| | 0.40 | 0.868 | -965 | -217 | -3.42 | -41.6 | -17.6 | -52.0 | -110 | -130 | -59.7 |
| | 0.50 | 0.862 | -905 | -188 | -2.68 | -31.1 | -22.4 | -80.6 | -180 | -213 | -96.6 |
| | *0.57* | *0.875* | *-771* | *-122* | *0.487* | *120* | *37.6* | *98.8* | *179* | *217* | *137* |
| | 0.10 | 1.832 | -4490 | -447 | -4.32 | -36.3 | -2.28 | -0.982 | -0.267 | -0.0405 | -0.00258 |
| 80°/10° | 0.20 | 1.711 | -4520 | -431 | -3.96 | -31.9 | -1.93 | -0.803 | -0.209 | -0.0294 | -0.00165 |
| | *0.27* | *1.620* | *-4412* | *-388* | *-3.24* | *-24.9* | *-1.57* | *-76.4* | *-0.266* | *-0.0587* | *-0.00628* |

$C_1^S, C_3^S, C_5^S, C_7^S, C_9^S, C_{11}^S, C_{13}^S, C_{15}^S, C_{17}^S, C_{19}^S = 0$
*Rows with italicized numbers indicate solution for the modified boundary, as shown in Figure 3c

through the unit cell center is modified as discussed previously and illustrated in Figure 3c, the additional boundary on the right face of the unit cell where $\bar{x} = \bar{a}$ will be satisfied by applying Equation 13. Table 2 presents the values of the coefficients $C_0^S, \cdots, C_{18}^S$ calculated using the boundary collocation method with $N = 10$ discrete boundary points for several values of the fiber volume fraction, $v_f$, and fiber packing angle, $\delta$.

Using Darcy's law [26], the longitudinal permeability can be related to the average velocity through the cross section of the fluid region in the unit cell, the fluid viscosity, and the pressure gradient as $\kappa = \mu L u_{avg}/\Delta p$, from which the dimensionless permeability, $\bar{\kappa} = \frac{\kappa}{R^2}$, is obtained as

$$\bar{\kappa} = \bar{u}_{avg} = \frac{\int_0^{\pi/2} \int_1^{\bar{R}_b(\theta)} \bar{u}(\bar{r},\theta)\,\bar{r}\,d\bar{r}\,d\theta}{\int_0^{\pi/2} \int_1^{\bar{R}_b(\theta)} \bar{r}\,d\bar{r}\,d\theta} \qquad (17)$$

where the numerator denotes the dimensionless volumetric flow rate and the denominator is the dimensionless cross sectional area of the fluid region of the unit cell equaling $\left(\bar{a}\bar{b} - \frac{\pi}{4}\right)$ for the rectangular packing as in Figure 2a and $\left(\frac{\bar{a}\bar{b}}{2} - \frac{\pi}{4}\right)$ for the hexagonal fiber arrangement as in Figure 2b. In Equation 17 the velocity profile, $\bar{u}(\bar{r},\theta)$, is given by Equation 12 and the associated coefficients tabulated in Table 1 and Table 2. Equation 17 was evaluated using a computational quadrature method to determine the dimensionless permeability as a function of the volume fraction, $v_f$, and the fiber packing angle, $\delta$, for the two packing arrangements considered in this dissertation, where the results are presented below.

## 2.2 Results and Error Estimation

The analytical model presented in the previous section was compared to three-dimensional numerical simulations of the fluid flow through identical rectangular and hexagonal unit cell
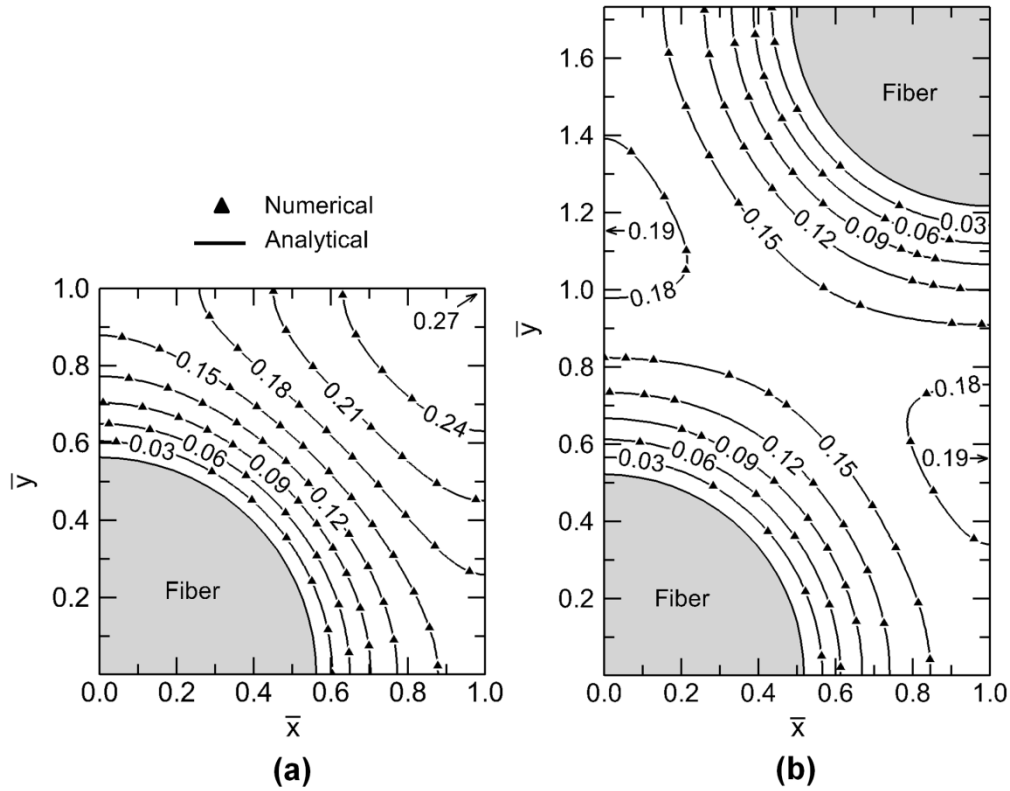
Figure 4: Contour plots of the dimensionless velocity in unit cells of a (a) rectangular fiber arrangement with $v_f = 0.25$ and $\delta = 45°$ and (b) hexagonal fiber arrangement with $v_f = 0.25$ and $\delta = 60/30°$.

geometries (as shown in Figure 2) for a range of fiber volume fractions and fiber packing angles. The numerical solution was obtained with the commercially available finite element software COMSOL$^©$ using a tetrahedral mesh consisting of $2 \times 10^4$ elements, and the results were non-dimensionalized according to the parameters presented in Chapter 2.1 in order to compare the numerical results to the dimensionless analytical series solution. The results of the comparison are presented and discussed in this chapter. Figure 4 presents contours of the dimensionless velocity profiles evaluated using the analytical solution in a rectangular unit cell geometry with a fiber packing angle of 45° (Figure 4a) and a hexagonal unit cell geometry with a fiber packing angle of 60° (Figure 4b), both with a fiber volume fraction of 0.25. The analytical solution is based on ten

boundary collocation points in the evaluation of the boundary conditions, Equation 6 and Equation 7, using the constants given in Table 1 and Table 2 in Equation 12. Also included in the figures are the dimensionless velocity profile values obtained from a numerical fluid dynamics simulation of the flow through the respective geometries, shown by the discrete triangular markers in the figures.

Excellent agreement is noted between the analytical solution and the corresponding numerical solution. For the rectangular fiber arrangement in Figure 4a, the maximum dimensionless velocity is approximately 0.27 and located at the upper right-hand corner of the fluid domain. At the same volume fraction, the hexagonal-packed case in Figure 4b shows a smaller maximum dimensionless velocity of approximately 0.19 to occur at the points (0,1.16) and (1,0.57) in the unit cell. From Figure 4, it is also evident that the maximum velocity locations for each fiber packing arrangement are situated on the fluid boundary at the furthest distance from the fiber surfaces in their respective unit cell domains. It follows from the dimensionless velocity profiles that the dimensionless volumetric flow rate through the rectangular fiber packing geometry is greater than the hexagonal fiber arrangement at the same fiber volume fraction. Since the results are presented in dimensionless form, the velocity profiles are generally applicable to longitudinal flow situations through aligned rigid fibers without limitation on the fiber radius or fluid viscosity. In addition, the qualitative relative trends in the flow behavior for the two unit cell geometries are generally applicable throughout the entire range of fiber volume fractions and packing angles.

The results in Figure 4 were based on ten collocation points on the boundaries of the rectangular and hexagonal unit cells in Figure 3, which, in turn, governs the number of terms used in evaluating the series solution in Equation 12. It is instructive to assess the influence of the number of boundary collocation points—and, in turn, the number of terms in Equation 12—on the accuracy of the analytical solution. To this end, Figure 5 presents the magnitude of the error in
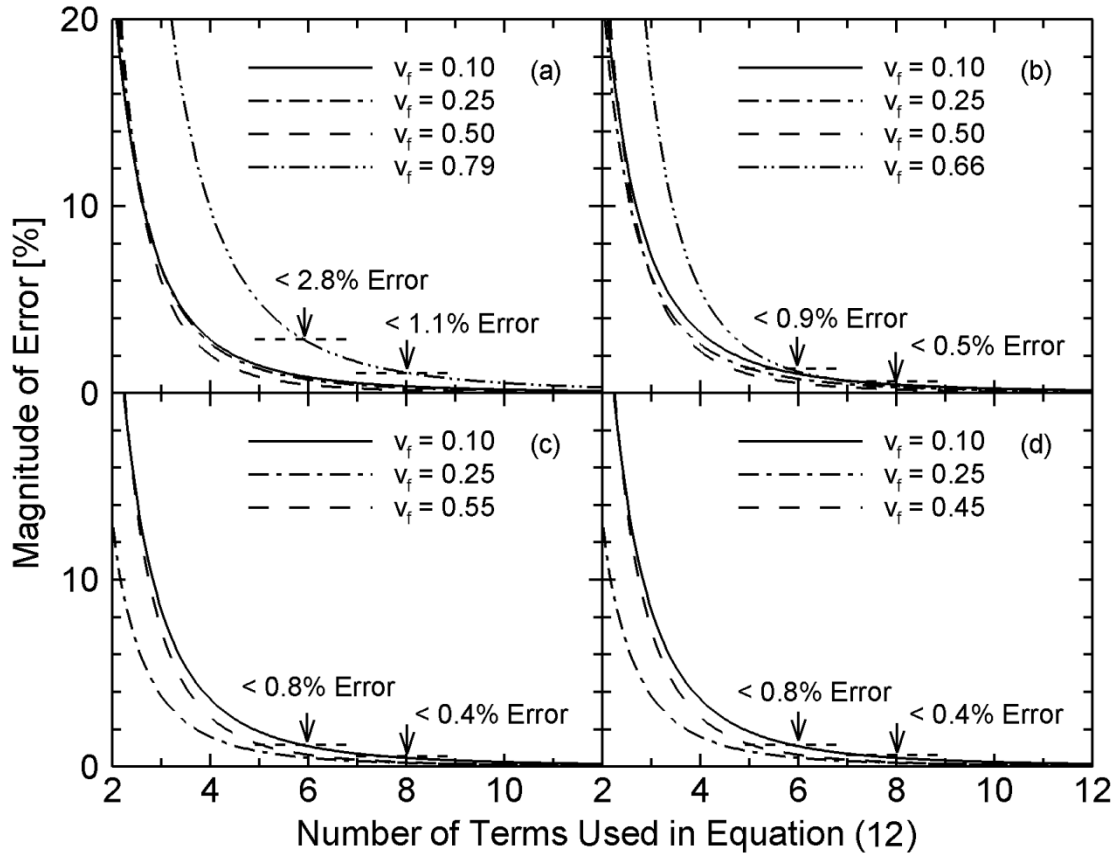
Figure 5: Variation of the error between the numerical and analytical solutions for flow rate through a rectangular fiber array at different fiber volume fractions as the number of terms in Eq. 12 is varied; for (a) $\delta = 45°$, (b) $\delta = 50°/40°$, (c) $\delta = 55°/35°$, and (d) $\delta = 60°/30°$.

the analytical solution of the volumetric flow rate for the rectangular fiber arrangement in comparison to the converged numerical solution of the volumetric flow rate, expressed as a percentage of the numerical solution, as the number of coefficients determined in Equation 12 is increased. The numerical finite element method (FEM) was used to validate the analytical solution since FEM is usually employed in detailed computational modeling of this flow situation and serves as an appropriate basis for comparison with the analytical results. The error magnitudes are presented at incremented values of the volume fraction, $v_f$, and at four different values of the packing angle, $\delta$, (Figure 5a–Figure 5d) as noted in the figure caption. The maximum attainable

volume fraction at the packing limit decreases as the packing angle is increased, which can be seen from inspection of the unit cell's geometry and is reflected in the different values of the volume fraction upper limits as the packing angle is changed, presented in the legend of Figure 5. In general, Figure 5 shows that as the number of terms in the expansion of Equation 12 is increased, the accuracy of the analytical solution increases accordingly and the error with respect to the converged numerical solution approaches zero.

It is apparent from Figure 5a that for a rectangular packing angle of $\delta = 45°$, the error remains less than about 2.8% when at least six terms are included in the expansion of Equation 12 and further reduces to less than ~1% when the number of terms is increased to eight. The relatively greater amount of error apparent in the case where $v_f = 0.79$ and $\delta = 45°$ (Figure 5a) when
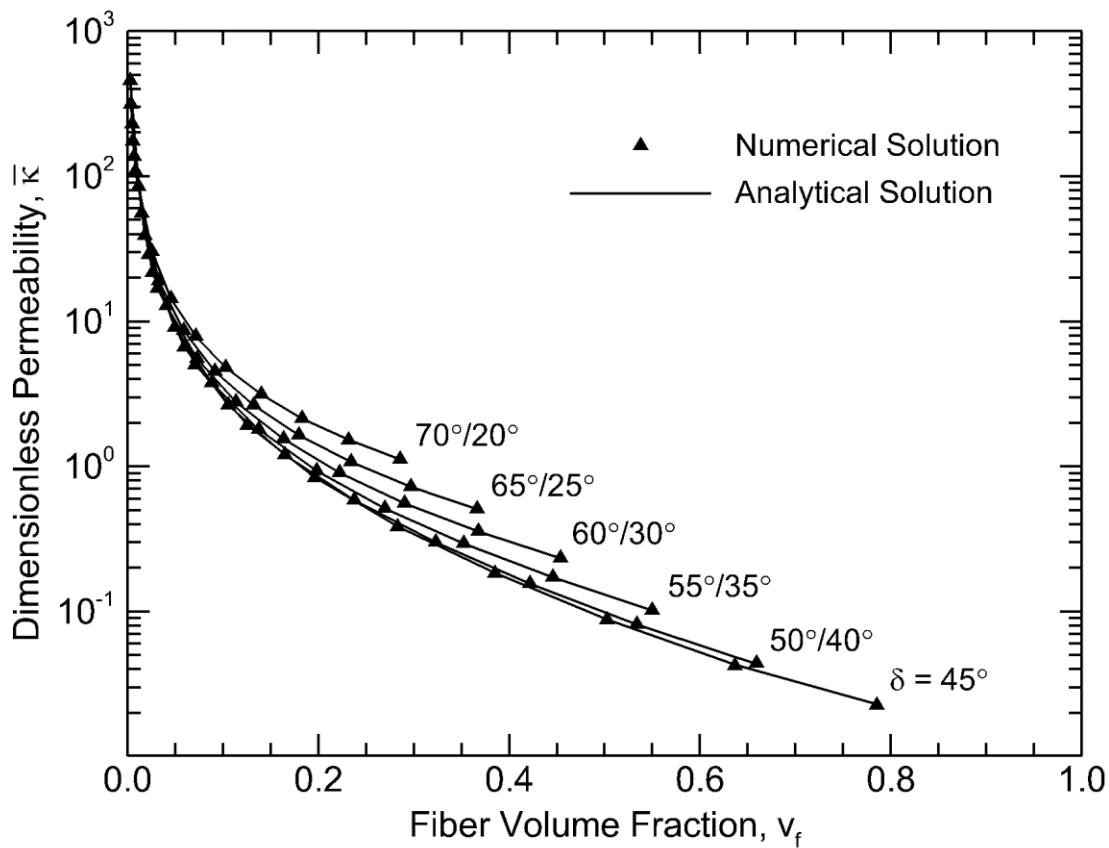


Figure 6: Variation of the dimensionless permeability with the fiber volume fraction and fiber packing angle for a rectangular arrangement of fibers.

compared to the other cases is due to the presence of narrow fluid regions at either side of the unit cell which occur as a result of the unit cell geometry approaching the fiber packing limit. Figure 5b–Figure 5d indicate that for packing angles other than 45°, the error is less than 0.9% and 0.5% with the inclusion of six and eight terms, respectively. In general, the error variations in Figure 5 demonstrate that by including ten terms in the expansion of Equation 12, a highly accurate solution for the flow rate through the unit cell can be found throughout the ranges of the geometrical parameters involved, including conditions approaching and equal to the fiber packing limits. The error in the solution of Equation 12 using a hexagonal packing arrangement of the fibers is similar to the trends presented in Figure 5 and is omitted for brevity.

The variation of the dimensionless longitudinal permeability, $\bar{\kappa}$, with the fiber volume fraction, $v_f$, for rectangular fiber arrangements with different packing angles is depicted in Figure 6. The figure shows the analytical solution obtained from Equation 17 with ten boundary collocation points and using the coefficients in Table 1, as solid lines, which is compared with the numerical finite element solution presented as the discrete triangular symbols. The designation of two angles for the different lines in Figure 6 other than $\delta = 45°$ represents the fact that either packing angle results in the same dimensionless fluid flow rate and therefore the same dimensionless permeability value. In general, it is noted that the dimensionless permeability decreases with increasing fiber volume fraction, owing to the resulting increase in the flow resistance. Furthermore, for any given fiber volume fraction, the permeability is the lowest for the packing angle of 45°, again signifying the greatest flow resistance for this packing configuration. It is seen in Figure 6 that the packing angle of 45° allows the maximum fiber volume fraction of 0.785 to be attained, which results in the least dimensionless permeability of approximately $2.31 \times 10^{-2}$.
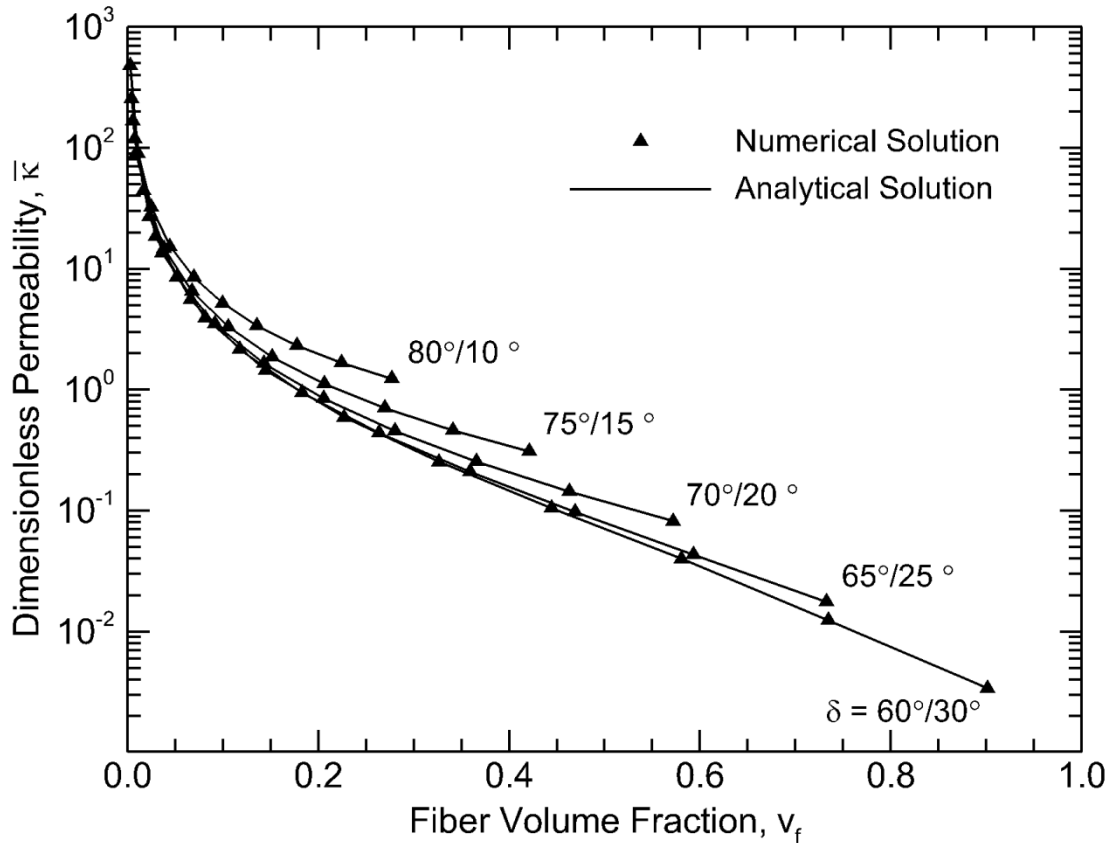
Figure 7: Variation of the dimensionless permeability with the fiber volume fraction and fiber packing angle for a hexagonal arrangement of fibers.

Similar trends in the dimensionless permeability variation with fiber volume fraction and fiber packing angle were found for the hexagonal fiber arrangement, as presented in Figure 7. As in Figure 6, the discrete triangular markers denote the numerical finite element solution and the solid lines represent the analytical solution from Equation 17 based on 10 boundary collocation points using the coefficients in Table 2. Two different packing angles are shown for each line to signify that the identical dimensionless flow rates are found by applying either of the packing angle values. For the hexagonal fiber arrangement, the highest volume fraction attainable is 0.907 at a packing angle of 60°/30°, where the corresponding dimensionless permeability value is

approximately $3.26 \times 10^{-3}$, which is approximately an order of magnitude lower than the minimum permeability noted for the rectangular packing in Figure 6.

In both Figure 6 and Figure 7, excellent agreement is seen between the analytical results and the numerical values. It is evident from a comparison of the permeability values in Figure 6 and Figure 7 that at any fiber volume fraction, the rectangular fiber packing offers less resistance to the fluid flow than the hexagonal fiber arrangement, which is reflected in the higher dimensionless permeability value for the rectangular fiber arrangement. This difference is particularly pronounced at higher fiber volume fractions and reduces as the fiber volume fraction decreases, where the smallest tested fiber volume fraction of $1 \times 10^{-3}$ resulted in the dimensionless permeability values converging to the same value of approximately 450 for all cases of the different relative fiber arrangements.

The longitudinal permeability values presented in Figure 6 and Figure 7 can be compared to experimental results reported in the literature to evaluate the accuracy of the analytical results compared to physical measurements. An experiment measuring the longitudinal permeability of an array of aligned cylinders was presented in [20], reporting a dimensionless permeability on the order of $10^{-2}$ for a hexagonal fiber arrangement with a volume fraction of 0.6. Considering the results presented in Figure 7 for a hexagonal fiber arrangement, it is evident that at $v_f = 0.6$ the analytical solution also predicts a permeability on the order of $10^{-2}$ and therefore exhibits good agreement with the experimentally measured value in [20]. In addition, the study in [23] examined a fiber tow made up of glass filaments with a diameter of 12 $\mu m$ and experimentally measured the dimensionless longitudinal permeability to be on the order of $10^{-2}$ for a fiber volume fraction of 0.6, which is on the same order of magnitude as the measurements in [20] and the analytical results presented in Figure 6 and Figure 7.

As the fiber volume fraction of the fiber tow is increased, the effects of capillary pressure will become increasingly significant in permeability measurements and predictions (e.g. [23,28]). According to [28], the capillary pressure, $P_{cap}$, in the longitudinal direction of aligned rigid fibers can be expressed in terms of the fiber volume fraction, $v_f$, fiber radius, $R$, surface tension, $\gamma$, and contact angle, $\sigma$, as: $P_{cap} = \frac{v_f}{1-v_f} \frac{2\gamma cos(\sigma)}{R}$. In a typical liquid composite molding process the surface tension will be on the order of $10^{-2}$ N/m, the contact angle will be on the order of 10 degrees, and the fiber radius will be on the order of $10^{-5}$ m. Applying the above expression to a fiber tow with a volume fraction of 0.8 results in a capillary pressure of approximately 8 kPa. The applied pressure in a liquid composite molding application is typically on the order of $10^2$ kPa, which is more than an order of magnitude higher than the capillary pressure calculated in the previous scenario. Therefore, reasonable accuracy should be expected when using the permeability values presented in Figure 6 and Figure 7, however these results should be used carefully when applied to situations involving fiber tows with small filament diameters and high fiber volume fractions where the capillary effect may become increasingly significant. The model developed in this chapter along with an established transverse permeability model are applied to describe the local permeability tensor of a woven preform fabric used in the numerical simulation of void formation in LCM processes presented in Chapter 3.

## 2.3 Nomenclature used in Chapter 2

a      width of unit cell [$m$]

b      height of unit cell [$m$]

C      Equation 12 constants

L      length of unit cell [$m$]

N       number of boundary collocation points

P       pressure [$Pa$]

r       radial-direction coordinate [$m$]

R       fiber radius [$m$]

$R_b$   radius to flow boundary [$m$]

Re      Reynolds number

**u**   velocity vector [$m/s$]

$v_f$   fiber volume fraction

x       x-direction coordinate [$m$]

y       y-direction coordinate [$m$]

z       z-direction coordinate [$m$]


*Greek symbols*

$\gamma$    surface tension [$N/m$]

$\delta$    fiber packing angle [$degrees$]

$\theta$    angular-direction coordinate [$degrees$]

$\kappa$    permeability [$m^2$]

$\mu$       fluid viscosity [$Pa \cdot s$]

$\sigma$    contact angle [$degrees$]


*Superscripts/subscripts*

$^{-}$      dimensionless value

$^{R}$      rectangular fiber packing

$^{S}$      hexagonal fiber packing

$_{2n}$     index of constants in solution equation

**Chapter 3:  Numerical Simulation of Void Formation in LCM Processes**

This chapter presents a numerical simulation of the resin evolution through a fibrous preform during a liquid composite molding (LCM) process. Based on the studies, a generalized paradigm is illustrated for predicting the void content as a function of the Capillary and Reynolds numbers governing the materials and processing, along with the most favorable conditions for minimizing air entrapment during processing.

**3.1  Modeling**

The geometry considered in the current study consists of a unit cell of length *l*, containing
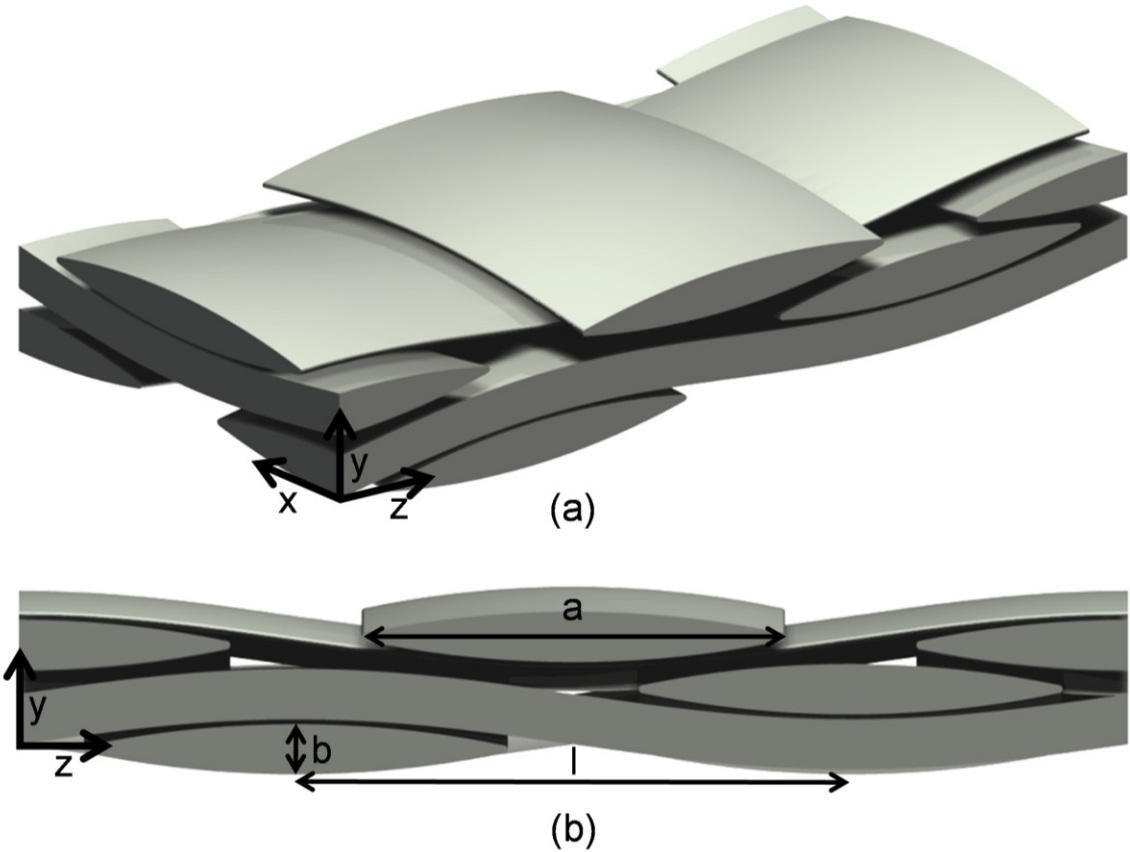
Figure 8: Schematic illustration of the fiber preform architecture with two layers of nested plain weave preform shown from an (a) isometric and (b) side view, along with the fiber bundle width, *a*, thickness, *b*, and unit cell length, *l*.

multiple layers of plain weave fabric, with fiber bundle thickness $a$ and height $b$, stacked in a nested configuration as illustrated in the isometric and side views in Figure 8a and Figure 8b, respectively. The weave of the fiber bundles is considered to be a sinusoidal function and the cross section of each bundle is defined as being lenticular in shape. In actuality, each fiber bundle consists of several thousand individual fiber filaments, which is modeled by describing the fiber bundle as a porous medium with a permeability defined as a function of the fiber bundle volume fraction and the individual filament radius, considering a hexagonal packing arrangement of the fiber filaments within the bundle.

In addition to modeling the flow through the three-dimensional unit cell in Figure 8, in an effort to reduce the computational effort, the study also considered thin slices of the unit cell in the direction of fluid flow, as illustrated in Figure 9, and simulated the resin permeation through five such two-dimensional planes, at $\bar{x} = \frac{x}{l} =:$ (1) 1/2 (Figure 9a; middle of the unit cell), (2) 3/8
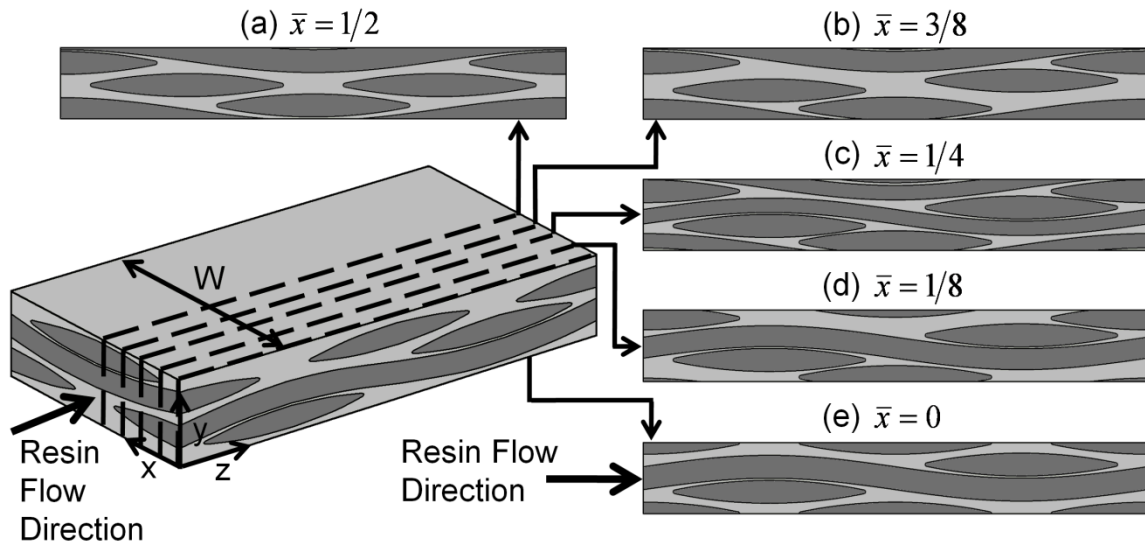


Figure 9: Schematic of the two-dimensional slices of the fiber preform architecture at $\bar{x}$ $(= x/l) =:$ (a) 1/2, (b) 3/8 (c) 1/4, (d) 1/8, and (e) 0. The dark gray area indicates the presence of a fiber bundle and the initial air surrounding the woven fiber bundles is represented by the light gray shading.

(Figure 9b), (3) 1/4 (Figure 9c), (4) 1/8 (Figure 9d), and (5) 0 (Figure 9e; edge of the unit cell).

The void fraction in the three-dimensional geometry was then estimated through a volumetric summation of the void content in individual slices. It can be observed from the geometry shown in Figure 8 that the three-dimensional fiber architecture is anti-symmetric about the middle plane defined in Figure 9a, which implies that the slices in Figure 9b–Figure 9e are inverted at their respective locations when mirrored on the opposite side of the middle plane (at $\bar{x} = 1/2$). However, in a two-dimensional modeling the flow is identical through these inverted configurations and as a result the simulations on one half of the unit cell are representative of the flow through the entire domain.

For both the three-dimensional unit cell geometry and the two-dimensional slices, the governing mathematical equations describing the resin flow through the macro-scale inter-bundle regions and the porous fiber bundles are the conservation of mass and momentum along with the equation associated with the volume of fluid (VOF) method [92] used to track and advance the resin/air interface during the filling process. The governing mathematical equations are expressed in a nondimensional form using the following dimensionless parameters:

$$\bar{\boldsymbol{u}} = \frac{\boldsymbol{u}}{u_{in}} \qquad \bar{x} = \frac{x}{l} \qquad \bar{y} = \frac{y}{l} \qquad \bar{z} = \frac{z}{l} \qquad \bar{t} = \frac{t}{l/u_{in}} \qquad \bar{p} = \frac{p}{\rho_r u_{in}^2}$$

where $\bar{\boldsymbol{u}}$ is the dimensionless velocity vector describing the fluid motion and $u_{in}$ is the inlet resin velocity, $\bar{x}$, $\bar{y}$, and $\bar{z}$ are the three dimensionless Cartesian directions, $\bar{t}$ is dimensionless time, $\bar{p}$ is dimensionless pressure, and $\rho_r$ is the density of the resin phase. In addition, the Reynolds number, $Re$, and Capillary number, $Ca$, are defined as:

$$Re = \frac{\rho_r u_{in} l}{\mu_r} \qquad Ca = \frac{\mu_r u_{in}}{\sigma}$$

33

where the resin viscosity is $\mu_r$ and $\sigma$ is the surface tension. In the VOF method, the volume fraction of the resin in a computational cell, $\alpha$, is governed in dimensionless form by:

$$\frac{\partial \alpha}{\partial \bar{t}} + \bar{\nabla} \cdot (\alpha \bar{\boldsymbol{u}}) = 0 \tag{18}$$

where $\bar{\nabla}$ is the dimensionless gradient operator. Assuming incompressible fluid properties, conservation of mass is described by the dimensionless continuity equation, written as:

$$\bar{\nabla} \cdot (\bar{\boldsymbol{u}}) = 0 \tag{19}$$

Conservation of momentum for flow around the fiber bundles in the macro-pores of the unit cell is enforced through the dimensionless Navier-Stokes equation. In the case of flow within the micro-pores of the fiber bundle, two source terms are added to this equation in order to account for the porous and capillary effects within the fiber bundle. For conciseness of presentation, Equation 20 and Equation 21 include the porous media and capillary source terms (the last two terms in Equation 20 and Equation 21), however these two source terms are only active within the porous domains of the unit cell. The presence of the two-phase flow in the model requires two momentum equation descriptions using the properties of the different fluid phases, written for resin and air, respectively, as:

$$\frac{\partial}{\partial \bar{t}}(\bar{\boldsymbol{u}}) + \bar{\nabla} \cdot (\bar{\boldsymbol{u}}\bar{\boldsymbol{u}}) = -\bar{\nabla}\bar{p} + \frac{1}{Re}\bar{\nabla} \cdot (\bar{\nabla}\bar{\boldsymbol{u}} + \bar{\nabla}\bar{\boldsymbol{u}}^T) + \frac{1}{Re}\bar{F}_{por} + \frac{1}{Re * Ca}\bar{F}_{cap} \tag{20}$$

$$\frac{\partial}{\partial \bar{t}}(\bar{\boldsymbol{u}}) + \bar{\nabla} \cdot (\bar{\boldsymbol{u}}\bar{\boldsymbol{u}}) = -\frac{\rho_r}{\rho_a}\bar{\nabla}\bar{p} + \frac{\rho_r}{\rho_a}\frac{\mu_a}{\mu_r}\left[\frac{1}{Re}\bar{\nabla} \cdot (\bar{\nabla}\bar{\boldsymbol{u}} + \bar{\nabla}\bar{\boldsymbol{u}}^T) + \frac{1}{Re}\bar{F}_{por}\right] + \frac{\rho_r}{\rho_a}\frac{1}{Re * Ca}\bar{F}_{cap} \tag{21}$$

where the density and viscosity of the air phase are denoted by $\rho_a$ and $\mu_a$, respectively, $\bar{F}_{por}$ is the dimensionless porous media source term, and the dimensionless capillary source term is denoted by $\bar{F}_{cap}$. The dimensionless source term corresponding to the flow through the porous fiber bundles was expressed using Darcy's Law as

$$\bar{F}_{por} = -\frac{l^2}{[\kappa]}\bar{\boldsymbol{u}} \tag{22}$$
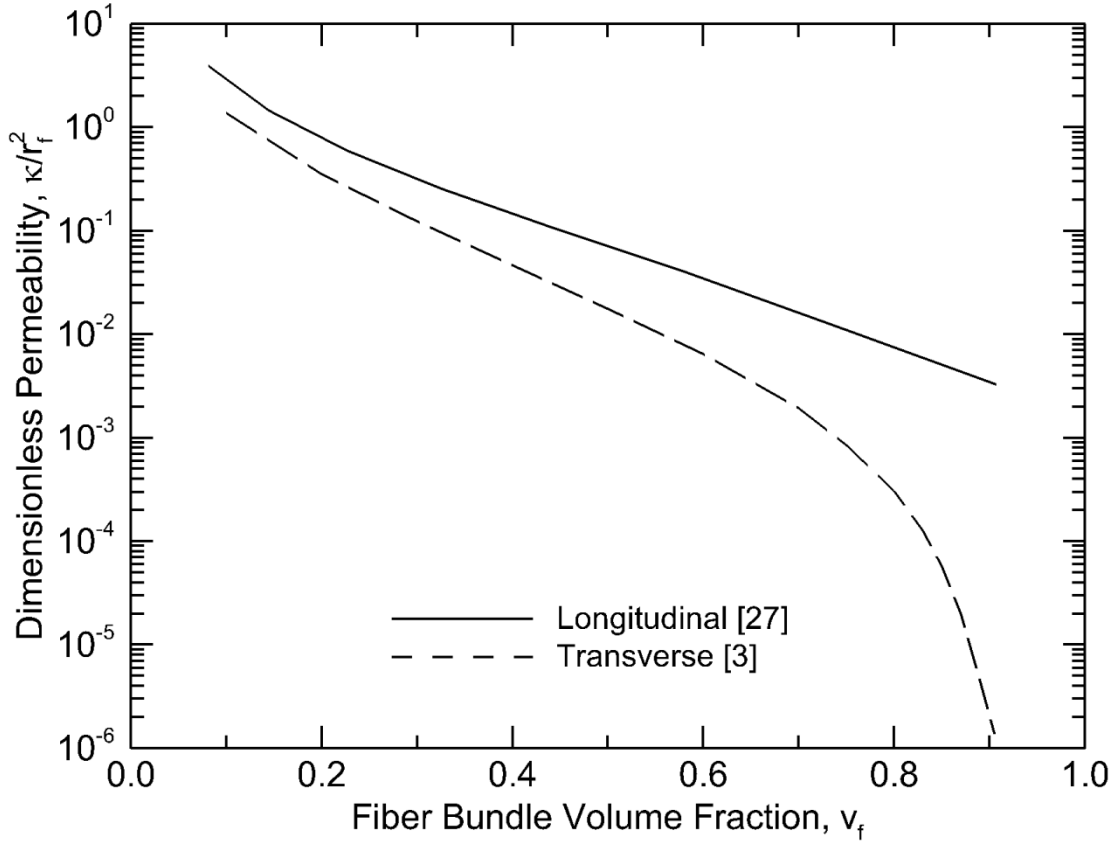
Figure 10: Variation of the dimensionless transverse permeability [3] and the longitudinal permeability developed in Chapter 2 and [27] with the fiber bundle volume fraction for fiber tows with a hexagonal-packed fiber arrangement.

where $[\kappa]$ is the permeability tensor of the porous media. The permeability values were calculated using the relationships with the fiber bundle volume fraction shown graphically in Figure 10, which presents the permeability nondimensionalized by the square of the individual fiber filament radius, $r_f$. The longitudinal permeability values in Figure 10 are based on an analytical permeability model presented in Chapter 2 and [27] and the transverse permeability values were adapted from [3]. A permeability tensor is defined along the curvature of the fiber bundle based on projecting the longitudinal and transverse permeability values of the idealized aligned rigid fiber bundles onto the local axis of the woven fiber bundle throughout the unit cell.

By definition, the capillary forces are present only at the resin-air interface within the fiber bundle flow field of the geometry. However, a continuum method for modeling surface tension effects across the interface of two adjacent fluids was developed in [93]. By using the divergence theorem, the capillary effects at the resin-air interface can be converted to a body force and expressed as a source term in the momentum equation [94], written as

$$\bar{F}_{cap} = 2\bar{p}_c \alpha \bar{\nabla} \alpha \tag{23}$$

where $\bar{p}_c$ is the dimensionless capillary pressure in the fiber bundle at the resin-air interface and $\alpha$ is the local volume fraction of the resin. In the VOF model, the volume fraction variable is defined as 0 for purely resin and 1 for purely air. At the interface of these two phases is a thin region where the volume fraction varies smoothly between 0 and 1, and a value of 0.5 is chosen to represent the approximate transition between phases. It is evident that the gradient of the volume fraction term in Equation 23 will be non-zero only along this thin region where $\alpha$ varies between 0 and 1, satisfying the physical presence of the capillary forces occurring at the resin-air interface. Within the idealized fiber bundle of straight aligned rigid fibers, the capillary force occurs in two principal directions: causing the resin to wick (1) radially inward perpendicular to the fibers and (2) longitudinally through the fibers in the bundle. In the first case, the dimensionless capillary pressure forces the resin radially into the fiber bundle (perpendicular to the individual fibers) and can be expressed in dimensionless form according to [35] as

$$\bar{p}_{c,r} = \frac{l}{\pi r_f} \int_{-\pi/2}^{\pi/2} \frac{cos(\theta + \eta)}{\left(\sqrt{\pi/(2\sqrt{3}v_f)} - cos(\eta)\right)} d\eta \tag{24}$$

where $\bar{p}_{c,r}$ is the dimensionless capillary pressure acting radially along the fibers, $\theta$ is the wetting angle of the resin, $v_f$ is the fiber volume fraction of the fiber bundle, and $\eta$ is the angular location of the resin-air meniscus during flow between neighboring fibers. The integral in Equation 24 is

36

necessary to average the pressure as the capillary width changes according to perpendicular flow between two adjacent cylindrical fibers. In the case of capillary flow longitudinal to the aligned rigid fibers, the capillary width is constant as the resin is wicked along the channels and consequently the dimensionless capillary pressure is constant as well and written in dimensionless form according to [28] as

$$\bar{p}_{c,l} = \frac{2lv_f \cos(\theta)}{r_f(1 - v_f)} \tag{25}$$

where $\bar{p}_{c,l}$ is the capillary pressure acting longitudinal to the fibers. Following the foregoing approach, the capillary pressure values can be calculated at the resin-air interface in the two principal resin infiltration directions.

Equation 18–Equation 25 provide a complete description of the resin flow through the preform and were numerically solved to investigate the resin evolution through the plain weave preform architecture illustrated in Figure 8 and Figure 9. A constant and uniform resin velocity was imposed as the boundary condition at the inlet plane of the unit cell geometry and a constant pressure boundary was enforced at the outlet plane. The top and bottom faces of the unit cell were defined as periodic boundaries based on the geometry of the two-dimensional fiber arrangements as seen in Figure 9a–Figure 9e. It must be mentioned that the domain considered for the modeling consists of a full repeating unit cell and a half unit cell length upstream and a half unit cell downstream. This extended unit cell geometry allows the initially uniform resin flow front to migrate naturally through and around the fiber bundles in the first half unit cell before entering the complete unit cell of study (which is the focus of the results presented below), thereby better approximating the actual resin flow development through the preform geometry.

The domain geometry and the model formulation were implemented in and solved using the commercial ANSYS Fluent™ software using numerous supplementary user-defined functions

37

(UDF's) developed to model the permeability and surface tension forces included in the momentum equation. The two-dimensional models used a mesh of approximately $0.8 \times 10^4$ elements and $4.5 \times 10^4$ elements were used in the three-dimensional simulations. The PISO scheme was used for the pressure-velocity coupling [95], a first-order implicit scheme was applied for the time discretization, a second-order upwind scheme was implemented for the momentum discretization, and the CICSAM scheme was used to solve the volume fraction equation [96]. Iterations at each time step were allowed to run until the residuals for each governing equation dropped below $10^{-4}$, and various grid densities and time-steps were explored to verify grid and time-step independence. All computations were performed on a single Dell PowerEdge R610 server with a 2.53 *GHz* processor and 12 GB of RAM, and the computing times for a fully three-dimensional solution through a complete unit cell (Figure 8) ranged from 5–8 days depending on the *Ca* and *Re* values, whereas the computing times were correspondingly in the range of 8–20 hrs. for the simulations through the five two-dimensional slices (Figure 9a–Figure 9e) of the three-dimensional volume. The simulations yielded the flow front progression through the inter- and intra-fiber-bundle regions of the unit cell as a function of time. Using the flow progression information, the void locations in the unit cell as well as the total void content was calculated as a function of time to determine the steady state void fraction, where the results of the study are presented and discussed below.

### 3.2  Void Diagrams

Two commercially available plain weave fabric geometries were chosen for the study, specifically a Rovcloth 2454 (Fiber Glass Industries Inc., Amsterdam, NY) and an Owens Corning WR10/3010 (OCV Fabrics US Inc., Toledo, OH) fabric with their associated fiber bundle

dimensions, and inter-bundle spacing. For the Rovcloth 2454 fabric, the preform dimensions of $a$, $b$, and $l$ were determined to be 4.1, 0.43, and 5.5 $mm$, respectively, and the second plain weave fabric, Owens Corning WR10/3010 (OC WR10/3010), had a similar weave geometry with $a$, $b$, and $l$ equaling 3.5, 0.78, and 4.5 $mm$, respectively. In both fabrics the fiber bundles were assumed to have a fiber volume fraction of 0.6 and the individual fiber filaments within the fiber bundle were considered to be 10 $\mu m$ in diameter. The dynamic viscosity of the resin was chosen to be 0.01 $Pa \cdot s$ and the resin-air interface was described with a contact angle of 30 $degrees$.

A parametric study was conducted to investigate the effects of varying the Reynolds, $Re$, and Capillary, $Ca$, numbers on the resulting void content evolution in each of the five planar slices identified in Figure 9. Four different $Re$ values of 0.23, 5.75, 40.3, and 479 as well as four $Ca$ numbers of $1.6 \times 10^{-4}$, $4.0 \times 10^{-3}$, $2.8 \times 10^{-2}$, $3.3 \times 10^{-1}$ were studied in each of the five planes, for a total of 80 parametric runs. These values of $Ca$ and $Re$ were chosen for the parametric sweep in order to compare the current numerical simulations with similar experimental results presented in [97]. In each case, the flow progression and corresponding void content were recorded over time, as discussed in this Section. Further, the results of the flow along the planar unit cell slices (Figure 9) are also compared with results from simulations of the full three-dimensional flow through the unit cell geometry shown in Figure 8 to establish the accuracy of the computationally simpler modeling using the multiple two-dimensional slices.

Figure 11–Figure 13 present snapshots of the resin infiltrating each plane of the fiber preform architecture at progressive times throughout the mold filling process at various combinations of Capillary and Reynolds numbers using the two-dimensional planar geometries. The resin is injected uniformly at the left plane of the unit cell (as shown in Figure 9e) and allowed to permeate through the entire geometry. The local void content, $\phi$, at each time step is presented below every
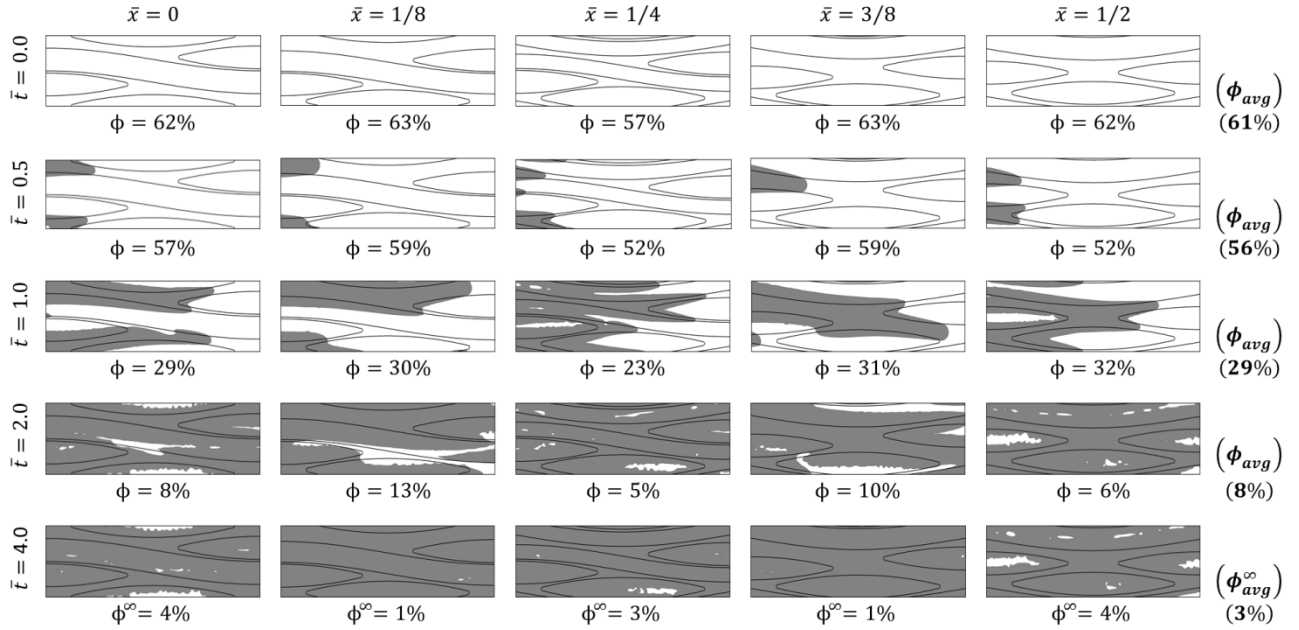
Figure 11: Snapshots of the resin infiltration, shown by the gray shading, through the various two-dimensional cross-sections of the Rovcloth 2454 fiber preform for $Ca = 2.8 \times 10^{-2}$ and $Re = 5.75$ at $\bar{t} = 0, 0.5, 1, 2,$ and $4$. The void content in each slice, $\phi$, the volume-averaged void content, $\phi_{avg}$, and the final void content, $\phi^{\infty}$, are indicated at each time step for each cross-section.

snap-shot of the respective cross-sectional plane and the average void content, $\phi_{avg}$ (calculated at each time step by volume-averaging the local void content in each plane), is shown in bold text in the far right-hand column of Figure 11–Figure 13 to approximate the void content in the entire fiber preform geometry over time. The local steady-state, or final, void content in each simulation is denoted by $\phi^{\infty}$ and the final average void content is given by $\phi_{avg}^{\infty}$. The gray shaded areas in Figure 11–Figure 13 represent the resin region, while the unshaded areas denote air. Although at $\bar{t} = 0$ in Figure 11–Figure 13 the entire geometry is unshaded, indicating that there is no resin yet infiltrating the unit cell, the average void content is less than 100% because of the presence of the fiber bundles within the preform. The fiber bundles are modeled as porous media and occupy a

fixed volume of approximately 39% of the unit cell and, therefore, the initial average void content

at $\bar{t} = 0$ is 61%.

The resin flow development through the fiber geometry for $Ca = 2.8 \times 10^{-2}$ and $Re = 5.75$

is presented in Figure 11. Initially, at $\bar{t} = 0$, the resin has not yet infiltrated the unit cell and each

of the five planes is saturated with air, where the edges of the fiber bundles in each of the

respective slices are clearly visible and $\phi_{avg} = 61\%$. At $\bar{t} = 0.5$, the resin has begun to flow into

the unit cell and primarily follows the path of least resistance through the macro-scale channels in

between the fiber bundles, although some fiber bundle permeation is also evident. As time

advances to $\bar{t} = 1$, the resin has permeated further into the macro-scale channels and has also

begun to fill into the fiber bundles of each plane, entrapping significant pockets of air in the

$\bar{x} = 1/4$ and $\bar{x} = 1/2$ planes within the fiber bundles. The resin flow front reaches the outlet in

the macro-scale channels in each of the different plane sections at $\bar{t} = 2$, and the average void

content is found to be approximately eight percent of the total unit cell volume. At $\bar{t} = 4$ the void

content decreases to approximately three percent and becomes nearly steady over time in each of

the planes, depicting the final size and location of the entrapped air pockets within each of the fiber

bundles. Significant void formation is visible in the $\bar{x} = 0$, $\bar{x} = 1/4$, and $\bar{x} = 1/2$ planes at this

steady state condition and, conversely, almost complete resin saturation is apparent in the $\bar{x} = 1/8$

and $\bar{x} = 3/8$ planes. Note that the periodic nature of the resin flow enforced at the top and bottom

faces of each of the unit cells is apparent throughout the simulation results presented in Figure 11.

Several observations can be made regarding the void formation in each of the fiber bundles in

the simulation shown in Figure 11: It is evident that at $\bar{t} = 4$, the void in the first cross-running

bundle (seen as one half bundle section at the left edge of the frame in Figure 11 for $\bar{x} = 1/2$) is

larger than the void in the third cross-running bundle (the one half bundle section at the right edge
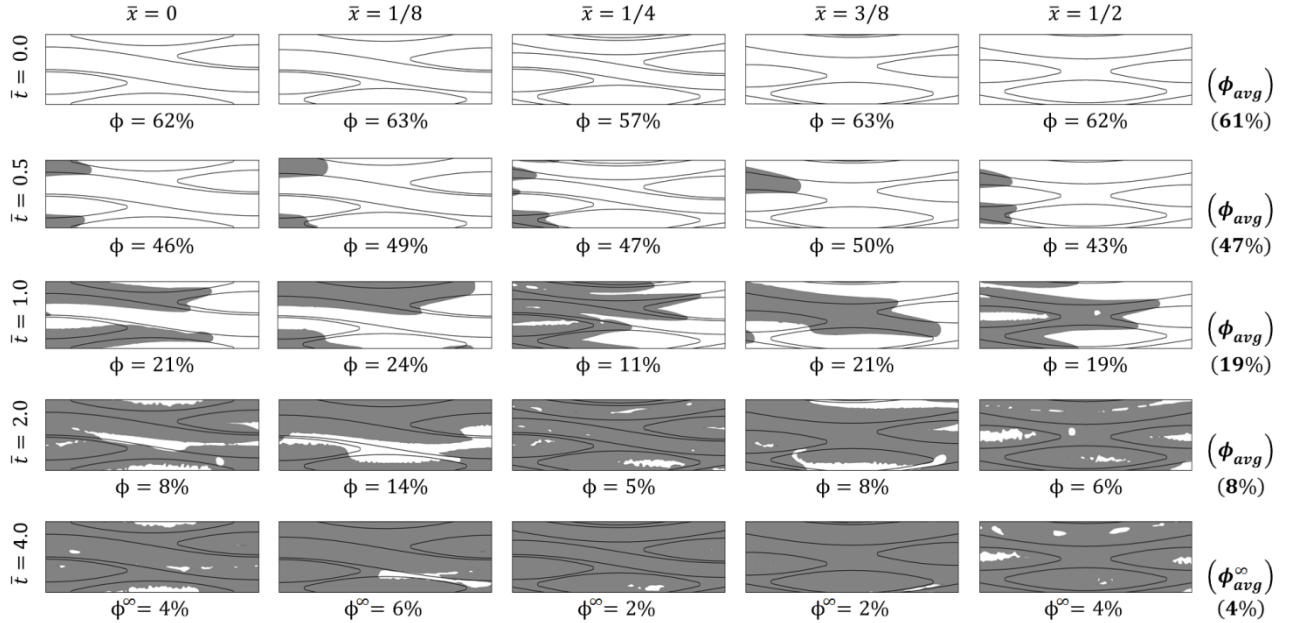
Figure 12: Snapshots of the resin infiltration, shown by the gray shading, through the various two-dimensional cross-sections of the Rovcloth 2454 fiber preform for $Ca = 2.8 \times 10^{-2}$ and $Re = 0.23$ at $\bar{t} = 0, 0.5, 1, 2,$ and 4. The void content in each slice, $\phi$, the volume-averaged void content, $\phi_{avg}$, and the final void content, $\phi^{\infty}$, are indicated at each time step for each cross-section.

of the frame in Figure 11 for $\bar{x} = 1/2$). This suggests that as the resin moves from left to right through adjacent unit cells directly downstream from one another, the amount of air entrapped in the cross-running fiber bundles will decrease slightly. It can also be seen in each plane at $\bar{t} = 4$ that the voids remaining in the cross-running fiber bundles are larger than the voids remaining in the longitudinal-running fiber bundles, where the resin has permeated further into the longitudinal-running fiber bundles and resulted in less entrapped air remaining in these regions. In each of the frames in Figure 11, the steady state voids are located within the fiber bundle regions, exemplifying flow conditions which lead to micro-void formation within the fiber bundles during processing.

For the additional parametric combinations of Reynolds and Capillary numbers, the trends observed in the numerical simulations are similar to those presented in Figure 11 with the principal

differences occurring in the resin flow front position over time and the final location and volume of the entrapped voids. An illustration of a flow condition leading to dissimilar final void locations and sizes than those in Figure 11 is shown in Figure 12, which presents the resin flow development through the fiber geometry for $Ca = 2.8 \times 10^{-2}$ and $Re = 0.23$ at successive times throughout the mold filling process, where the snapshots in Figure 12 correspond to equivalent time instants as shown in Figure 11. Although Figure 11 and Figure 12 are seen to present similar resin flow evolutions, a fundamental difference is observed in the final air entrapment locations. At $\bar{t} = 4$ in Figure 12, macro-voids are formed in the flow region between fiber bundles in the $\bar{x} = 1/8$ and $\bar{x} = 3/8$ planes (seen on the right side of the respective planes between the lowest cross- and longitudinal-running bundles in Figure 12) as the flow reaches steady state conditions, as opposed to the voids in Figure 11 occurring exclusively within the fiber bundles at steady state. Also
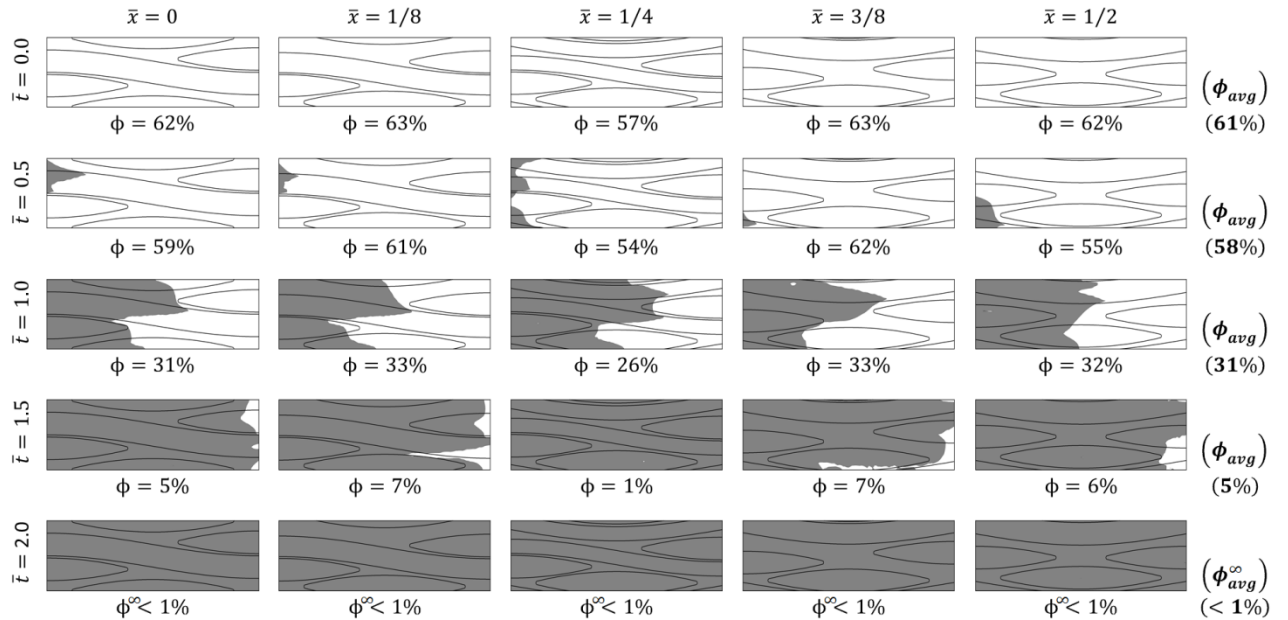


Figure 13: Snapshots of the resin infiltration, shown by the gray shading, through the various two-dimensional cross-sections of the Rovcloth 2454 fiber preform for $Ca = 4.0 \times 10^{-3}$ and $Re = 5.75$ at $\bar{t} = 0$, 0.5, 1, 1.5 and 2. The void content in each slice, $\phi$, the volume-averaged void content, $\phi_{avg}$, and the final void content, $\phi^{\infty}$, are indicated at each time step for each cross-section.

noteworthy is the fact that the resin has completely permeated the fiber bundles in the $\bar{x} = 3/8$ plane in Figure 12 at $\bar{t} = 4$ but has not totally permeated the fiber bundles in the $\bar{x} = 1/8$ plane, where some air entrapment is evident in the longitudinally-running fiber bundle adjacent to the macro-void formation. The final steady state void content of approximately 4% in Figure 12 is visually and quantitatively larger than that in Figure 11, indicating that the decrease in the Reynolds number resulted in a slightly higher overall final average void content in the fiber preform. The results in Figure 12 demonstrate processing conditions that lead to a combination of micro- and macro-void formation during the mold-filling stage of LCM.

An example of processing conditions that minimize the final average void content in the fiber preform is shown in Figure 13 for $Ca = 4.0 \times 10^{-3}$ and $Re = 5.75$ at successive times throughout the mold filling process. It is apparent that the resin flow is almost identical in each of the planes in Figure 13 at all times during the filling process. Further, the flows through the longitudinal fiber bundles, the cross-running fiber bundles, and the macroscale inter-bundle regions are nearly balanced throughout the process. This balanced resin flow evolution results in an even fill of the preform where minimal air voids are entrapped during processing, in contrast to the cases shown in Figure 11 and Figure 12 where the resin raced through the macro-scale channels and greatly outpaced the flow in the fiber bundle regions and resulted in higher final average void contents. Note that the resin flow front in each of the different simulations shown in Figure 11–Figure 13 reached the outlet at approximately the same dimensionless time of $\bar{t} = 2$; however, for the balanced flow presented in Figure 13, a steady state condition is at this same time of $\bar{t} = 2$, whereas the flows in Figure 11 and Figure 12 took about twice as long ($\bar{t} = 4$) to reach steady state conditions. A final average void content of less than 1% in the simulation shown in Figure 13 further demonstrates that the parametric combination of $Ca = 4.0 \times 10^{-3}$ and $Re =$

5.75 represents processing conditions that minimize void content during LCM processing using a Rovcloth 2454 woven fabric.

### 3.3 Dynamic Void Development

To quantitatively investigate the air entrapment within the unit cell during preform permeation, the local void content, $\phi$, in each of the planes shown in Figure 9 was tracked over time for different flow conditions described by various Capillary and Reynolds number combinations. Figure 14 shows a comparison between the void content evolution in each of these different planes for four different combinations of $Re$ and $Ca$ values as indicated in the plots. It is evident that when $Ca = 4.0 \times 10^{-3}$ (Figure 14a and Figure 14c) the void content within the unit cell initially
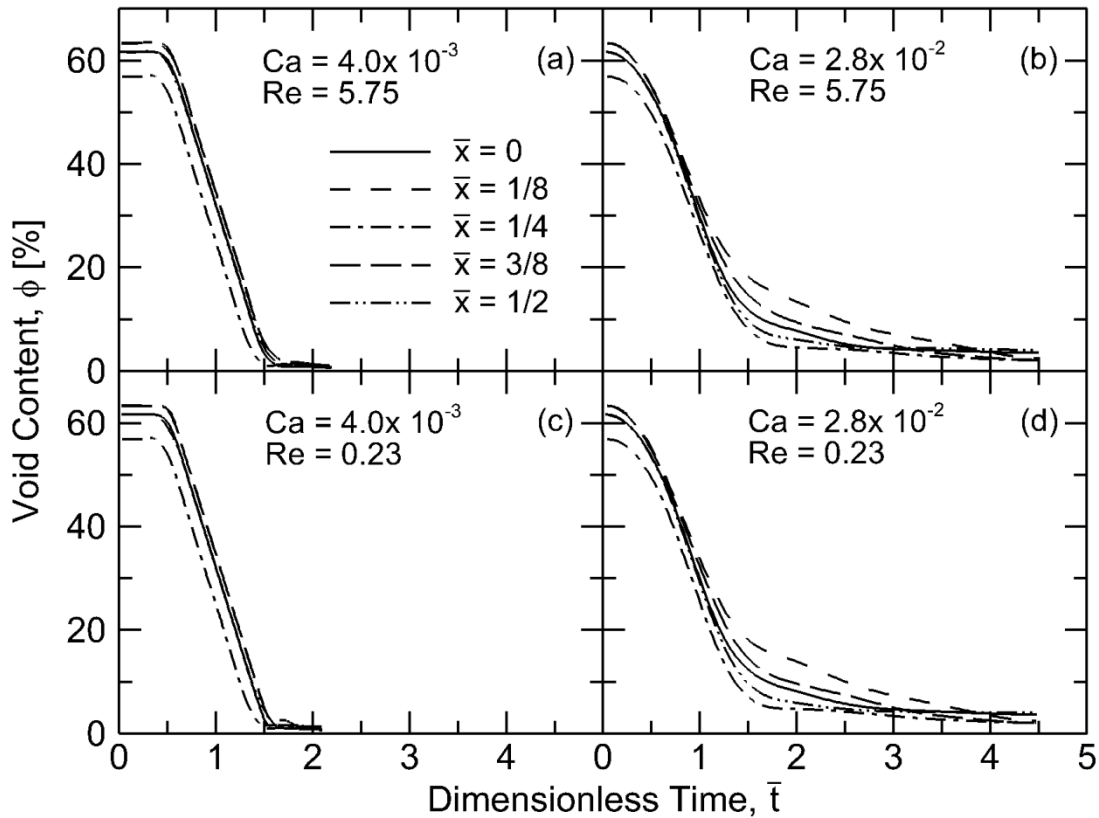


Figure 14: Void content, $\phi$, in each of the two-dimensional planes of the Rovcloth 2454 fabric for the parameter combinations of (a) $Ca = 4.0 \times 10^{-3}$ and $Re = 5.75$, (b) $Ca = 2.8 \times 10^{-2}$ and $Re = 5.75$, (c) $Ca = 4.0 \times 10^{-3}$ and $Re = 0.23$, and (d) $Ca = 2.8 \times 10^{-2}$ and $Re = 0.23$.

45

remains constant as the resin permeates the first half of the unit cell geometry and then decreases steadily and rapidly as the resin enters into the unit cell of study in each plane at $\bar{t} = 0.5$. After the swift decrease in void content the entrapped air within the unit cell rapidly levels out and asymptotically approaches a steady state value. Since the resin flow front moves through the entire preform geometry at a relatively constant rate in the simulations shown in Figure 14a and Figure 14c, the transition regions where the resin enters and exits the unit cell are clearly identified to occur at $\bar{t} = 0.5$ and 1.5, respectively. As $Ca$ is increased to $2.8 \times 10^{-2}$ (Figure 14b and Figure 14d) the void content begins to decrease almost immediately as a result of the flow rushing through the macro-channels much quicker than the flow into the fiber bundles. The rate of the decrease in void content in the cases in Figure 14b and Figure 14d is approximately equal to those in Figure 14a and Figure 14c; however, there is a much more gradual transition region beginning at approximately $\bar{t} = 1$ in Figure 14b and Figure 14d as the void content slowly levels out and asymptotically approaches the steady state value. In this case, the resin first flows quickly through the macro-scale paths of the unit cell and subsequently begins to permeate into the fiber bundles, resulting in a gradual transition from predominantly macro-scale channel infiltration to micro-scale pore infiltration as the flow approaches a steady state condition. It is also evident that, in general, the air entrapment in the $\bar{x} = 1/4$ plane decreases more rapidly than in the other planes, as evident most noticeably for $Ca = 4.0 \times 10^{-3}$ (Figure 14a and Figure 14c). The faster evacuation of the air in the $\bar{x} = 1/4$ plane can be explained by considering that the local geometry in this case (Figure 9c) offers less overall macro-scale volume for the resin to flow through when compared to the other planes, therefore forcing the resin to permeate into the fiber bundles of the $\bar{x} = 1/4$ plane more rapidly and consequently reducing the void content faster. The variation in the results for the different flow situations in Figure 14a–Figure 14d suggests the existence of a spatial variation of

46
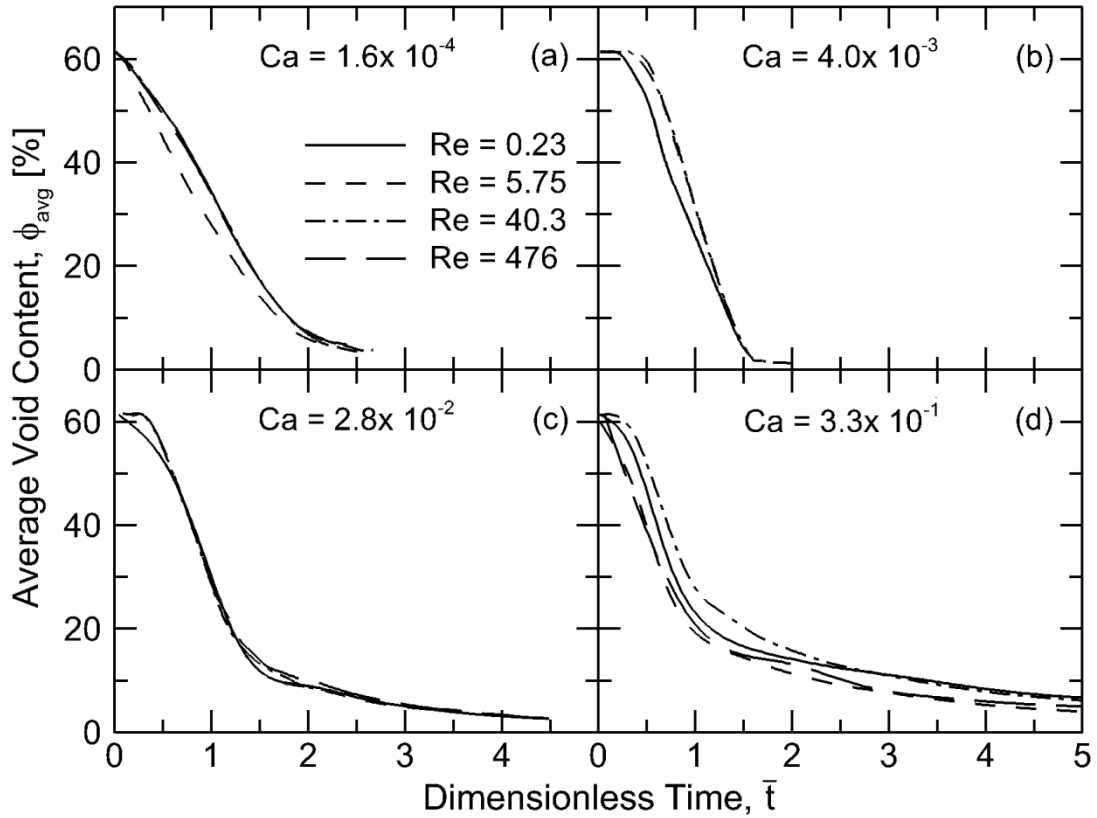
Figure 15: Volume-averaged void content, $\phi_{avg}$, in the Rovcloth 2454 fabric with $Ca$ = (a) $1.6 \times 10^{-4}$, (b) $4.0 \times 10^{-3}$, (c) $2.8 \times 10^{-2}$, and (d) $3.3 \times 10^{-1}$. Note that several of the plots are overlapping one another in (a)–(c).

the void content in the three-dimensional volume that is more pronounced at high Capillary numbers (Figure 14b and Figure 14d) than at lower Capillary numbers (Figure 14a and Figure 14c).

The results of the volume-averaged void content, $\phi_{avg}$, in the two-dimensional geometries over time for each of the 16 combinations of Reynolds and Capillary numbers studied are compared in Figure 15a–Figure 15d, where several of the trends for different $Re$ values are overlapping one another in Figure 15a–Figure 15c. It is evident that the void content evolution and the final void fraction are significantly different when $Ca$ is varied (comparing the overall trends *between* each subfigure) whereas they are relatively invariant with respect to a change in $Re$

(comparing the trends *within* each subfigure). Building upon observations in the discussion of Figure 11–Figure 13, the void content decreases rapidly in all the cases when $Ca = 4.0 \times 10^{-3}$ (Figure 15b) and reaches a steady state value of less than 1% quickly. The average void content in each of the cases in Figure 15a, Figure 15c, and Figure 15d is seen to vary more gradually with time. Note that for $Ca = 1.6 \times 10^{-4}$ (Figure 15a) the resin permeation is dominated by capillary flow within the fiber bundles, therefore resulting in macro-scale void formation within the unit cell. Conversely, resin flow through the macro-scale channels is dominant for $Ca = 2.8 \times 10^{-2}$ (Figure 15c) and $3.3 \times 10^{-1}$ (Figure 15d) which results in the resin rushing around the tows and entrapping air within the fiber bundles, thus forming micro-scale air voids. This trend is most
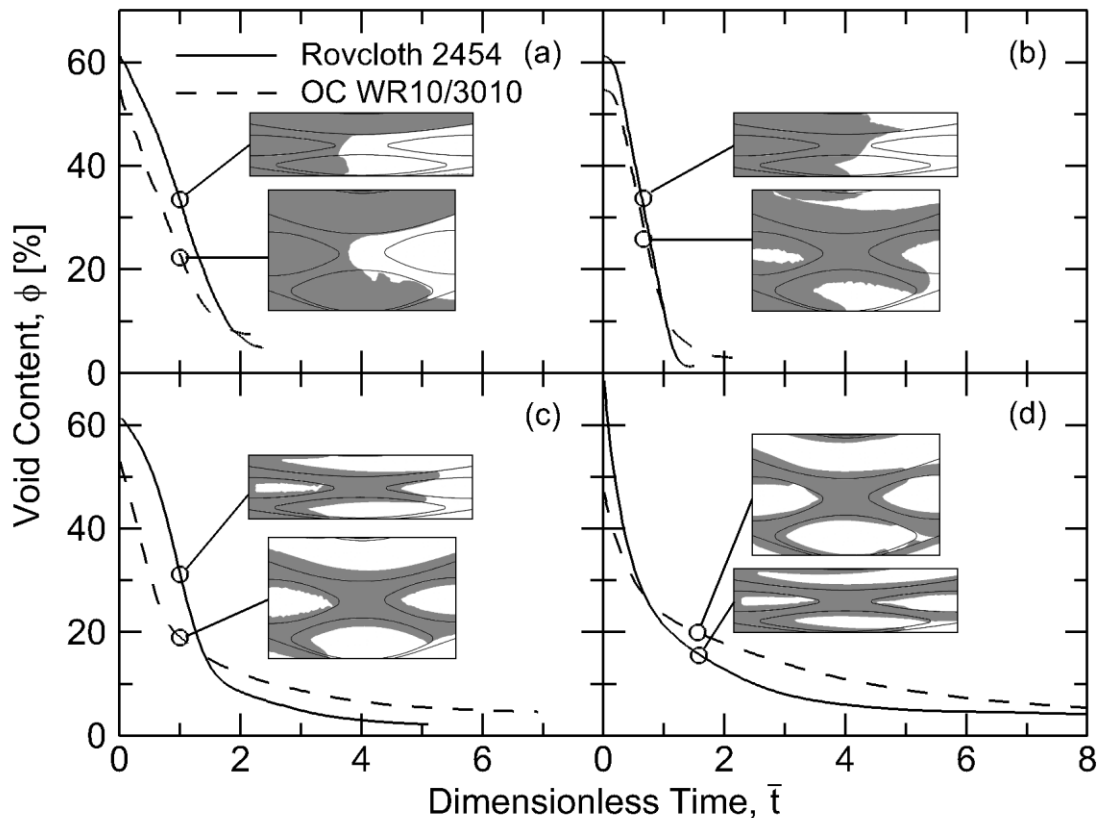


Figure 16: Comparison of the void content evolution with time for the Rovcloth 2454 and the Owens Corning WR10/3010 plain weave fabrics, in the $\bar{x} = 1/2$ two-dimensional plane for the parameter combinations of (a) $Ca = 1.6 \times 10^{-4}$ and $Re = 0.23$, (b) $Ca = 4.0 \times 10^{-3}$ and $Re = 5.75$, (c) $Ca = 2.8 \times 10^{-2}$ and $Re = 40.3$, and (d) $Ca = 3.3 \times 10^{-1}$ and $Re = 479$.

apparent in the curves shown in Figure 15c and Figure 15d where the void content initially decreases rapidly–corresponding to the quick infiltration of the macro-scale flow paths. The void content evolution then transitions and becomes more gradual over time as the resin infiltration begins to permeate into the micro-scale pores of the fiber bundles and the flow approaches a steady state. An examination of the trends in Figure 14 and Figure 15 reveal that the Capillary number has a relatively greater effect on the spatial void content distribution as well as the final void fraction and should therefore be carefully chosen in the design of the processing conditions, in agreement with the results presented in several studies (e.g. [41–43,97,98]).

The effect of the preform fabric geometry was studied by considering a second plain weave fabric, OC WR10/3010, with a similar weave geometry as the Rovcloth 2454 except for the bundle dimensions as mentioned in Chapter 3.1. In order to explore the influence of the fiber bundle geometry on the air entrapment evolution within the preform, Figure 16a–Figure 16d present a comparison of the void content that is developed in the $\bar{x} = 1/2$ plane for the two different fabrics, for four different combinations of the Reynolds and Capillary numbers as indicated in the figure caption. In each case, snapshots of the numerical simulation results are presented at selected times during the infiltration process, where the gray shaded areas represent the resin phase. The results shown in Figure 16 illustrate that the Owens Corning fabric initially begins with a slightly lower amount of air as a result of the different geometry. As time progresses, at the early stages of resin permeation, the Owens Corning fabric continues to contain less air than the Rovcloth fabric and the qualitative resin permeation and the rate of the void content evolution are similar for the two fabrics. However, in each case, the void content in the Rovcloth fabric eventually decreases to less than that of the Owens Corning fabric and the steady state void content in the Rovcloth fabric is consistently lower than that in the Owens Corning material, as seen in Figure 16a–Figure 16d. In

Figure 16a, at a low $Ca$ value of $1.6 \times 10^{-4}$—for which the surface tension is dominant—it is evident that the resin permeation in the longitudinal-running fiber bundle is leading the remainder of the flow front in the macro-pores. When $Ca$ is increased to $4.0 \times 10^{-3}$(Figure 16b), the final void content in the Rovcloth is approximately one percent and the resin flow front is approximately equal in each of the flow domains, as shown by the flow snapshot for this fabric in Figure 16b. Conversely, the resin flow front in the Owens Corning fabric shown in Figure 16b is not uniform and significant pockets of air are entrapped in the cross- and longitudinal-running fiber bundles. Figure 16c and Figure 16d present cases with progressively larger values of $Ca$ and $Re$, illustrating micro-void formation within the fiber bundles of both fabrics; the resin permeation in each case is qualitatively similar for the two fabrics, although the final void content is higher in the Owens Corning fabric for both cases. The trends in Figure 16 illustrate that the final void content is not only dependent on $Ca$ and $Re$ but also on the physical dimensions of the fiber bundle weave architecture, where an increase in the thickness of the fiber bundles (as in the Owens Corning fabric) generally results in an increase in the final void content of the preform as a result of the thicker bundles being more difficult to fully permeate with resin under similar flow conditions.

### 3.4  Experimental Comparison

The predicted volume-averaged values of the steady state void content within the unit cell as a function of the Capillary number are shown in Figure 17, where the final average void content values, $\phi_{avg}^{\infty}$, correspond to the asymptotic tails of the curves in Figure 15 and Figure 16 for the Rovcloth and Owens Corning fabrics, respectively. In Figure 17, the void content predictions using the current numerical simulations are compared with experimental results reported in [97] (shown
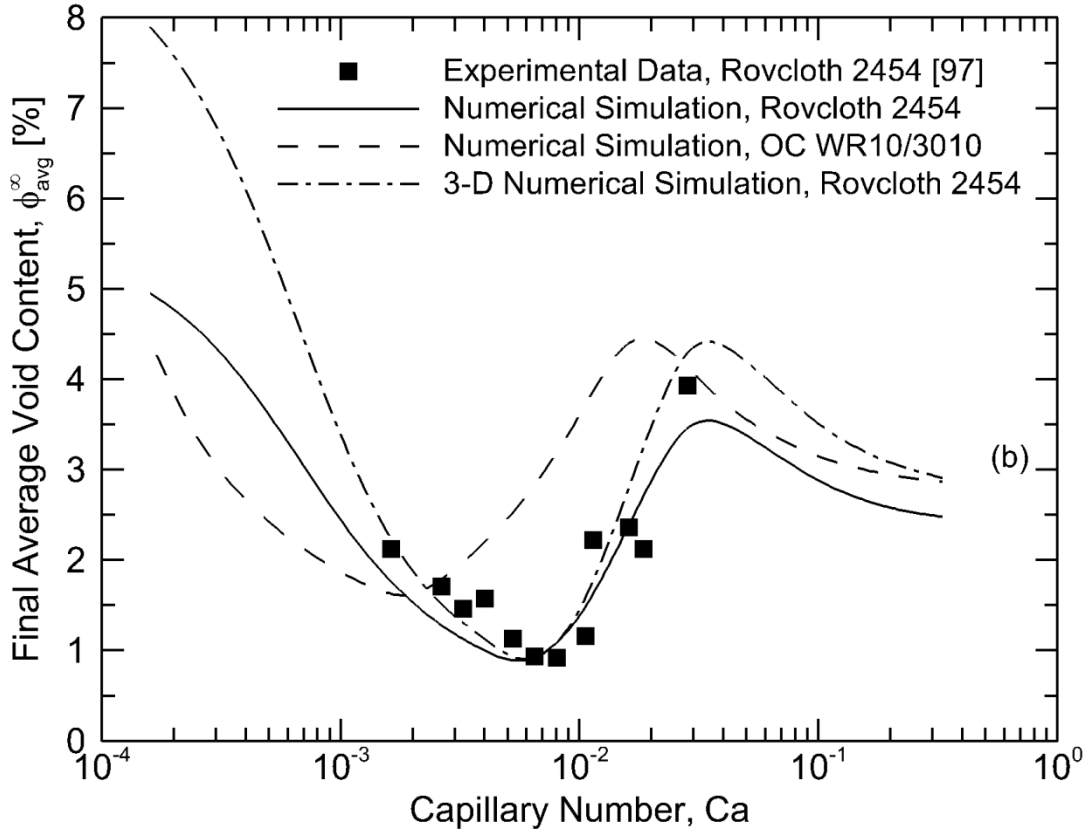
Figure 17: Comparison between experimentally measured [97] and numerically simulated final average void content values, $\phi_{avg}^{\infty}$, for the Rovcloth 2454 fabric, along with a comparison of the numerical simulation results predicting the void formation in the Owens Corning WR10/3010 fabric. Also presented are the results of a fully three-dimensional simulation of the flow in the complete unit cell geometry depicted in Figure 8 for a Rovcloth 2454 fabric.

as the filled square markers in Figure 17) which also used the Rovcloth 2454 woven fabric and identical resin material and flow conditions as in the current numerical study.

The numerical simulation results for the Rovcloth 2454 fabric are found to be in good agreement with the experimental void measurements from [97] over a wide range of Capillary numbers. The region $0.0015 \lesssim Ca \lesssim 0.0055$ in Figure 17 represents flow conditions where dry spots are formed in the macro-flow areas between the fiber bundles and the final average void content is seen to decrease with increasing $Ca$. In the region $0.0055 \lesssim Ca \lesssim 0.03$, the capillary forces become progressively less dominant, and the resin now rushes through the macro-flow paths

in the unit cell geometry to entrap air within the fiber bundles forming micro-voids, and the final average void content is seen to increase with *Ca* between 0.0055 and 0.03. The increase in macro-void formation when *Ca* is decreased below 0.0055 and an increase in micro-void formation when *Ca* is increased above 0.0055 up to 0.03 indicate that an ideal balance of the macro- and micro-scale flow within the unit cell geometry occurs when $Ca \approx 0.0055$ for the Rovcloth fabric.

Also presented in Figure 17 as the dash-dot line is the variation of the steady state void fraction with the Capillary number based on a fully three-dimensional solution of the flow through the complete three-dimensional unit cell (Figure 8) of the Rovcloth fabric, for comparison with the experimental results in [97] (the filled square markers in Figure 17) and the results based on the simulations using the five two-dimensional slices (the solid line in Figure 17). The three-dimensional simulation of the Rovcloth fabric shows excellent agreement with the experimental results in [97], predicting a similar void content trend as a function of the Capillary number. It is seen that the void content determined based on the five two-dimensional simulations shows good agreement with the results of the three-dimensional solution for $Ca \gtrsim 10^{-3}$; in the region $Ca \lesssim 10^{-3}$ the simulations through the two-dimensional planes are seen to underpredict the void content by up to 3% relative to the complete three-dimensional simulation, for $Ca \approx 10^{-4}$. This can be explained by considering that the capillary forces at the resin-air interface become increasingly dominant as *Ca* is decreased, and the wicking flow within the fiber bundles becomes much more significant. This wicking resin flow in the fiber bundles in the *x*-direction (Figure 8) of the three-dimensional unit cell are not accounted for in the two-dimensional slices taken along the *y*-*z* planes. Therefore, the resin is wicked in only two directions in the two-dimensional slices, with the predominant wicking occurring along the direction of resin infiltration (*z*-direction in Figure 8) toward the exit of the unit cell. As a result, the air is pushed out of the unit cell efficiently and

results in a lower final average void content. On the other hand, in the three-dimensional unit cell wicking in the *x*-direction is equally dominant as that in the *z*-direction towards the outlet. These additional flow paths caused by the resin wicking in the *x*-direction result in less air being pushed out three-dimensional unit cell, especially at low values of *Ca*, which leads to a higher overall void percentage in these cases. Computationally, however, the three-dimensional solution required over a week of CPU time for the smallest *Ca* of $1.6 \times 10^{-4}$, whereas the simulation through the five two-dimensional slices for this case took a maximum of only about 20 hrs. of CPU time, representing a tremendously faster approach to solving the problem without significant loss of accuracy.

As a comparison of the effects of the geometric parameters of the plain weave architecture, the final average void content in the Owens Corning fabric calculated from the numerical simulations is also presented in Figure 17 as the dashed line, where the trends are very similar to those of the Rovcloth fabric and the experimental data in [97]. The final average void content for the Owens Corning fabric are generally higher and the minimum and the maximum void fraction are found at smaller Capillary numbers at about 0.002 and 0.015, respectively, compared to the corresponding values of 0.0055 and 0.03 for the Rovcloth fabric. The results suggest that the flow paths offered to the infiltrating resin differs depending on the geometric parameters of the preforms, resulting in different values of *Ca* that describe a balance of the micro- and macro-scale flows in the preform. This result is significant in the determination of ideal processing conditions as well as a prediction of the overall final void content for different preform geometries.

Figure 17 shows that the final average void content decreases as the Capillary number is increased beyond ~0.03 for the Rovcloth fabric and beyond ~0.02 for the Owens Corning fabric. This is attributed to the increased pressure gradients within the preform for the higher Capillary
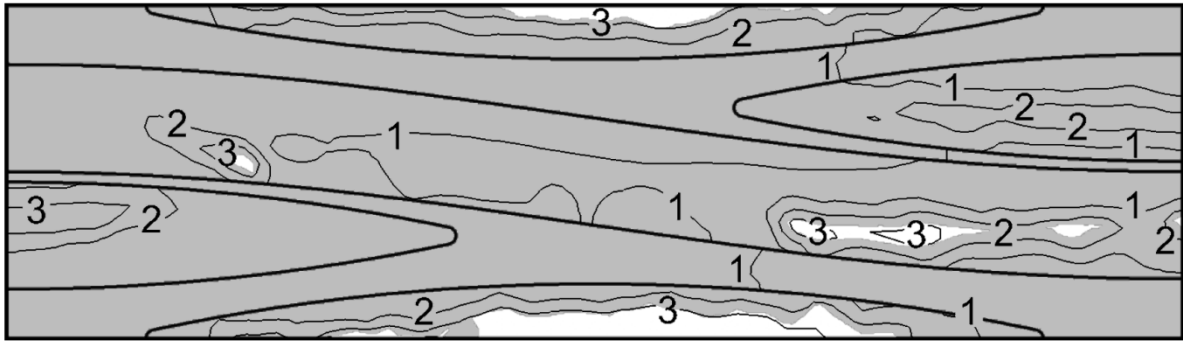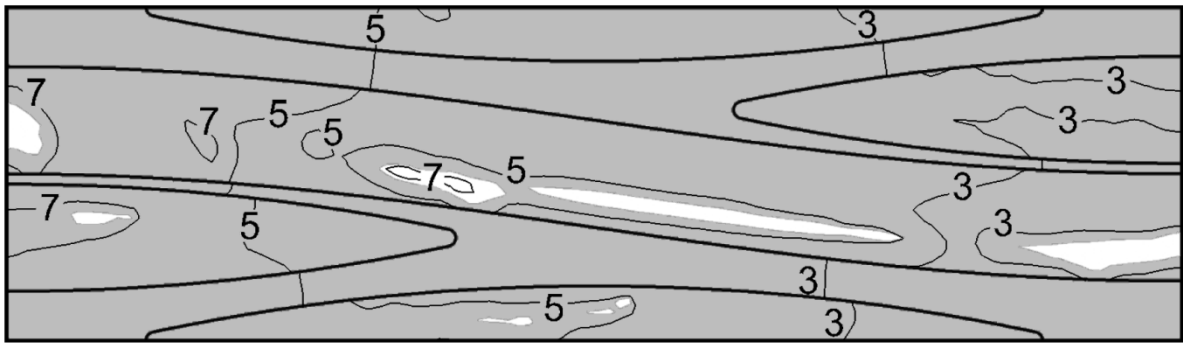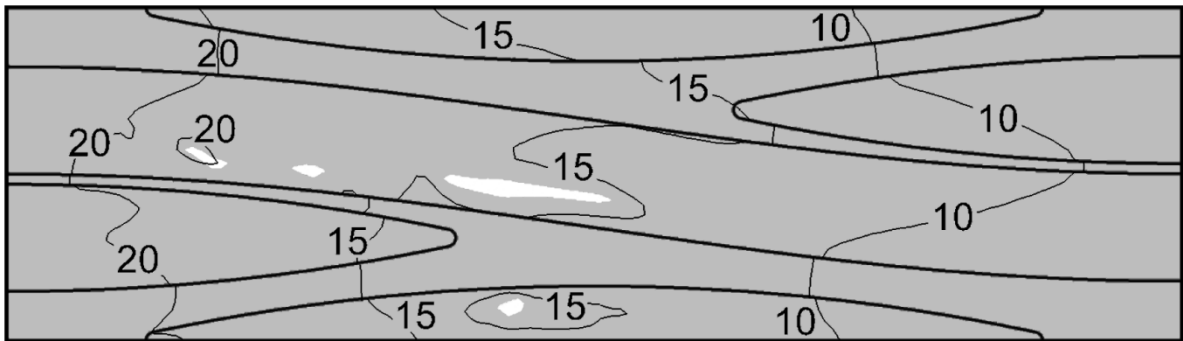
Figure 18: Pressure contours, $p$ [$MPa$] in the Rovcloth 2454 fabric at steady state in the $\bar{x} = 0$ plane for $Ca$ = (a) $2.8 \times 10^{-2}$, (b) $1.0 \times 10^{-1}$ and (c) $3.3 \times 10^{-1}$, where the gray shaded area represents the resin and the unshaded area represents the entrapped air locations.

numbers which cause the entrapped micro-scale air voids to shrink in size, thus reducing the overall void content within the fabric preform [97]. To illustrate this effect, Figure 18 presents the pressure contours within the $\bar{x} = 0$ plane of the Rovcloth fabric, at $t = 1$ for Capillary numbers

of $2.8 \times 10^{-2}$ (Figure 18a), $1.0 \times 10^{-1}$ (Figure 18b), and $3.3 \times 10^{-1}$ (Figure 18c). The shaded

areas in the frames denote the resin-filled region, while the entrapped air areas are shown in white.

For $Ca = 2.8 \times 10^{-2}$ (Figure 18a), the pressure varies from approximately 1–3 *MPa* and the areas

of highest pressure appear around the resin-air interface where the entrapped voids are present

within the fiber bundles. In this case, the resin has completely permeated the macro-scale paths and

has flowed a considerable distance into each of the individual fiber bundles within the unit cell,

entrapping a relatively small amount of air in the longitudinally running bundle and significantly

more air in the center cross-running bundle. As the Capillary number is increased to $1.0 \times 10^{-1}$

(Figure 18b) and $3.3 \times 10^{-1}$ (Figure 18c), the pressures within the unit cells increase accordingly

to 3–7 *MPa* and 10–20 *MPa*, respectively, and it is apparent that the overall void content within

the fiber bundles decreases as a result. Therefore, it is evident that the void content reduction with

increasing *Ca* can be associated with the concomitant increase in the pressure at the resin-air

interface around the void formations. Also notable in Figure 18 is the qualitative shift in the void

entrapment locations to be predominantly within the longitudinal fiber bundles as a result of the

Capillary number being increased: an increase in *Ca,* indicating a decrease in the relative capillary

forces, makes it more difficult for the resin to wick along the length of the longitudinal fiber tows

in comparison to the resin flow in the macro-scale channels and through the narrower cross-

running fiber bundles, resulting in the voids in the longitudinal fiber tows.

## 3.5 Processing Metrics

Based on the systematic parametric exploration of the process discussed so far, it is instructive

to determine the ranges of Capillary and Reynolds numbers that are desirable for actual processing.

To this end, four different parameters are considered that are each sought to be minimized: (1) the
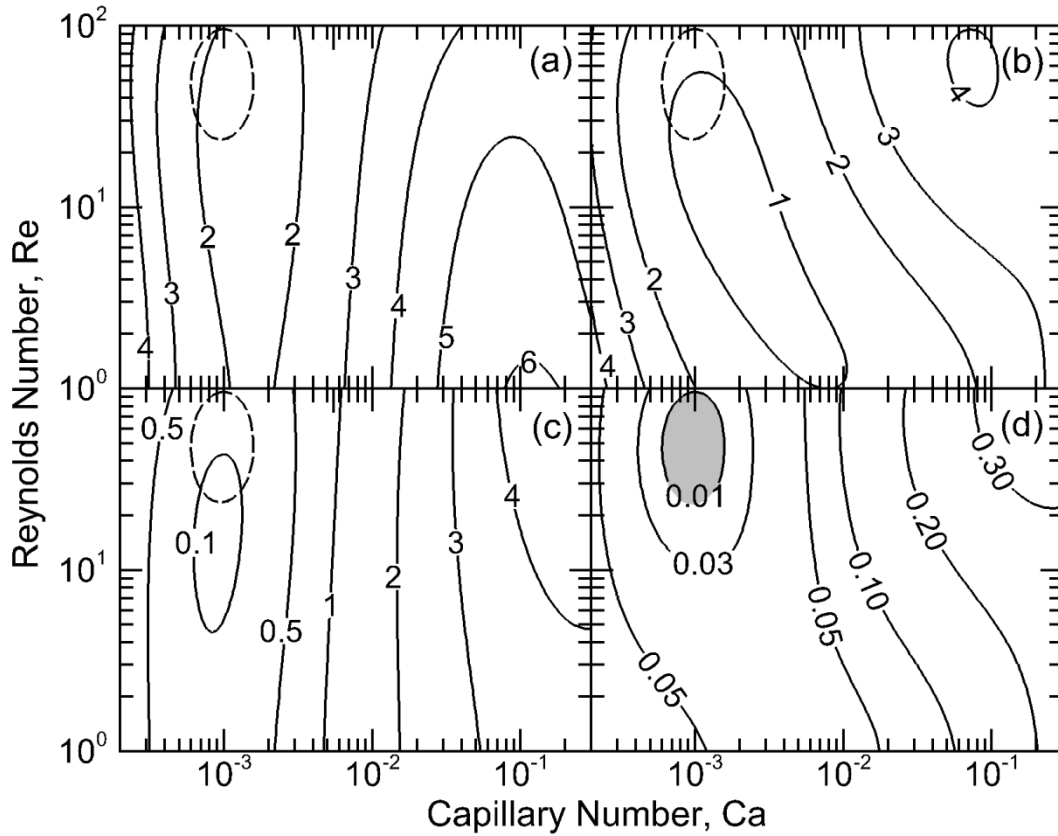
Figure 19: Contours of (a) maximum final void content, $\phi_{max}^{\infty}$, found in the two-dimensional slices of the Rovcloth 2454, (b) volume-averaged final void content, $\phi_{avg}^{\infty}$, considering each of the two-dimensional slices, (c) dimensionless excess flow time, $\bar{t}_{ex}$, and (d) combined parameter $\phi_{avg}^{\infty} \cdot \bar{t}_{ex}$ on a Capillary number–Reynolds number plane for the Rovcloth 2454. The most favorable processing window shown by the shaded light gray oval region in (d) is superimposed by the dashed oval in (a)–(c) to illustrate the corresponding maximum void content, average void content, and excess flow time, respectively, associated with the most favorable processing window

maximum void content from among the five preform planes, $\phi_{max}^{\infty}$, (2) the average void content over all the five preform planes, $\phi_{avg}^{\infty}$, (3) a dimensionless excess flow time needed to reach steady state, $\bar{t}_{ex}$ and (4) a combined objective defined as $\phi_{avg}^{\infty} \cdot \bar{t}_{ex}$, all calculated from the two-dimensional geometry results. Figure 19a–Figure 19d presents contour maps of the four parameters identified above on a Reynolds number—Capillary number space for the Rovcloth 2454 fabric.

The predicted maximum and average values of the steady state void content within the unit cell are shown in Figure 19a and Figure 19b, respectively, and correspond to the tails of the curves in Figure 14 and Figure 15 for the different values of *Re* and *Ca* studied in each of the cross-sections. The maximum steady state void content for each flow situation was observed to occur predominantly in either the $\bar{x} = 0$ or $\bar{x} = 1/2$ plane and therefore represents a worst-case scenario in terms of air entrapment. A volume average of the void content in the five different planes at their respective steady state conditions was used to calculate the average steady state void content values shown in Figure 19b and is representative of the approximate void content measurement that would be reported experimentally. The maximum steady state void content values (Figure 19a) of the cases studied all fall between the range of approximately two to six percent of the entire unit cell volume while the average steady state void content values (Figure 19b) all fall within the range of approximately one to four percent.

It is observed from the data in Figure 19a that the maximum void content occurs at low Reynolds numbers and high Capillary numbers, and progressively decreases for all *Re* as *Ca* is decreased to approximately 0.001 and then begins to increase again as *Ca* is further reduced. The approximately vertical nature of the contour lines in Figure 19a at the low and moderate *Ca* values suggest that the maximum void content in these cases has a greater dependency on *Ca* than on *Re*. This trend reflects the fact that the capillary forces at the resin-air interface increase in comparison with the inertial forces dominating the macro-flow paths as *Ca* decreases, causing the resin to permeate more rapidly into the fiber bundles and reducing micro-void formation. In contrast, as *Re* varies independent of *Ca* the ratio of inertia to viscous forces is changed, which appears to have a lesser effect on the resulting flow and final void content. The final average void content values shown in Figure 19b are all less than the maximum void content values (Figure 19a) at similar

57

flow conditions, and the different trends which occur in Figure 19a and Figure 19b throughout the ranges of *Re* and *Ca* studied suggests a moderate degree of spatial non-uniformity in the void content of the preform. The average void content in Figure 19b reaches a maximum of about four percent when both *Re* and *Ca* are either very high or low, and a minimum of less than one percent is observed at moderate values of both *Re* and *Ca*. The difference between the average and maximum void content results becomes increasingly drastic as *Re* and *Ca* are increased, pointing out a greater spatial nonuniformity in the void content under these flow conditions. Note that the processing window for achieving an average void content of less than one percent spans a Capillary number range of about one order of magnitude, while the Reynolds number spans a little less than two orders of magnitude to achieve the same void content. This is significant in considering the relative importance of both dimensionless groups when choosing processing parameters for LCM, where the smaller range of acceptable values for *Ca* indicates that this dimensionless group should be paid the most attention during process design.

In addition to the prediction of the final void content within the preform, it is critical to consider the excess time, $\bar{t}_{ex}$, needed for the void content to reach steady state after the first part of the flow front has reached the far end of the unit cell away from the inlet plane, so as to achieve the final void content values reported in Figure 19a and Figure 19b. In an ideal mold fill, the time scales of the macro-scale and micro-scale flows are equal such that the two flow regimes will be filled simultaneously. However, in an actual fill, the resin can race across the unit cell through the macro-scale channels or wick quickly into the micro-scale fiber bundles, resulting in an uneven resin flow front and additional resin flow being required to ensure that the macro- or micro-scale voids are filled (to their final extent). This additional processing time is defined here as the excess dimensionless flow time, $\bar{t}_{ex}$, and should be minimized during LCM applications to conserve time

and material. Figure 19c shows the excess flow time for each of the flow situations studied, where it is evident that the worst case scenarios using this metric occurs when the values of $Ca$ and $Re$ are both relatively high. As observed in Figure 19c, the approximately vertical nature of the contour lines at low and moderate $Ca$ values suggest that the excess dimensionless flow time is more dependent on $Ca$ than $Re$, as also mentioned above in the discussion of Figure 19a. The minimum excess time values occur at $Ca \cong 0.001$, which also roughly corresponds to the areas of minimum void content in Figure 19a and Figure 19b.

A comparison of Figure 19b and Figure 19c further shows that choosing conditions that lead to minimized average void content (e.g. ~1% for $Ca = 0.01$ and $Re = 1$ in Figure 19b) may come at the expense of significant resin wastage as determined by $\bar{t}_{ex} \approx 2$ in Figure 19c for the stated $Re$ and $Ca$ combination. From a processing perspective, however, both these values must be minimized simultaneously. To this end, Figure 19d presents the variation of the product of the normalized values of the final average void content (Figure 19b) and the excess dimensionless flow time (Figure 19c), $\phi_{avg}^{\infty} \cdot \bar{t}_{ex}$, as a function of $Ca$ and $Re$. The contours of the product function are the highest at combinations of large $Ca$ and $Re$, reflecting the high average void content and high nondimensional processing times occurring under these conditions in Figure 19b and Figure 19c. The minimum value of the combined consideration of the average void content and the excess resin flow time in Figure 19d is found centered around $Ca \approx 0.001$ and spanning from $5 \times 10^{-4} \lesssim Ca \lesssim 15 \times 10^{-4}$, and $Re \approx 50$ and spanning from $25 \lesssim Re \lesssim 100$. This most favorable processing window is the shaded light gray oval region in Figure 19d, and is presented as the superimposed dashed oval in Figure 19a–Figure 19c to illustrate the corresponding maximum void content, average void content, and excess flow time associated with this most favorable processing window. The numerical results summarized in Figure 19d suggest that designing the

mold-filling stage of preform permeation such that the *Ca* and the *Re* fall within this most favorable processing window would result in the minimum combination of both final void content (~1% average or ~2% maximum) and the dimensionless processing time (~0.1) for a Rovcloth 2454 woven fabric. The trends presented in Figure 19 provide an example of using the current numerical simulations as a decision making tool regarding processing parameters for preform permeation and the arrival at mold-filling designs that tradeoff between the competing effects involved in LCM processes. These results fulfill the first objective of this dissertation by presenting a numerical simulation of resin permeation in LCM processes, addressing the issue of void formation in composite molding processes. The second goal of this dissertation concerning the augmentation of the damping characteristics of composite materials through nanoscale reinforcement is dealt with in Chapter 4–Chapter 6.

## 3.6 Nomenclature used in Chapter 3

$a$      fiber bundle thickness [$m$]

$b$      fiber bundle height [$m$]

$Ca$      Capillary number

$F_{cap}$      capillary source term [$N/m^3$]

$F_{por}$      porous media source term [$N/m^3$]

$l$      unit cell length [$m$]

$p$      pressure [$Pa$]

$p_{c,l}$      longitudinal capillary pressure [$Pa$]

$p_{c,r}$      radial capillary pressure [$Pa$]

$r_f$      fiber filament radius [$m$]

$Re$      Reynolds number

$t$       time [$s$]

$\boldsymbol{u}$       velocity vector [$m/s$]

$v_f$       fiber bundle volume fraction

$x$       x-direction coordinate [$m$]

$y$       y-direction coordinate [$m$]

$z$       z-direction coordinate [$m$]


*Greek symbols*

$\alpha$       fluid volume fraction

$\eta$       resin-air meniscus location

$\theta$       contact angle [*degrees*]

$\kappa$       permeability [$m^2$]

$\mu$       viscosity [$Pa{\cdot}s$]

$\rho$       density [$Kg/m^3$]

$\sigma$       surface tension [$N/m$]

$\phi$       void content


*Superscripts/subscripts*

$^{-}$       dimensionless value

$_a$       air phase

$_{avg}$       average quantity

$_r$       resin phase

$_\infty$       steady-state value

**Chapter 4: Experimental Investigation of the Damping Enhancement in Fiber-reinforced Composites with CNTs**

This chapter investigates the damping effects of carbon nanotubes (CNTs) embedded in the matrix of fiber-reinforced composite materials. The composite materials are analyzed using dynamic mechanical analysis (DMA) and various modal analysis techniques to determine the damping characteristics of the composite as a function of strain, fiber volume fraction, and nanotube type and weight percentage loading. In addition, experiments are conducted using cantilevered beams in both a stationary and rotating frame in order to explore the effects of rotation on the damping behavior of the composite material.

**4.1 Composite Fabrication and Testing Methods**

Various lengths, diameters, and concentrations of CNTs are considered in the fabrication of different composite specimens, and an ultrasonic probe is used to disperse the as-received agglomerated CNTs throughout the resin. The effect of different ultrasonic processing times on the CNT dispersion is studied to determine the processing conditions which maximize the damping characteristics of the final composite. Four types of CNTs are used in the current study: one single-walled CNT (SWCNT) geometry and three different multi-walled CNT (MWCNT) geometries. The SWCNTs are purchased from SES Research (Houston, TX) with >90% purity and dimensions of <2 $nm$ in diameter, $D$, and 5–15 $\mu m$ in length, $L$, and the multi-walled CNTs are purchased from Nanolab (Waltham, MA) with >95% purity and dimensions of: (1) $D = 15$ $nm$ and $L = 5 - 20$ $\mu m$, (2) $D = 30$ $nm$ and $L = 5 - 20$ $\mu m$, and (3) $D = 30$ $nm$ and $L = 1 - 5$ $\mu m$. Each of the different nanotube types are obtained from the respective companies in large quantities from the same lot in order to minimize any variation that may occur between different production batches.

The composite samples are made via hand layup and compression molding, and the cured composites are tested using several different techniques to determine their material damping characteristics.

*4.1.1 Sample Preparation*

The composite samples are fabricated using a compression molding method in which the resin flows through the thickness of the part as it is being compressed to ensure uniformity of CNT dispersion throughout the sample. The CNT-epoxy mixture is prepared as follows: First, EPON 826 resin (Hexion Specialty Chemicals, Columbus OH) is mixed with Heloxy Modifier 68 (Hexion Specialty Chemicals, Columbus OH) using a ratio of 4:1 by weight in order to reduce the viscosity of the resin. Appropriate amounts of the resin and CNTs are then weighed into a beaker using an Ohaus Explorer Pro balance to achieve the proper CNT weight percentage, $\alpha$, in the epoxy. The nanotubes are then carefully mixed into the resin by hand using a medical grade utensil in order to ensure that the CNTs are integrated with the resin before transport from the balance. After this brief manual stirring, the resin-CNT combination is blended using an IKA T25 high-shear mixer for 90 seconds. A Cole-Parmer 500 watt ultrasonic processor with a 12.5 *mm* probe is then used to disperse the carbon nanotubes in the sample using a pulsed on-off mode with one second pulses for an optimum duration so as to maximize the damping in the final composite, as described in Chapter 4.2. Following sonication, an appropriate amount of Epikure 3274 hardener (Hexion Specialty Chemicals, Columbus OH) is added to the sample and immediately incorporated with the CNT-resin sample using manual stirring for two minutes and high-shear mixing for an additional 90 seconds. The entire resin sample is then transferred to a larger diameter beaker to increase the exposed surface area of the resin and degassed for 30 minutes.

A hand-layup technique combined with compression molding is applied to fabricate the composite sample, using a 3K plain weave carbon fiber fabric (Fibre Glast Development Corp, Brookville OH) with 12.5 picks and wefts per inch, a nominal thickness of 0.3 $mm$, and an areal weight of 193 $g/m^2$. The compression molding is carried out using a three-part aluminum mold consisting of a separable top section, a middle spacer frame, and a bottom plate, as shown in Figure 20a and Figure 20b. The top and bottom sections are sealed to the middle spacer using an O-ring fitted to a machined groove in each respective piece. Precise amounts of the epoxy-CNT mixture are poured between every two layers of carbon fiber fabric during the hand layup to minimize any filtering of the CNTs from the epoxy during the resin-permeation stage of the compression molding process. The sample is then processed using an MTP-10 programmable hot press (Tetrahedron Associates, San Diego, CA) using the following cure cycle: (1) the mold is held
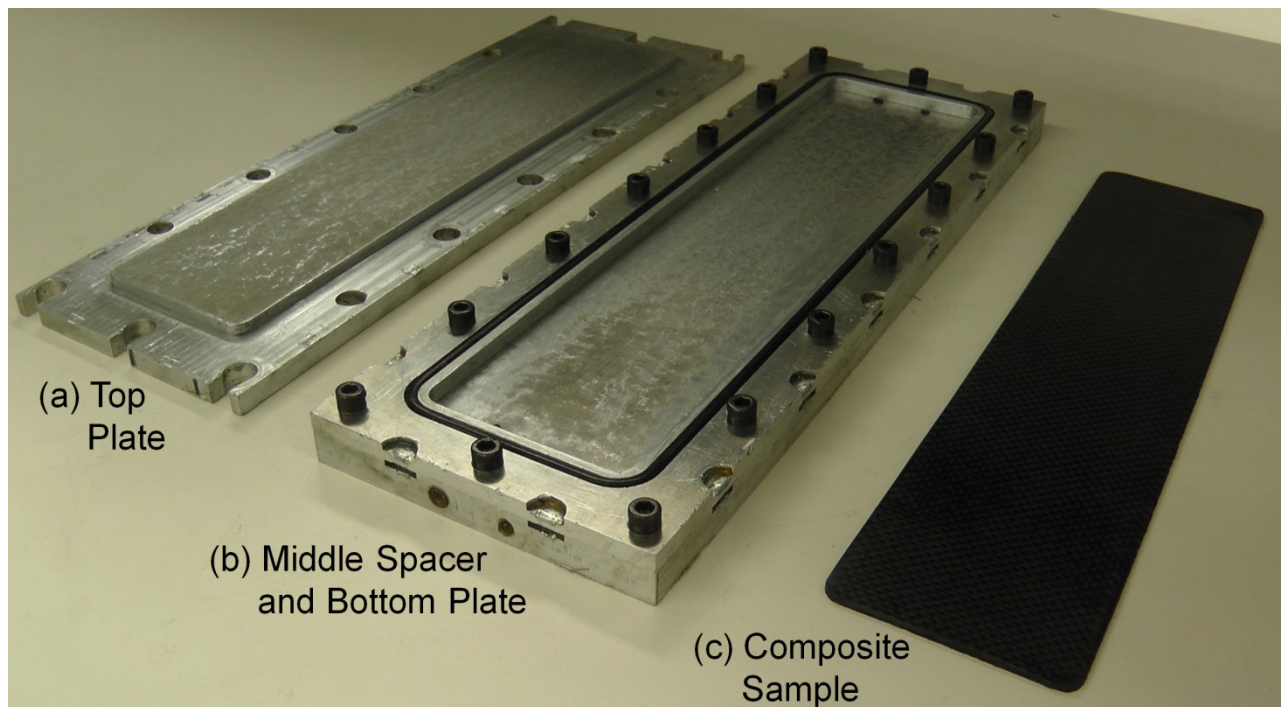


Figure 20: The aluminum mold used for fabricating the composite beams consisting of (a) a top plate and (b) a middle spacer and a bottom plate. A finished composite sample measuring 318 x 76 x 2 $mm$ is shown in (c).

at 40 ℃ and 40 *kN* for one hour, (2) the mold is then held under the same force while the temperature is ramped to 120 ℃ over a ten minute period, (3) after two hours at 40 *k*N and 120 ℃, the mold is then cooled to room temperature in 15 minutes and the cured composite specimen measuring 318 x 76 x 2 *mm* is removed from the mold, as shown in Figure 20c.

The fabricated rectangular plate sample is then cut using a diamond-bladed wet saw into long slender beams measuring 292 x 13 x 2 *mm* for vibration testing. In addition, random sections of each composite plate are cut into 40 x 20 x 2 *mm* sections, scored, frozen in liquid nitrogen, and fractured to create a surface for scanning electron microscope (SEM) evaluation of the CNT dispersion in the epoxy matrix. Composite samples are made following the above methodology using a range of materials and processing conditions as enumerated in Table 3. Each of the

Table 3: Range of values of carbon nanotube, fiber reinforcement, and ultrasonic processing parameters used in the experimental study.

| Sample | CNT | | | | Ultrasonic processing time, $t_p$ (*min.*) | CNT weight fraction, $\alpha$ (%) | Fiber volume fraction, $v_f$ |
| | Type | Length, L ($\mu m$) | Diameter, D (*nm*) | Aspect ratio (*L/D*) | | | |
|---|---|---|---|---|---|---|---|
| 1 | | | | | | | 0.00 |
| 2 | | N/A | | | 0 | 0 | 0.46 |
| 3 | | | | | | | 0.58 |
| 4 | | | | | | | 0.00 |
| 5 | | | | | | 1 | 0.46 |
| 6 | MWCNT | 5–20 | 15 | 833 | 10 | | 0.58 |
| 7 | | | | | | | 0.00 |
| 8 | | | | | | 2 | 0.46 |
| 9 | | | | | | | 0.58 |
| 10 | MWCNT | 5–20 | 30 | 417 | 10 | 1 | 0.46 |
| 11 | | | | | | 2 | |
| 12 | MWCNT | 1–5 | 30 | 100 | 10 | 1 | 0.46 |
| 13 | | | | | | 2 | |
| 14 | SWCNT | 5–15 | 2 | 5000 | 5 | 1 | 0.46 |
| 15 | | | | | | 2 | |

samples are tested as described in Chapter 4.1.2 to obtain the results presented and discussed below.

### 4.1.2 Damping Measurement

A TA Q800 (TA Instruments, New Castle DE) dynamic mechanical analysis (DMA) system is used in the dual-cantilever mode to measure the material loss factor, $\delta$, of each composite sample in a stationary frame of reference. Experiments are carried out using a constant excitation frequency of 1 *Hz*, and the beam is swept through a range of different strain values to determine the material damping as a function of strain. Traditional modal analysis techniques [99]—specifically base excitation and modal hammer tests—are also performed using different boundary conditions and clamps to verify that the measurements are independent of testing conditions. In these cases, the damping measurement is expressed using the damping ratio, $\zeta$, where the material loss factor and the modal damping can be approximately related by $\delta = 2\zeta$ [100]. These tests elucidate the effects of CNT type, CNT weight percentage, strain, and fiber reinforcement on the resulting damping measurements as presented in Chapter 4.3.

To measure the CNT damping in the composite material during rotation, an experimental test stand is developed as shown in Figure 21a to mount and rotate two thin cantilever beams on opposite sides of a central shaft up to angular velocities of 500 RPM. As seen in Figure 21a, the beams extend lengthwise parallel to the plane of rotation and are protected by acrylic tubing to avoid the effects of aerodynamic damping on the beam during rotation. The central shaft is connected to a brushed DC motor (Magmotor, Worchester, MA) which is mounted to the underside of a raised aluminum platform and controlled via a proportional-integral-derivative (PID) algorithm developed in the data acquisition and control system Labview™ (National
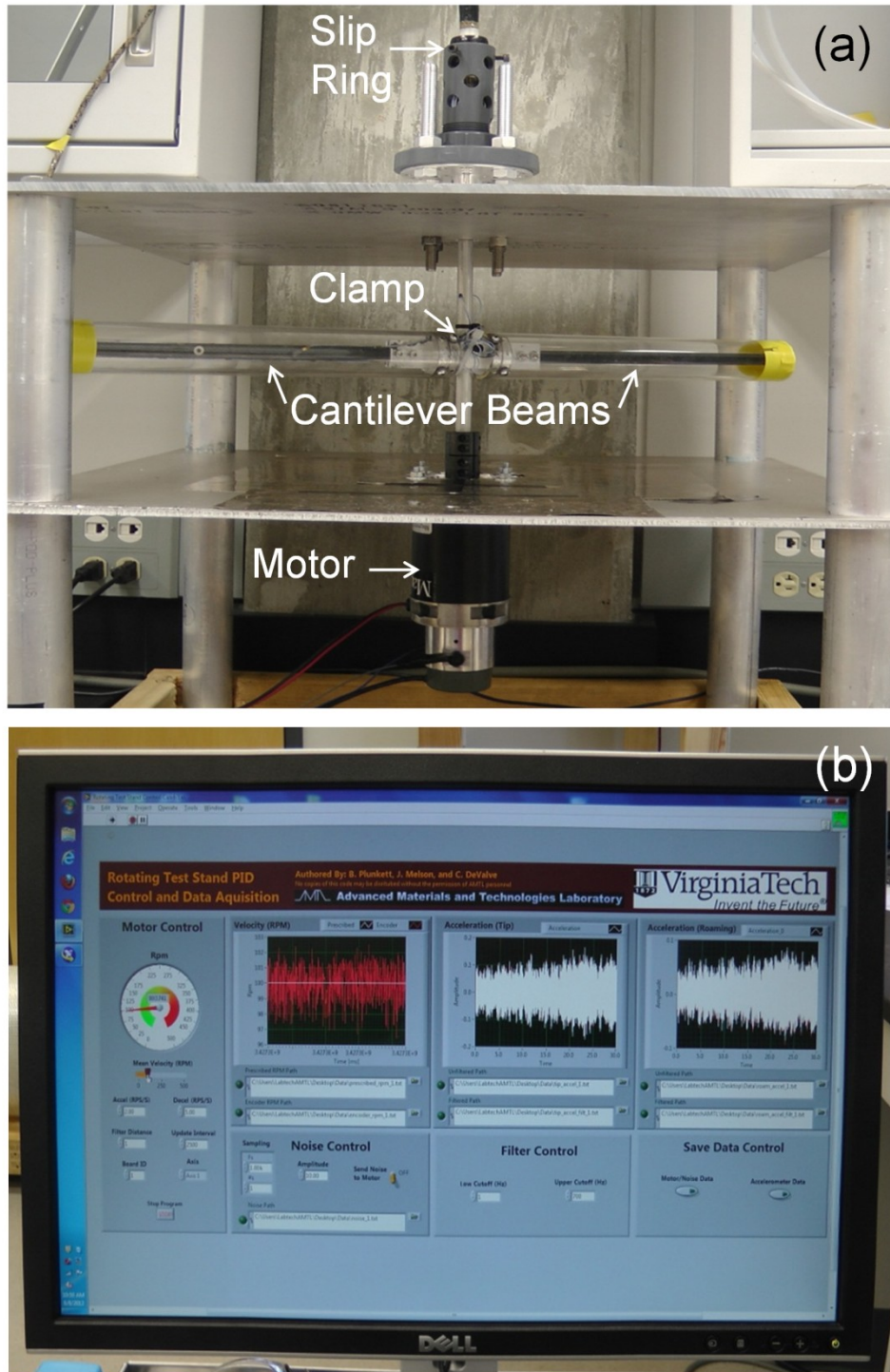
Figure 21: (a) The experimental rotating test stand, consisting of an aluminum frame, a DC motor, two cantilever beams mounted using a clamp connected to the central rotating shaft, and a slip ring routing the signals from the accelerometers to the Labview™ control board. (b) The Labview™ user interface for controlling and monitoring the motor velocity profile, as well as for displaying and saving the vibration data from the rotating beams.

Instruments, Austin, TX) with a user interface as shown in Figure 21b. The vibrations of the beams are measured during rotation using two miniature ICP accelerometers (PCB Piezotronics, Depew, NY) and 30 seconds of continuous data is recorded using a sampling rate of 1800 samples per second. The location of the first accelerometer is fixed at the tip of the beam for all the experiments, where the second "roving" accelerometer is positioned variably along the length of the beam at precise increments during different experimental measurements to verify the mode shapes of the beam. The accelerometers are powered by an external current source (Dytran Instruments Inc., Chatsworth, CA), and the signal from the test rig is passed through a liquid mercury slip ring (Mercotac, Carlsbad, CA) at the top of the rotating test stand (shown in Figure 21a) and fed through an analog low-pass filter (DL Instruments, Ithaca, NY) before being recorded by the Labview™ data acquisition system. Uniform white noise of $\pm 10$ RPM is added to the constant RPM motor control signal in order to randomly excite the base of the beam during operation, creating an input condition that maximizes the effectiveness of the operational modal analysis (OMA) technique [101−103] which assumes that the system is subject to random excitation. The vibration measurements are taken from the test setup at incremental angular speed values and the data is compiled and analyzed using the stochastic subspace identification unweighted principle component (SSI-UPC) algorithm [104,105] in the OMA software package ARTeMIS™ (Structural Vibration Solutions, Denmark) to extract the modal parameters of the system. The results of the damping measurements using the various test methods described in this subsection are presented and discussed in Chapter 4.4.

## 4.2 CNT Dispersion

In order to maximize the benefits of the CNTs in the final composite material, individual nanotubes should be distributed as evenly as possible throughout the resin by completely dispersing the as-received CNT agglomerates without breaking the individual CNTs. Various techniques are available for dispersion as reviewed in [106], of which a mechanical method using energy generated from an ultrasonic probe is employed in this work to disperse the nanotube agglomerates. For effective dispersion, it is important to understand the effects of ultrasonic processing time on the dispersion of the CNTs throughout the resin and, in turn, the effects of the different dispersion states on the CNT-induced damping in the resulting composite material. As the resin-CNT mixture is ultrasonically processed for an increasing amount of time, two competing effects take place within the sample: (1) the agglomerated CNTs are increasingly dispersed and approach conditions in which the individual CNTs are evenly distributed throughout the resin, maximizing their effectiveness in improving the material properties of the overall composite, and (2) the individual CNTs are increasingly broken apart and become shorter, approaching conditions resembling amorphous carbon if processed for too long and thus nullifying the potential benefits of the CNTs to the material. Therefore, it follows that a balance of these two effects should occur using an intermediate processing time of the sample where the CNTs are significantly dispersed without considerable breakage of the individual nanotubes, maximizing the CNT damping effect in the final composite.

A systematic investigation is carried out using ultrasonic processing times in 2.5 minute increments up to 30 minutes on separate resin samples with one weight percent SWCNTs and MWCNTs (30 $nm$, 5–20 $\mu m$). In all the cases, a 12.5 $mm$ probe is employed as the dispersing instrument and the ultrasonic power is held constant at 500 $W$. The ultrasonically dispersed CNT-
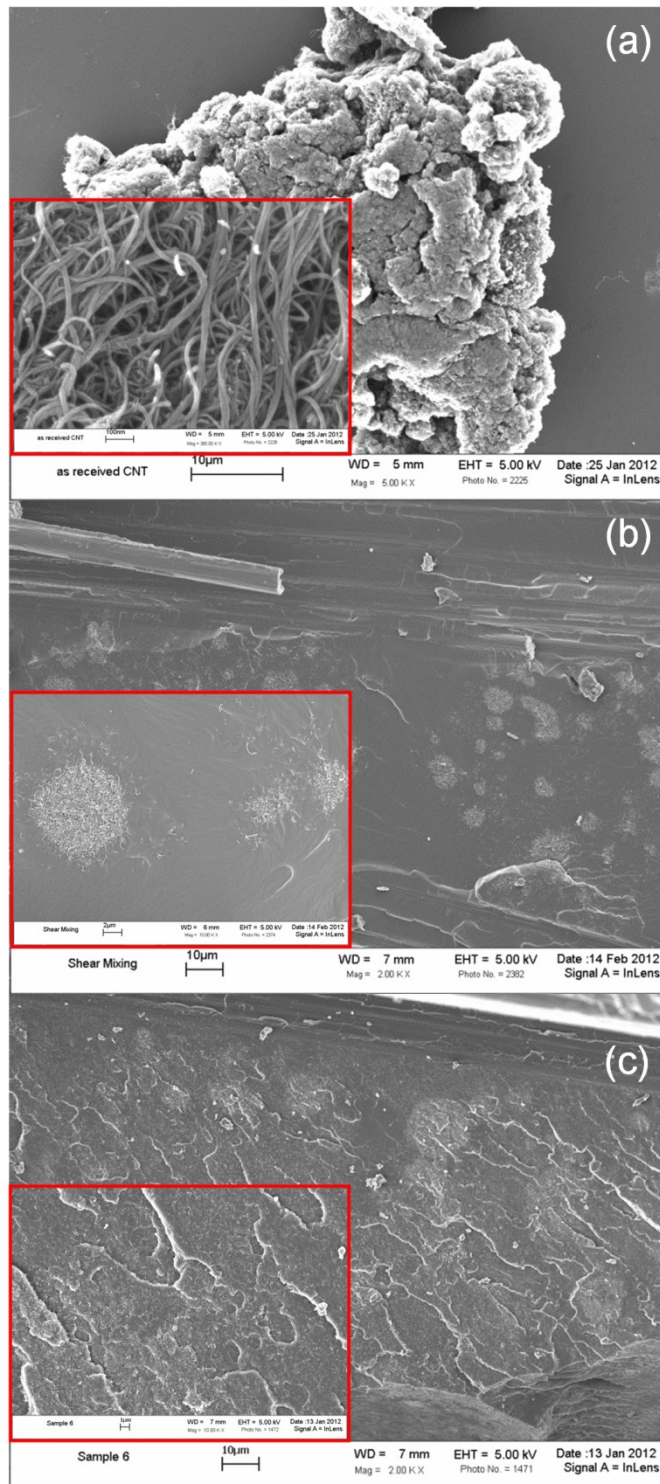
Figure 22: Scanning electron microscopy images of the (a) as received SWCNTs depicting large agglomerates, and fracture surfaces of the epoxy-CNT composite showing the relative nanotube dispersion after (b) shear mixing (no ultrasonic processing) and with (c) shear mixing and 10 minutes of ultrasonic processing using a 12.5 *mm* probe

resin samples are then used to fabricate carbon fiber reinforced composites plates with a $v_f = 0.46$, and three random samples from two separate composite plates for each case are imaged using scanning electron microscopy (SEM) to examine the CNT dispersion. These samples are further tested using DMA in the dual-cantilever mode at 1 $Hz$ to determine the average damping for each case, which is reported as the material loss factor, $\delta$, in the presentation of the results.

To first qualitatively investigate the CNT dispersion in the composite matrix, the cured nanotube-epoxy sample is sputter-coated with gold for one minute using a Cressington HR 208 (Cressington Scientific Instruments, England) and imaged using a Leo 1550 Field Emission SEM (Carl Zeiss Microscopy, Germany). Figure 22a presents the micrograph of a SWCNT agglomerate, as received from SES Research, untreated and unmixed into any solution, where the main image is shown at a magnification level of 5,000 times and the inset is magnified by 300,000 times. It is evident from Figure 22a that an extremely large quantity of the as-received nanotubes are highly entangled and intertwined with each other (i.e. agglomerated), and individual nanotubes are almost indecipherable from one another. Figure 22b and Figure 22c illustrate the effect of ultrasonic processing on the SWCNT dispersion in the resin by presenting a fracture surface of two different composites, one in which the SWCNT-resin mixture is simply shear mixed (Figure 22b) and the other being shear mixed and ultrasonically treated for 10 minutes (Figure 22c). The main images in both Figure 22b and Figure 22c are magnified by 2,000 times, and the inset figures are shown at a magnification level of 10,000 times. The sample which is shear mixed in Figure 22b shows evidence of significant remaining agglomeration, seen as the light white circles ranging in diameter from about 2 to 10 microns. However, it is evident that the size of the initial agglomerate in Figure 22a of about 60 microns has been reduced by approximately an order of magnitude as a result of the shear mixing. In Figure 22c where the sample has been shear mixed and ultrasonically
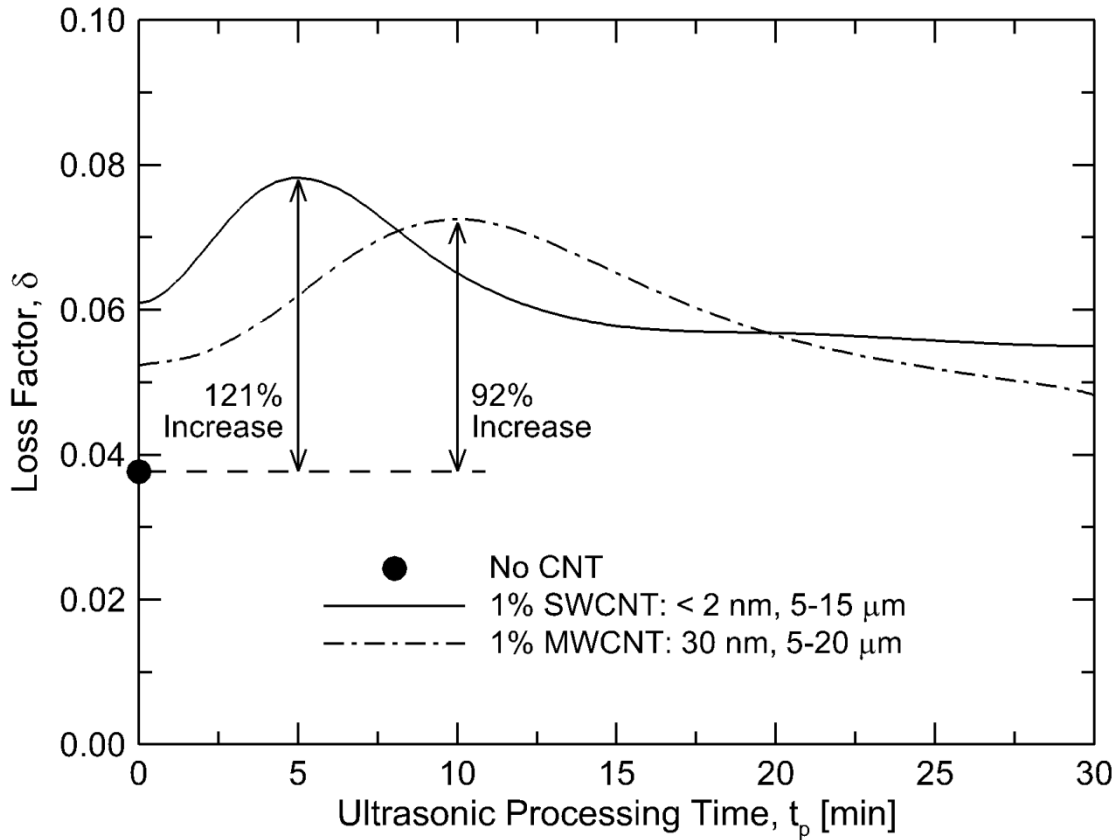
Figure 23: Variation of the material damping loss factor, $\delta$, with the ultrasonic processing time, $t_p$, for a carbon fiber reinforced composite with $v_f = 0.46$ and one weight percent CNT loading.

agitated, the SWCNTs appear to be much more dispersed with only a few small areas of remaining agglomeration, which is further illustrated by the inset of this subfigure. Figure 22 serves as a qualitative illustration of the SWCNT dispersion in the composite sample as a result of the different mixing steps, and demonstrates evidence that the CNTs are indeed being mostly deagglomerated in the resulting composite samples using the ultrasonic processing method.

The effect of the ultrasonic processing time, $t_p$, on the damping characteristics of the CNT-infused composite material is quantitatively presented in Figure 23, where the SWCNT results are shown by the solid line and the MWCNT results are presented using a dash-dotted line. The loss factor data in this plot is gathered using DMA at 1 *Hz* using a controlled strain, $\varepsilon$, test method with

$\varepsilon = 0.025\,\%$. The solid circle shown on the y-coordinate axis at a loss factor value of approximately 0.37 denotes the damping measured in the baseline composite without CNTs, and serves as a reference for quantifying the damping enhancement. Note that since all the samples are shear-mixed prior to ultrasonic dispersion, $t_p = 0$ in Figure 23 denotes the damping in the composite beams processed using only shear mixing without ultrasonic processing.

As the ultrasonic processing time is increased from zero, the measured damping in the composite increases in both beams with SWCNTs and MWCNTs. This trend reflects an increase in the CNT dispersion throughout the matrix with increasing $t_p$ (as presented in Figure 22), which consequently increases the total matrix-CNT interfacial area and results in more available stick-slip surfaces and greater damping in the overall composite. The SWCNT-infused composite achieves a maximum of a 121% increase over the baseline beam, which occurs at an ultrasonic processing time of $t_p = 5$ *min*. A similar trend is seen for the composite beams with MWCNTs, where a 92% maximum increase in damping is evident using an ultrasonic processing time of $t_p = 10$ *min*. However, as the ultrasonic processing times of each sample are further increased, the damping is observed to decrease in both cases, leveling off in the composite with SWCNTs as the processing time approaches 30 minutes. The damping in the MWCNT beam also decreases for larger $t_p$ values and reduces to lower levels of damping than the SWCNT beam after about 20 minutes of processing. The trend in the MWCNT composite beam demonstrates a continuing decrease with time beyond 30 minutes of processing, indicating that the damping in the composite could eventually approach the baseline value of the beam without CNTs if $t_p$ is further increased. Similar studies are conducted for the other two MWCNT types (30 *nm*, 1–5 *μm* and 15 *nm*, 5–20 *μm*) and the damping is found to be maximized for $t_p = 10$ min in both cases; these results are excluded from Figure 23 for brevity.

## 4.3 Damping in Cantilevered Beams

Using the ultrasonic processing times determined so as to maximize the damping in the composite for each type of CNT, systematic experimental studies are conducted over the range of carbon nanotube, fiber reinforcement, and ultrasonic processing parameters enumerated in Table 3. All four CNT types and dimensions are first considered at weight fractions of $\alpha = 1\%$ and 2% for a fixed fiber volume, $v_f$, of 0.46. In each case, the loss factor damping, $\delta$, is measured as a function of strain, $\varepsilon$, using DMA in the dual-cantilever mode at 1 *Hz* as presented in Figure 24a–Figure 24d. In each subfigure, the solid and the dashed lines represent $\alpha = 2\%$ and 1%, respectively, and the dash-dotted line denotes the baseline composite beam without CNTs.
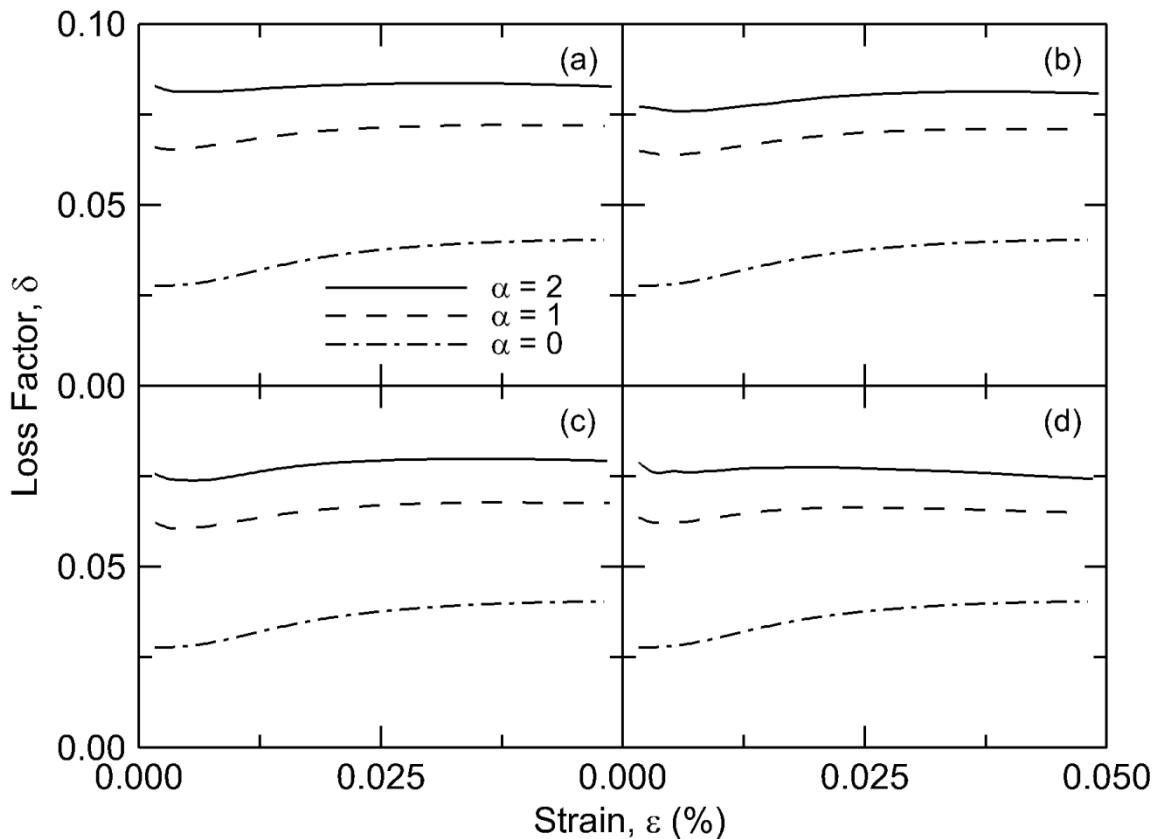


Figure 24: Variation of the material damping loss factor, $\delta$, with strain, $\varepsilon$, using various CNT weight percentage loadings, $\alpha$, for (a) SWCNTs with dimensions of < 2 *nm* in diameter and 5–15 *μm* in length, and MWCNTs measuring (b) 15 *nm* in diameter and 5–20 *μm* in length, (c) 30 *nm* in diameter and 5–20 *μm* in length, and (d) 30 *nm* in diameter and 1–5 *μm* in length.

The measured damping variation with strain for the SWCNT-reinforced composite beam with $v_f = 0.46$, presented in Figure 24a, demonstrates that, in general, the damping in the beam increases with increasing strain. In addition, the damping in the beam is seen to increase as the weight increase is measured for $\alpha = 2\%$. These results indicate that the damping enhancement is nonlinear with the increase in the nanotube weight percentage, with the difference in damping fraction of SWCNTs is increased—using SWCNTs with $\alpha = 1\%$, the measured damping is observed to increase by an average of 95% over the beam without CNTs, and an additional 38% from zero to one percent CNTs being much more than the increase from one to two percent CNTs. Accordingly, it is expected that the damping benefits of adding higher weight percentages of CNTs to the composite matrix would eventually level off and further addition of CNTs will likely not affect the damping in the composite material significantly.

The trends in the damping variation with strain for composite samples containing MWCNTs with aspect ratios (*L/D*) of 833, 417, and 100 are presented in Figure 24b–Figure 24d, respectively, and exhibit similarity to the SWCNT results in Figure 24a, in that the damping increases with both increasing strain and increasing CNT weight percentage loading: for the MWCNTs with an aspect ratio of 833 (Figure 24b), the damping is increased by approximately 98% and 120% with $\alpha = 1\%$ and 2%, respectively; in Figure 24c, for MWCNTs with an aspect ratio of 417, the damping with $\alpha = 1\%$ and 2% is increased by about 96% and 117%, respectively;  MWCNTs with the lowest aspect ratio of 100 (Figure 24d) demonstrated an increase in damping of 81% and 112% using one and two weight percent CNTs, respectively. Considering that the SWCNTs have an aspect ratio of 5,000, there is a noticeable correlation relating an increase in damping enhancement with an increase in the CNT aspect ratio, at both CNT weight percentages considered in the current study. This trend may be explained by noting that as the aspect ratio increases, the total surface area of

the nanotubes within the resin increases as well, offering more continuous stick-slip surfaces which contribute to the damping in the composite, a trend also noted in [54,78]. The plots in Figure 24 demonstrate that using a weight fraction of 2% SWCNTs in a carbon fiber reinforced composite with $v_f = 0.46$ resulted in the greatest measured damping increase of about 133%, demonstrating a significant increase in performance of the functional composite material.

The effect of fiber-reinforcement on the loss factor damping of the composite material is studied using three different $v_f$ values of 0, 0.46, and 0.58, and the results are summarized in Figure 25. Multi-walled CNTs (30 *nm*, 5–20 *μm*) with an aspect ratio of 833 are chosen as the
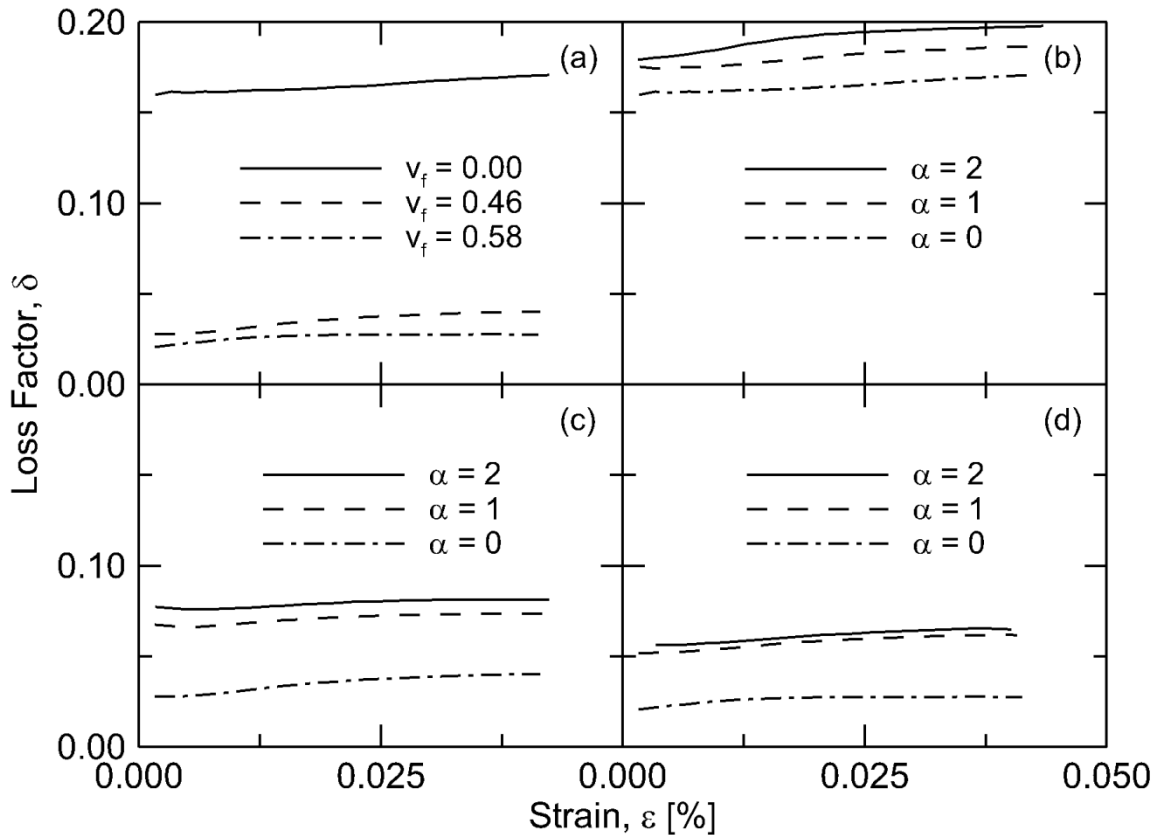


Figure 25: Variation of the material damping loss factor, $\delta$, with strain, $\varepsilon$, using (a) no CNT and varying the fiber volume fraction of the composite material, as well as using various weight percentages of MWCNTs (15 *nm* in diameter, 5–20 *μm* in length) with constant $v_f$ values of (b) 0.00, (c) 0.46, and (d) 0.58.

nanoscale reinforcement based on their similar damping qualities to SWCNTs but at a lower cost and greater availability in large batch sizes. Figure 25a presents the effect of the carbon fiber reinforcement without CNTs ($\alpha = 0\%$) on the material damping. The solid line represents the composite material made out of only epoxy resin with no fiber reinforcement or CNTs, and the damping in this case is quite high, averaging a loss factor of approximately 0.16. However, when the fiber reinforcement is added to the resin, the damping is observed to decrease dramatically, where the dashed and dash-dotted lines signify $v_f$ = 0.46 and 0.58, respectively, and show a corresponding decrease in damping of 78% and 84% relative to the neat epoxy resin. The damping in the beam decreases as a result of the fiber addition because of the added rigidity to the sample from the carbon fiber reinforcement and consequent increase in the specific strength to stiffness ratio, which is generally noted to result in a material with decreased vibration damping characteristics and has been observed in similar composite material studies [47,76,78].

The effect of various CNT weight fractions is explored by considering the three different $v_f$ values of 0, 0.46, and 0.58, as presented in Figure 25b–Figure 25d, respectively. For the composite without fiber reinforcement shown in Figure 25b, the measured values of the loss factor are quite high and range from 0.16 to 0.20. The damping is steadily augmented as the CNT weight fraction is increased, where the CNT-infused resin material with $\alpha = 2\%$ has a loss factor measuring almost 0.20 at high strain. In Figure 25c and Figure 25d corresponding to $v_f$ = 0.46 and 0.58, respectively, the overall damping qualities of the composite are reduced as the composite is reinforced with carbon fiber weave material, similar to the trends in Figure 25a. However, with increasing weight fraction of CNTs in the matrix of the composite material at these high $v_f$ values, a damping enhancement is clearly evident over the respective baseline beams in each case. In Figure 25c, with $v_f$ = 0.46, the baseline beam without CNTs and only carbon fiber reinforcement

has a loss factor averaging about 0.036. When one weight percent CNT is added to the beam, the loss factor almost doubles and increases to approximately 0.071, and a loss factor of 0.080 is achieved with two weight percent CNTs. Similarly, in the case of $v_f = 0.58$ shown in Figure 25d, the loss factor increases from 0.026 with no CNTs to 0.058 with $\alpha = 1\%$ and to 0.062 with $\alpha = 2\%$.

From the trends in Figure 25b–Figure 25d it is also evident that the difference between the damping values for one and two weight percent CNTs decreases as $v_f$ is increased, signifying that increasing the CNT loading is less effective in enhancing the damping in the resulting material at higher fiber volume fractions. This trend is most likely a result of the decrease in overall CNTs throughout the resin combined with the increased rigidity of the composite as the fiber volume fraction increases. In summary, the results in Figure 25 demonstrate that a relatively small amount of CNTs incorporated into the matrix of fiber reinforced composites can result in a significant increase in the damping properties of the material, and that, although the effect of CNT damping decreases as $v_f$ is increased, matrix-embedded CNT can provided substantial damping enhancement even in high $v_f$ composites.

The damping measurements on a cantilevered beam presented in Figure 24 and Figure 25 may be correlated to an empirical fit of the measured data to describe the material loss factor, $\delta$, of the composite material as a function of CNT weight percentage, $\alpha$, strain, $\varepsilon$, and fiber volume fraction, $v_f$, as:

$$\delta = (0.168e^{-2.66v_f} + 0.0355\alpha^{0.172})\varepsilon^{\left(0.0118e^{2.46v_f} + 0.0308e^{-1.11\alpha}\right)} \qquad (26)$$

where the constants are determined to fit the measured data with a root mean squared error of less than $5.16 \times 10^{-3}$. Equation 26 is valid for the range of parameters considered in the experimental studies: material strain values from 0 to 0.05 percent, fiber volume fractions of 0 to 0.58, and CNT

weight percentage loadings of zero to two weight percent. The power-law form of the equation reflects the monotonic increase in the material loss factor with increasing strain, noted in Figure 24 and Figure 25. In addition, the constants in Equation 26 designate that the loss factor increases with increasing CNT weight fraction and decreases as the volume fraction of the fiber reinforcement is increased, reproducing the trends observed in Figure 24 and Figure 25. Equation 26 serves as a quantitative tool for relating the loss factor damping as a function of the aforementioned material design parameters, and may be used in computational modeling of composite systems with embedded carbon nanotubes.

## 4.4 Damping in Rotating Beams

The effect of rotation on the characteristics of the CNT-infused composite materials is explored using the rotating test stand described in Chapter 4.1.2, where the beams are tested at different angular velocities ranging from 0 to 500 *RPM* in increments of 100 *RPM*. Carbon fiber reinforced composite beams with matrix-embedded SWCNTs are considered using two different $v_f$ values of 0.46 and 0.58, and aluminum beams of the same dimensions are used for a baseline material. For each case, three different beams are tested to calculate the natural frequency and damping values in each of the first three transverse modes of vibration.

A study is first conducted to validate the rotating experimental test rig by considering the effects of different test methods and clamping conditions on the damping measurements of the beams, where the results are summarized in Figure 26. As a baseline material, several beams are machined out of 2024 aluminum to match the dimensions of the composite beams described in Chapter 4.1.1, and modal hammer and base excitation tests are performed on both the aluminum and composite beams using free-free and clamped-free boundary conditions with several different
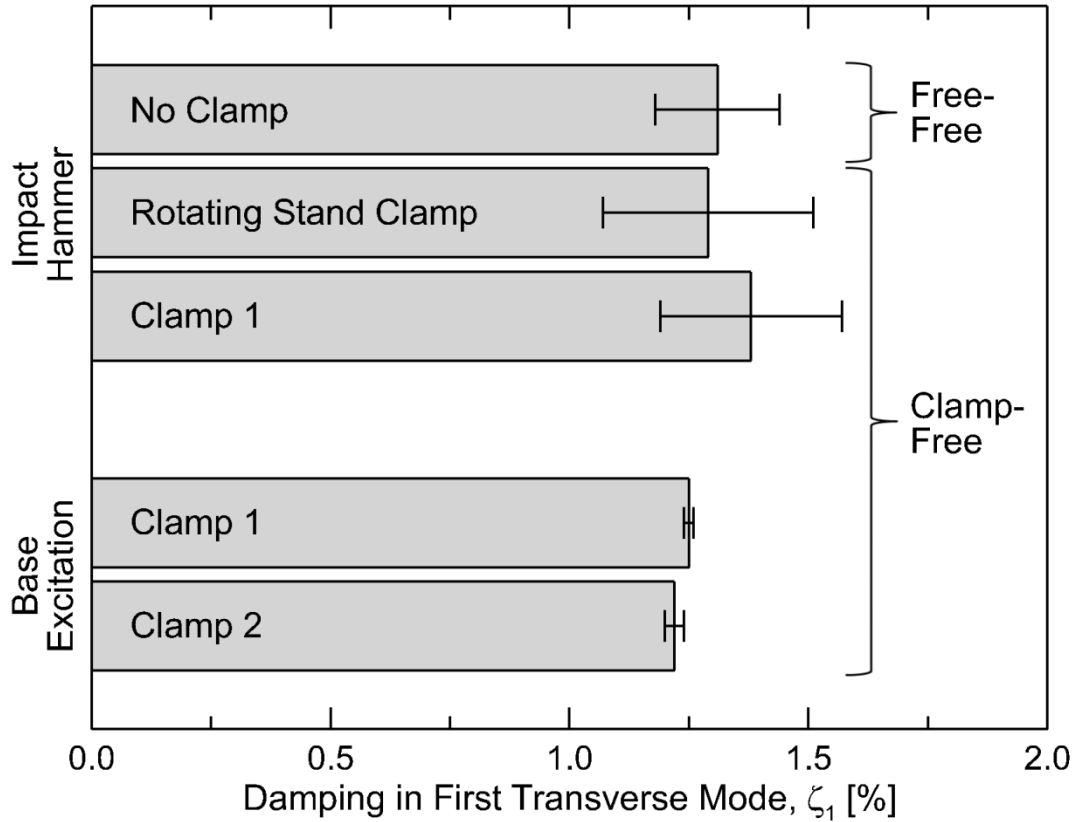
Figure 26: Comparison of the damping measured in the first mode of the composite beam with $v_f = 0.46$ and no CNT using various testing conditions as indicated.

clamps. The frequency response of the different materials is measured and computed using a Siglab™ control interface (Spectral Dynamics, San Jose, CA), and the damping ratio in the first mode, $\zeta_1$, is calculated using the half power technique [99,100] and applied as a comparison metric among the various test cases. The trends in each case of the aluminum beam and the composite beam with $v_f = 0.46$ and no CNTs are similar and, therefore, only the results for the composite beam are presented in Figure 26 for brevity.

The validation test methodology is described as follows: First, an impact hammer is used to excite a free-free beam and modal analysis is performed on the resulting data to measure the damping in the composite (top bar in Figure 26) to isolate any clamping effects before moving to a clamped-free configuration. Next, the beams are further tested as cantilevers by mounting one end

in the rotating test stand clamp and excited via an impact hammer test (second bar from the top in Figure 26), where this identical experiment is then repeated using the same beam mounted to a stationary clamp denoted as clamp 1 (third bar from the top in Figure 26). Finally, clamp 1 is mounted to a shaker (second bar from the bottom in Figure 26) and the beams are tested by means of base excitation, where this same test is repeated using an additional stationary clamp denoted as clamp 2 (bottom bar in Figure 26). Using the damping measurements of the free-free beam as a standard, the results in Figure 26 demonstrate that the damping in all cases is measured to be approximately 1.25% and there is no statistically significant difference between the results of the
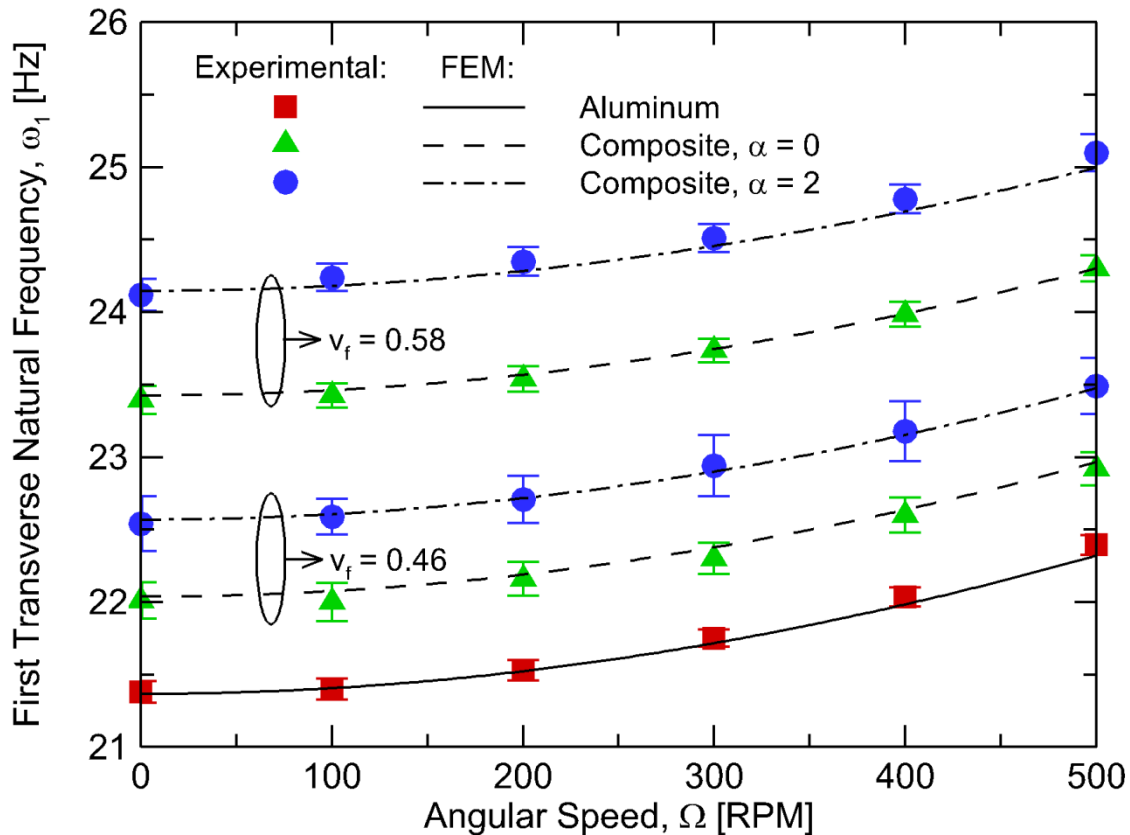


Figure 27: The first transverse natural frequencies of the aluminum and composite beams with $\alpha = 0\%$ and $\alpha = 2\%$ SWCNTs as a function of angular speed. The symbols and associated error bars indicate the experimentally measured values and the lines indicate the predicted natural frequencies using a finite element model (FEM) for each of the various materials.

free-free tests or any of the clamped-free tests for the composite beam. The standard deviation of the measured damping values for the base excitation results are very small, and the standard deviation is relatively larger for the damping measured using the impact hammer tests but still within acceptable limits for the high variation normally found between damping measurements. From the results in Figure 26 it is evident that the clamp used on the rotating test stand produces similar results to the other test clamps and methods, and therefore it is reasonable to assume that the rotating test stand and clamp do not significantly affect the modal damping measurements reported throughout the remainder of this subsection of the study.

Figure 27 presents the natural frequencies of the first transverse mode of vibration, $\omega_1$, for the aluminum and composite beams as a function of angular speed, $\Omega$. The results for the composites with the two different $v_f$ are indicated in the figure, and the experimental measurements and standard deviation error bars of the aluminum beam are shown by the square markers. The composite beam with $\alpha = 0\%$ is denoted by the triangle markers, and the circle markers signify the composite beam with $\alpha = 2\%$. A finite element model (FEM) is used to predict the natural frequencies for each different beam as a function of angular speed, where the solid line represents the results of the aluminum beam, and the composite beams with zero ($\alpha = 0$) and two ($\alpha = 2$) weight percent SWCNTs are shown by the dashed and dash-dotted lines, respectively. The results in Figure 27 indicate that the natural frequency of each beam increases with increasing angular speed ($\Omega$). In general, this trend demonstrates that the beams act stiffer as the centrifugal forces from rotation increase, known as the spin-stiffening effect [107]. The trend of the natural frequency as a function of angular speed also appears to be exponential in nature, since the natural frequency of the beams increases more rapidly as the angular speed increases steadily. The aluminum beam displays the lowest natural frequency values, and $\omega_1$ increases for the composite

82

beam with $v_f = 0.46$ and further increases when $v_f = 0.58$ as a result of the increased stiffness of

the beam with additional fiber reinforcement. For each respective fiber volume fraction, the natural

frequency of the composite beam also increases with the addition of two weight percent SWCNTs

to the composite matrix, which indicates that the high modulus of the CNTs (~*TPa*) causes an
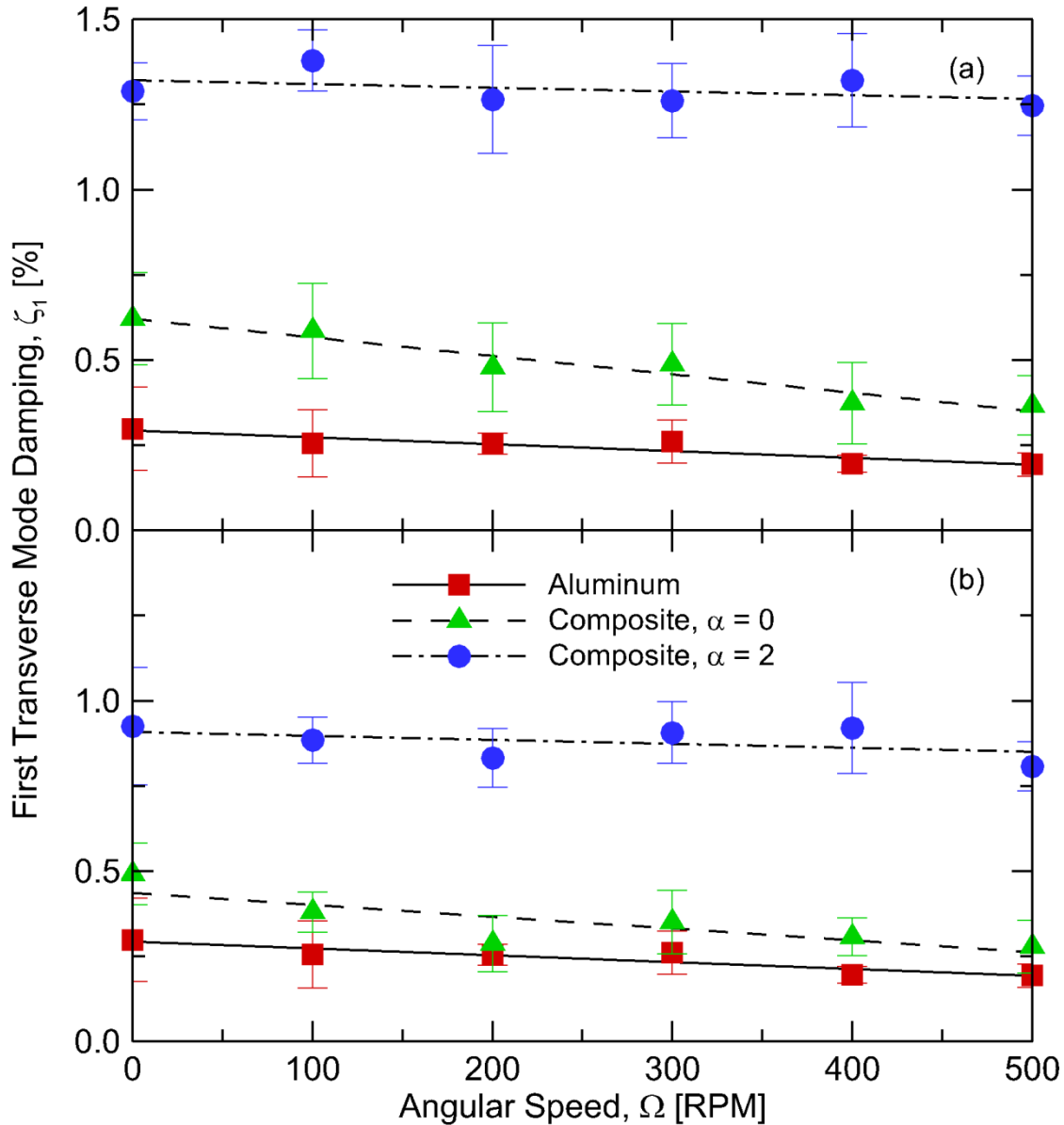


Figure 28: The measured damping in the first transverse mode of vibration for the aluminum and composite beams with $\alpha = 0\%$ and $\alpha = 2\%$ SWCNTs as a function of angular speed for $v_f =$ (a) 0.46 and (b) 0.58. The experimentally measured values are denoted by the symbols and associated error bars, and the lines represent linear regression fits through the respective data.

increase in the overall stiffness of the composite material. It is important to note that the experimental measurements of the natural frequency are in very good agreement with the values predicted from the finite element model, which further supports the validity of the data being collected and analyzed from the rotating experimental apparatus.

The measured damping in the first transverse mode of vibration for the aluminum and composite beams are shown in Figure 28 as a function of angular speed, $\Omega$, where the composite samples with $v_f = 0.46$ are shown in Figure 28a and the composites with $v_f = 0.58$ are presented in Figure 28b. As in Figure 27, the square markers and the solid line denote the aluminum beam, the composite beam without SWCNTs is shown by the dashed line and the triangle markers, and the circle markers and the dash-dotted line represent the composite beam with $\alpha = 2$. Note that the solid, the dashed, and the dash-dotted lines in Figure 28 are linear regression fits through the respective data. In addition, the standard deviation of each damping measurement for the various test conditions is shown by the respective error bars on each data point in Figure 28.

The damping values of the aluminum beam in Figure 28 serve as a baseline for comparing the trends of the different composite beams, as aluminum is a well-understood material with linear material properties under the current excitation conditions [108–110]. As $\Omega$ is increased from zero, the damping measured in the aluminum beam tends to decrease linearly from a value of approximately 0.30 to about 0.19 when $\Omega = 500$ RPM. Similarly, for the composite beam in Figure 28a with $v_f = 0.46$ and no CNT, the damping measured in the beam tends to decrease as the angular speed is increased, a trend which has been observed in similar studies [111,112]. Note that the damping values for the composite beam with no CNTs and $v_f = 0.46$ range from 0.62 to 0.37 and are significantly greater than those of the aluminum beam. Figure 28a further reveals that the magnitude of the slope of the linear variation indicates that for the composite with no CNT, the

84

damping decreases as a function of $\Omega$ more sharply than for the aluminum beam. The data for the composite beam with $\alpha = 2$ and $v_f = 0.46$ shows a considerable increase in damping over the composite beam without CNT at the same fiber volume fraction, ranging from 1.38 at $\Omega = 0$ RPM to 1.24 at $\Omega = 500$ RPM. As in the other materials, the damping in the beam decreases as the angular speed is increased, but the slope of the linear variation demonstrates that the decrease in damping is not nearly as large as in the case of the composite without CNT. Trends similar to those observed in Figure 28a with $v_f = 0.46$ are seen in the damping measurements of the composite beam with $v_f = 0.58$, presented in Figure 28b. However, a primary difference is observed in the magnitude of the damping values between the two $v_f$ cases in Figure 28a and Figure 28b, where the 0.58 fiber volume fraction composites have lower damping characteristics for similar nanotube weight percentage values. In the case of $v_f = 0.58$ with no CNT loading the damping values range from 0.49 at $\Omega = 0$ *RPM* to 0.28 at $\Omega = 500$ *RPM*, and from 0.93 to 0.81 when two weight percent SWCNTs are incorporated into the composite matrix. Also, the magnitude of the slopes for the composite beam data with $v_f = 0.58$ are smaller than those for the composite with $v_f = 0.46$, indicating that the damping characteristics of the composite material are less dependent on the angular velocity at increasing fiber volume fractions.

The data presented in Figure 28 indicate that for each of the various materials tested, the damping characteristics are related to angular speed, and, in general, the measured damping decreases with increasing angular speed. As is noted earlier and discussed in Figure 27, there is evidence of the beam undergoing spin-stiffening effects, which may explain the reduced damping characteristics of the material as the angular speed is increased and the beam's specific stiffness increases. The trends displayed by the data in Figure 28 suggest that the damping characteristics of the composite beam without CNT decreases more rapidly with increasing $\Omega$ than the composite

beam with two weight percent SWCNTs, which is evident from a comparison of the slopes of the linear variations in Figure 28a and Figure 28b for the composites with $v_f$ values of 0.46 and 0.58, respectively. In turn, this indicates that the addition of CNTs to the matrix of fiber-reinforced composites may result in mitigating the adverse effects of spin-stiffening which reduces the damping characteristics of rotating composite beams at high angular speeds. It is also evident from the results that the overall damping in the composite for each $v_f$ value can be improved by an average of over 150 percent with the addition of two weight percent SWCNTs to the composite.

Figure 29 presents a summary of the damping values measured in the first three transverse modes of vibration for the composite beams with zero and two weight percent CNTs at angular
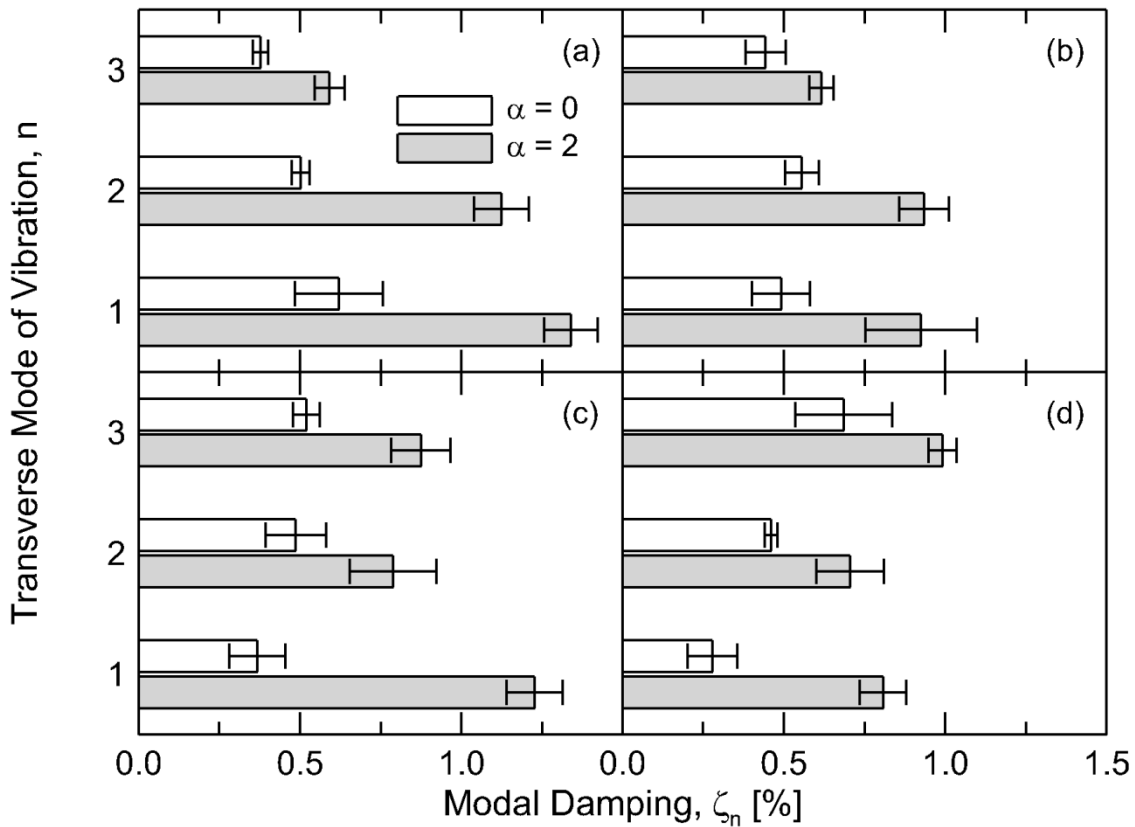


Figure 29: The measured damping in the first three transverse modes of vibration for the composite beams with $\alpha = 0\%$ and $\alpha = 2\%$ SWCNTs for (a) $v_f = 0.46$ and $\Omega = 0$ $RPM$, (b) $v_f = 0.58$ and $\Omega = 0$ $RPM$, (c) $v_f = 0.46$ and $\Omega = 500$ $RPM$, and (d) $v_f = 0.58$ and $\Omega = 500$ $RPM$.

speeds of 0 and 500 *RPM*. Figure 29a and Figure 29b present the results for $\Omega = 0$ *RPM* for $v_f = 0.46$ and 0.58, respectively, and the results for $\Omega = 500$ *RPM* are shown in Figure 29c and Figure 29d for $v_f = 0.46$ and 0.58, respectively. The standard deviation of each damping value is also presented as the error tails on each bar graph, and the white-shaded bars represent the composite beam without CNT ($\alpha = 0$) while the composite beam with two weight percent SWCNTs ($\alpha = 2$) is represented by the bars shaded in grey. By comparing Figure 29a and Figure 29b—or similarly Figure 29c and Figure 29d—the effect of varying the fiber volume fraction on the damping values can be seen for constant angular speed values. To explore the effect of varying the angular speed on the damping values for constant $v_f$ values, a comparison can be made between the results in Figure 29a and Figure 29c—or similarly Figure 29b and Figure 29d.

In general, the results in Figure 29 demonstrate that the damping values measured in the first three transverse modes of vibration for the composite with $\alpha = 2$ are all significantly greater than the damping measured in the composite beam with $\alpha = 0$. In each case it is also evident that the damping either decreases or stays approximately constant in the first two modes of vibration as the fiber volume fraction increases from 0.46 to 0.58, but the damping in the third mode increases slightly as $v_f$ increases from 0.46 to 0.58 (comparing Figure 29a with Figure 29b, or Figure 29c with Figure 29d). Additionally, for a constant fiber volume fraction, the damping in the first two modes either decreases or stays the same with increasing angular speed, whereas the damping actually increases with increasing angular speed in the third mode. Lastly, the difference in the damping values between the cases with $\alpha = 0$ and $\alpha = 2$ for both fiber volume fraction composites are especially pronounced in the case of $\Omega = 500$ *RPM* (Figure 29c and Figure 29d) in the first and third modes of vibration, whereas the differences between the damping values for these same cases in the second mode of vibration are not as significant. These results indicate that

CNT damping may be even more effective at high angular speeds in the first and third transverse modes of vibration, but, in general, that CNTs are effective at increasing the damping in each of the first three transverse modes of vibration for rotating fiber-reinforced composite beams.

The results presented in this chapter have experimentally investigated the effects of ultrasonic dispersion on the damping in high fiber volume fraction composites with CNT reinforcement as well as the damping augmentation provided to stationary and rotating composite beams from matrix-embedded CNTs. An analytical model is developed in Chapter 5 to describe this CNT damping effect on the dynamic response of a rotating composite beam.


## 4.5  Nomenclature used in Chapter 4

$D$    diameter of CNT [$nm$]

$L$    length of CNT [$\mu m$]

$t_p$    ultrasonic processing time [$min$]

$v_f$    fiber volume fraction


*Greek symbols*

$\alpha$    weight percent CNT loading [$\%$]

$\delta$    material damping loss factor

$\varepsilon$    strain [$\%$]

$\zeta_n$    modal damping coefficient [$\%$]

$\omega_n$    natural frequency [$Hz$]

$\Omega$    angular speed [$RPM$]

**Chapter 5: Analysis of Vibration Damping in a Rotating Composite Beam with CNTs**

This chapter presents a numerical model describing the vibration damping effects of carbon nanotubes (CNTs) embedded in the matrix of fiber-reinforced composite materials used in rotating structures. A parametric study is performed to examine the effects of various beam geometries, angular speed profiles, and CNT damping values on the vibration settling times of the numerical simulation cases, and the results are illustrated in a dimensionless design space to demonstrate the use of CNTs for improving the vibration damping characteristics of a rotating composite beam.

**5.1 Modeling of Simple Rotating Beam**

This section presents the geometric configuration along with the numerical model used to simulate the rotation and deformation of the composite beam. Figure 30a presents the rotating hub of radius $R$ to which the three-dimensional beam of length, $L$, thickness, $a$, and width, $b$, is connected, with the origin of the Cartesian coordinate system located at the center of the beam's base. The beam rotates around the vertical central axis of the hub at a time-varying angular speed $\Omega(t)$, and the Cartesian coordinate vectors rotate with the hub at the same speed. The motion of the rotating beam is described in a non-dimensional form using the dimensionless parameters:

$$\alpha = \left(\frac{AL^2}{I}\right)^{1/2} \qquad \bar{\Omega} = \Omega\left(\frac{\rho AL^4}{EI}\right)^{1/2} \qquad \bar{t} = t\left(\frac{\rho AL^4}{EI}\right)^{-1/2} \qquad \{\bar{c}, \bar{R}, \bar{u}, \bar{v}, \bar{x}, \bar{y}, \bar{s}\} = \{c, R, u, v, x, y, s\}/L$$

where $\alpha$, $A$, $L$, $I$, $\rho$, and $E$ are the slenderness ratio, cross-sectional area, length, moment of inertia defined as $a^3b/12$, density, and modulus of the beam, respectively. The angular speed profile specified at the base of the beam is shown in Figure 30b and is expressed using the dimensionless angular speed, $\bar{\Omega}$, and the dimensionless time, $\bar{t}$. The dimensionless angular speed profile consists of a ramp period where the speed is increased steadily from zero and a hold period where the speed

89
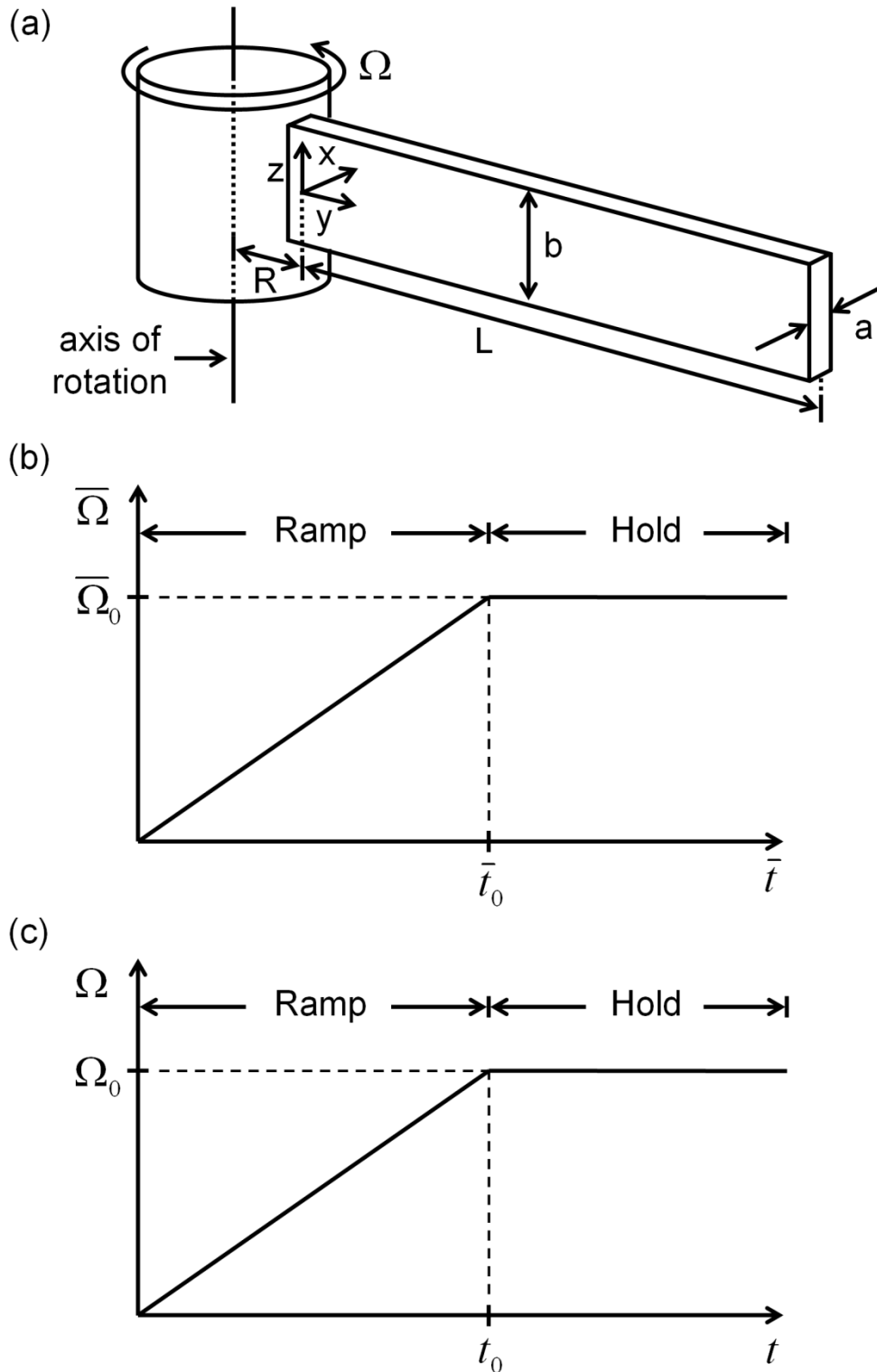
Figure 30: (a) Schematic of the hub and beam geometry with hub radius, $R$, beam length, $L$, thickness, $a$, and width, $b$, and a description of the (b) dimensionless and (c) dimensional angular speed profile, governed by the dimensionless and dimensional steady-state angular speed, $\bar{\Omega}_0$ and $\Omega_0$, and the dimensionless and dimensional ramp time, $\bar{t}_0$ and $t_0$, respectively.

is held constant, where this profile is described by the dimensionless steady-state speed, $\bar{\Omega}_0$, and the dimensionless ramp time, $\bar{t}_0$, as specified in Figure 30b.

Further, $\bar{c}$ is the dimensionless coulomb damping parameter, $\bar{R}$ is the dimensionless radius of the hub, $\bar{u}$ and $\bar{v}$ are the dimensionless transverse and axial beam deformations, respectively, $\bar{x}$ and $\bar{y}$ represent the dimensionless distance along the x- and y-axis, respectively, and $\bar{s}$ denotes the dimensionless stretch deformation of the beam. The dimensionless stretch variable, $\bar{s}$, provides a more succinct mathematical approach compared to using the axial deformation variable, $\bar{v}$, when formulating the governing equations of the rotating beam as the beam undergoes large deformations during vibration, and can be written by neglecting higher order terms according to [113] as:

$$\bar{s} = \bar{v} + \frac{1}{2} \int_0^{\bar{y}} \left(\frac{\partial \bar{u}}{\partial \bar{y}}\right)^2 d\bar{y} \tag{27}$$

The material properties of the composite beam are considered to be isotropic and homogeneous described by the law of mixtures [114], where the effects of heterogeneous and orthotropic composite properties will be addressed in future studies. Therefore, the linearized governing equations of motion assuming a one-dimensional representation of the constant cross-sectional beam may be derived using an energy approach, written as:

$$\bar{U} = \frac{1}{2} \int_0^1 \left[ \alpha^2 \left(\frac{\partial \bar{s}}{\partial \bar{y}}\right)^2 + \left(\frac{\partial^2 \bar{u}}{\partial \bar{y}^2}\right)^2 \right] d\bar{y} \tag{28}$$

$$\bar{T} = \frac{1}{2} \int_0^1 \left[ \left(\frac{\partial \bar{s}}{\partial \bar{t}} - \bar{\Omega}\bar{u}\right)^2 + \left(\frac{\partial \bar{u}}{\partial \bar{t}} + \bar{\Omega}\{\bar{R} + \bar{y} + \bar{s}\}\right)^2 \right] d\bar{y} \tag{29}$$

where $\bar{U}$ and $\bar{T}$ are the dimensionless strain and kinetic energies of the beam, respectively. The damping in the CNT-reinforced composite beam may be modeled with a coulomb and viscous damping parameter to represent the energy dissipation effects of the CNTs embedded in the

composite matrix and the damping in the composite without CNTs, respectively, as demonstrated in [78]. These damping models are applied to the physics of the rotating beam via dimensionless body forces derived using a first-mode assumption [99,100], written for coulomb and viscous damping, respectively, in dimensionless form as:

$$\bar{F}_c = \bar{c}\beta^4|\bar{u}|sgn\left(\frac{\partial\bar{u}}{\partial\bar{t}}\right) \tag{30}$$

$$\bar{F}_v = 2\zeta\beta^2\frac{\partial\bar{u}}{\partial\bar{t}} \tag{31}$$

where the subscripts $c$ and $v$ represent coulomb and viscous damping, respectively, $\beta$ is the dimensionless constant arising from the first-mode eigenvalue calculation of a transversely vibrating beam, $sgn()$ is the signum function which returns the sign of its argument, and $\zeta$ is the viscous damping parameter. The effect of rotation on the beam dynamics is modeled by an additional dimensionless body force, expressed as:

$$\bar{F}_r = \bar{\Omega}^2(\bar{R} + \bar{y})\hat{s} - \frac{\partial\bar{\Omega}}{\partial\bar{t}}(\bar{R} + \bar{y})\hat{u} \tag{32}$$

where the subscript $r$ denotes rotation and $\hat{s}$ and $\hat{u}$ are unit vectors in the stretch and transverse directions, respectively.

The complete governing equations of motion for the rotating beam can be obtained by applying Hamilton's principle to Equation 28 and Equation 29, and considering the body forces in Equation 30–Equation 32, which may be combined and written as:

$$\frac{\partial^2\bar{s}}{\partial\bar{t}^2} - \alpha^2\frac{\partial^2\bar{s}}{\partial\bar{y}^2} - \bar{\Omega}^2\bar{s} - 2\bar{\Omega}\frac{\partial\bar{u}}{\partial\bar{t}} - \frac{\partial\bar{\Omega}}{\partial\bar{t}}\bar{u} - \bar{\Omega}^2(\bar{R} + \bar{y}) = 0 \tag{33}$$

$$\frac{\partial^2\bar{u}}{\partial\bar{t}^2} + 2\zeta\beta^2\frac{\partial\bar{u}}{\partial\bar{t}} + \frac{\partial^4\bar{u}}{\partial\bar{y}^4} - \bar{\Omega}^2\left(\bar{u} - \frac{\partial}{\partial\bar{y}}\left\{\left[\bar{R}(1 - \bar{y}) + \frac{1}{2}(1 - \bar{y}^2)\right]\frac{\partial\bar{u}}{\partial\bar{y}}\right\}\right) - 2\bar{\Omega}\frac{\partial\bar{s}}{\partial\bar{t}} - \frac{\partial\bar{\Omega}}{\partial\bar{t}}\bar{s}$$

$$+\bar{c}\beta^4\left|\frac{\bar{u}}{\bar{u}_{\bar{x}=1}}\right|sgn\left(\frac{\partial\bar{u}}{\partial\bar{t}}\right) + \frac{\partial\bar{\Omega}}{\partial\bar{t}}(\bar{R} + \bar{y}) = 0 \tag{34}$$

Several terms arise in Equation 33 and Equation 34 as a result of modeling the beam in a rotating frame of reference: the term $\bar{\Omega}^2 \left( \bar{u} - \frac{\partial}{\partial \bar{y}} \left\{ \left[ \bar{R}(1 - \bar{y}) + \frac{1}{2}(1 - \bar{y}^2) \right] \frac{\partial \bar{u}}{\partial \bar{y}} \right\} \right)$ in Equation 34 describes the motion-induced stiffness, or equivalently the *spin-stiffening* effect on the beam [107], and the *gyroscopic* effects of rotation [115] are expressed by the terms $2\bar{\Omega}\frac{\partial \bar{u}}{\partial \bar{t}}$ and $\frac{\partial \bar{\Omega}}{\partial \bar{t}}\bar{u}$ of Equation 33 as well as the $2\bar{\Omega}\frac{\partial \bar{s}}{\partial \bar{t}}$ and $\frac{\partial \bar{\Omega}}{\partial \bar{t}}\bar{s}$ terms of Equation 34. In addition, it is evident that Equation 33 and Equation 34 are coupled through the gyroscopic terms identified above and, therefore, must be solved simultaneously.

Assuming the beam to be initially at rest and cantilevered to the rotating hub at one end with the opposite end able to freely deform, the three initial conditions and six boundary conditions necessary for solving Equation 33 and Equation 34 may be written in dimensionless form as

$$\bar{s} = \bar{u} = \frac{\partial \bar{u}}{\partial \bar{t}} = 0 \quad at \ \bar{t} = 0 \tag{35}$$

$$\bar{s} = \bar{u} = \frac{\partial \bar{u}}{\partial \bar{y}} = 0 \quad at \ \bar{y} = 0 \tag{36}$$

$$\frac{\partial \bar{s}}{\partial \bar{y}} = \frac{\partial^2 \bar{u}}{\partial \bar{y}^2} = \frac{\partial^3 \bar{u}}{\partial \bar{y}^3} = 0 \quad at \ \bar{y} = 1 \tag{37}$$

Equation 33–Equation 37 completely describe the dynamic response of a rotating cantilever beam including the CNT energy dissipation effects. These equations of motion are solved using the finite element method [116–118] and marched in time using the generalized-$\alpha$ scheme [119] to obtain the dynamic response of the beam, where a detailed derivation of this approach is presented in [87]. The results and analysis of the numerically simulated dimensionless transverse displacement at the beam's free end, or equivalently the *tip displacement*, $\bar{u}_{\bar{x}=1}$, with respect to the rotating coordinate system fixed at the base of the beam are presented below. The current simulations are compared with results from published reports as presented in Chapter 5.2. With

the validated model as basis, a parametric study is performed to explore the effects of CNT

damping, geometric variation, and different angular speed profiles on the dynamic response of

the rotating composite beam, and the results of the parametric study are described in Chapter 5.3.


## 5.2 Validation of Model

The numerical model developed above is first validated against results of the undamped

response of a rotating beam (i.e. $\zeta = 0$ and $\bar{c} = 0$) presented in [87] and [120]. The comparison

is shown in Figure 31a and Figure 31b, respectively, where the results from the literature are

indicated by the solid lines and the numerical simulations are denoted by the dashed lines and

open circle markers. In Figure 31a, the beam geometry is described by $\alpha = 70$ and $\bar{R} = 0.1$ with
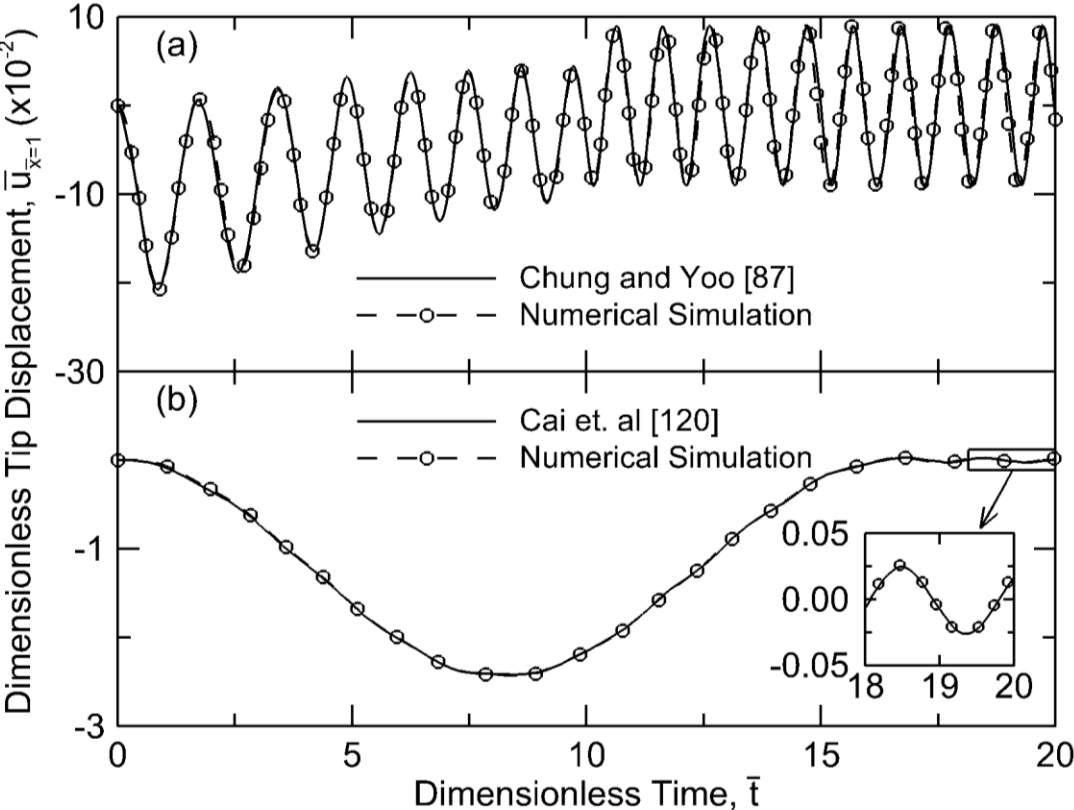


Figure 31: Validation of the dynamic beam response predicted using the numerical model with results presented by (a) Chung and Yoo [87] and (b) Cai, et al. [120].

94

a dimensionless angular speed profile defined by $\bar{\Omega}_0 = 10$ and $\bar{t}_0 = 10$, where it is evident that the current simulation and the results from the literature shown in Figure 31a exhibit good agreement with one another. The effect of *spin-stiffening* [107] is apparent in these trends as the frequencies of the dynamic responses increase during the ramp period ($0 < \bar{t} < 10$), a result of the centripetal forces caused by rotation acting on the beams in the axial direction towards the center of rotation. Additionally, due to the transverse forces acting on the beam during the angular acceleration of the ramp period, the vibrations oscillate around a deformed axis, which is dependent on time. During the hold period in Figure 31a ($10 < \bar{t} < 20$) when the angular speed is steady, the natural frequency of the beam is constant and the vibrations oscillate around zero as a result of the transverse acceleration forces reducing to zero. In general, the trends observed in Figure 31a, related to the angular speed and consequent spin-stiffening effect, are seen in the numerical simulation results throughout the remainder of this study.

Figure 31b compares the current simulation to the results reported in [120] for $\alpha = 2500$ and $\bar{R} = 0$ with a ramp period defined by $\bar{\Omega}(t) = 1.12(1 - \cos(0.188 \cdot \bar{t}))$ for $\bar{t} < 16.7$ and a hold period with $\bar{\Omega} = 2.25$ for $\bar{t} > 16.7$. The simulation results in Figure 31b are shown for a dimensionless time range of 0 to 20, where the trends demonstrate that the beam's vibrations are small in magnitude as a result of the smooth speed profile. A portion of the simulated response from $\bar{t} = 18$ to 20 is enlarged in the inset of Figure 31b to better illustrate the vibration magnitude of the response as well as to demonstrate the good agreement between the results of [120] and the numerical simulation. The small differences between the results may be attributed to the difference in convergence requirements used to determine the discretization scales involved in each of the different cases. Overall, the trends presented in Figure 31 show that the current model predicts values consistent with analytical data in the literature.
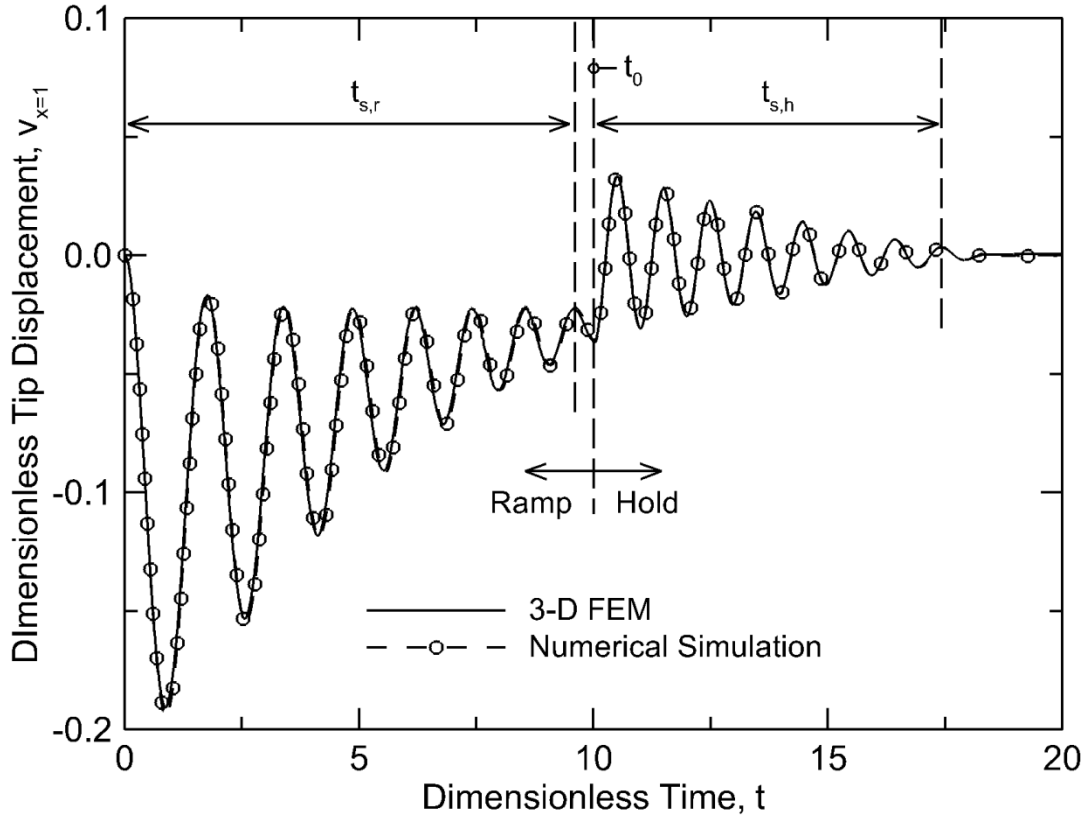
Figure 32: Comparison of the numerical simulation using the presented model with a three-dimensional FEM solution for $\zeta = 2.5 \times 10^{-2}$ and $\bar{c} = 2.5 \times 10^{-3}$, where the dimensionless vibration settling times for the ramp, $\bar{t}_{s,r}$, and hold, $\bar{t}_{s,h}$, periods are also indicated.

A comparison between the numerical model developed in Chapter 5.1 and a three-dimensional finite element model (FEM) is presented in Figure 32 for a rotating beam defined by $\alpha = 300$ and $\bar{R} = 0.1$. The rotating three-dimensional beam is modeled using the commercial software, COMSOL$^\copyright$, with a speed profile described by $\bar{\Omega}_0 = 10$ and $\bar{t}_0 = 10$ and a viscous and coulomb damping parameter of $2.5 \times 10^{-2}$ and $2.5 \times 10^{-3}$, respectively. The trends in Figure 32 show good agreement between the two models throughout the range of the simulation.

The dimensionless settling times, $\bar{t}_s$, to reach 95% of the initial tip displacement during the ramp (denoted as $\bar{t}_{s,r}$) and hold (denoted as $\bar{t}_{s,h}$) periods are also indicated in Figure 32. The $\bar{t}_{s,r}$ value is determined by fitting a decay envelop to the vibration peaks during the ramp period

96

compared to the deformed neutral axis of vibration over time, and applying these curves to determine the elapsed dimensionless time before the vibration amplitude decreases to five percent of its maximum value. The vibration settling time during the hold period is computed in a similar manner by fitting a decay envelope to the oscillating beam response for $\bar{t} > \bar{t}_0$ to determine the elapsed dimensionless time from $\bar{t} = \bar{t}_0$ when the vibrations settle to five percent of the maximum vibration observed at the start of the hold period. These two settling times are used throughout the remainder of the study to quantify the vibrations in each simulation case.

In general, the trends in Figure 32 demonstrate that the numerical model developed in Chapter 5.1 predicts similar results to the three-dimensional FEM model of the identical rotating system, further supporting the validity of the numerical simulations used in the ensuing parametric study. Together with the comparison in Figure 31, the validated numerical simulations form the basis of the results reported throughout the remainder of the study.

## 5.3 Parametric Study

A parametric study is conducted to explore the individual effects of the beam geometry (i.e. $\alpha$ and $\bar{R}$), the angular speed profile (i.e. $\bar{\Omega}_0$ and $t_0$), and the damping effects (i.e. $\zeta$ and $\bar{c}$) on the numerically simulated response of the composite beam. The results of the study are presented in

Table 4: Values of the variables in Equations 32 and 33 used in the parametric study

| Variable | Value | | |
|---|---|---|---|
| | *low* | *mid* | *high* |
| slenderness ratio, $\alpha$ | 100 | 300 | 500 |
| dimensionless hub radius, $\bar{R}$ | 0.05 | 0.10 | 0.20 |
| dimensionless steady-state speed, $\bar{\Omega}_0$ | 10 | 30 | 50 |
| dimensionless ramp time, $\bar{t}_0$ | 10 | 20 | 30 |
| viscous damping, $\zeta$ | 0 | $2.5 \times 10^{-2}$ | $5.0 \times 10^{-2}$ |
| dimensionless coulomb damping, $\bar{c}$ | 0 | $2.5 \times 10^{-3}$ | $5.0 \times 10^{-3}$ |

Figure 33–Figure 36. The range of values explored for each parameter are presented in Table 4 and are approximated from published reports detailing the measurement of damping in CNT-reinforced composite beams and the geometry of various rotor vibration studies [61,76,78–83,86,87]. The individual effects of varying $\alpha$, $\bar{R}$, $\bar{\Omega}_0$, and $\bar{t}_0$ are studied in Figure 33–Figure 36, respectively, while the remaining variables are held constant at the *mid* values indicated in Table 4 in each case. The dimensionless tip displacement, $\bar{u}_{\bar{x}=1}$, is shown in subfigure (a) of each figure, and contour plots of the dimensionless settling times for the ramp and hold periods are
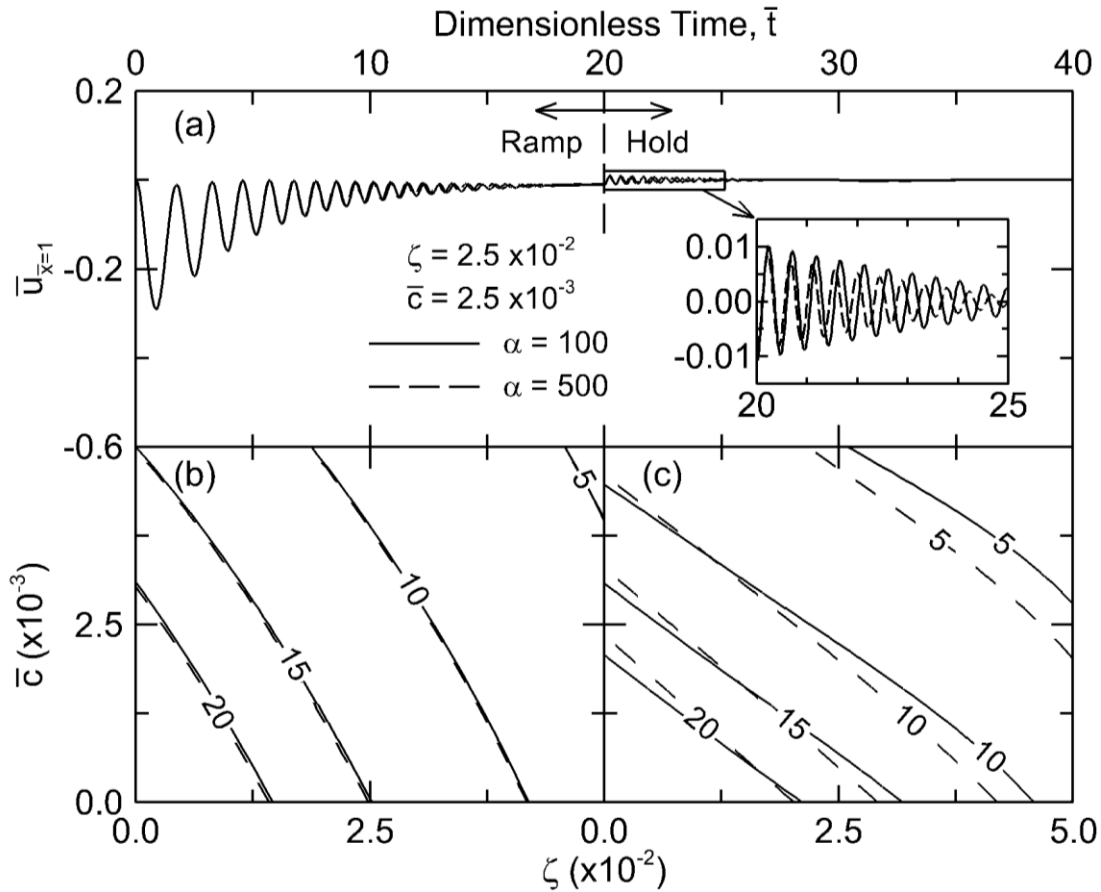


Figure 33: (a) Effect of varying the slenderness ratio, $\alpha$, on the dimensionless tip displacement of the beam, $\bar{u}_{\bar{x}=1}$, for $\zeta = 2.5 \times 10^{-2}$ and $\bar{c} = 2.5 \times 10^{-3}$, where the inset figure presents a larger view of the simulation results from $\bar{t} = 20$ to $25$. Contour plots of the dimensionless vibration settling times during the (b) ramp ($\bar{t}_{s,r}$) and (c) hold ($\bar{t}_{s,h}$) periods are presented for the two slenderness ratios on the $\bar{c} - \zeta$ damping parameter plane.

presented in subfigures (b) and (c), respectively, to explore the viscous and CNT damping effects on the vibration response of the rotating beam.

Figure 33 illustrates the parametric variation of the slenderness ratio, $\alpha$, where the dynamic responses of $\bar{u}_{\bar{x}=1}$ for $\alpha = 100$ and $500$ are shown in Figure 33a for damping values of $\zeta = 2.5 \times 10^{-2}$ and $\bar{c} = 2.5 \times 10^{-3}$. The responses of the two cases with varying $\alpha$ are almost indistinguishable from one another during the ramp period ($\bar{t} < 10$); however, the difference in the frequency and decay of each case during the hold period ($\bar{t} > 10$) is significant, shown by the closer view in the inset of Figure 33a for $\bar{t} = 20$ to $25$. From the trends in this inset, it is evident that the beam with $\alpha = 500$ vibrates with a greater frequency than the case with $\alpha = 100$—reflecting the increase in the natural frequency of the beam with increasing slenderness ratio. For a rectangular beam with a uniform cross-section, as in this study, the increase in $\alpha$ indicates a decrease in the beam thickness, $a$, for a constant beam length, and, consequently, less beam inertia against which the damping force is applied at higher $\alpha$ values. This results in a greater vibration damping effect with increasing $\alpha$, as reflected in the lower settling times and tip displacements for $\alpha = 500$ compared to $\alpha = 100$ illustrated in Figure 33a.

Contour plots of the settling times for different $\alpha$ values during the ramp ($\bar{t}_{s,r}$) and hold ($\bar{t}_{s,h}$) periods are presented in Figure 33b and Figure 33c, respectively, as a function of the two damping parameters, $\zeta$ and $\bar{c}$. It is evident that the settling times decrease as either damping parameter is increased. Figure 33b and Figure 33c reveal a non-monotonic trend in $\bar{t}_{s,r}$ and $\bar{t}_{s,h}$ with respect to damping, where the settling times decrease rapidly as the damping parameters are increased from zero and then level off at the higher damping values. The results also demonstrate that the slenderness ratio, $\alpha$, has an almost negligible effect on the beam's response and associated settling time during the ramp period (Figure 33b). However, it is apparent during the

hold period (Figure 33c) that, at high damping levels, as $\alpha$ is increased, the required damping decreases (either viscous or coulomb) to achieve the same $\bar{t}_s$ value. During the hold period for $\zeta \gtrsim 1.5 \times 10^{-2}$, similar damping parameters result in lower settling times for higher values of $\alpha$, indicating that the damping in this region is more effective at reducing the settling times as the beam becomes more slender. For situations with less viscous damping ($\zeta \lesssim 1.5 \times 10^{-2}$), the aforementioned trends during the hold period are reversed and an increase in $\alpha$ is seen to result in slightly higher settling times at similar damping value.
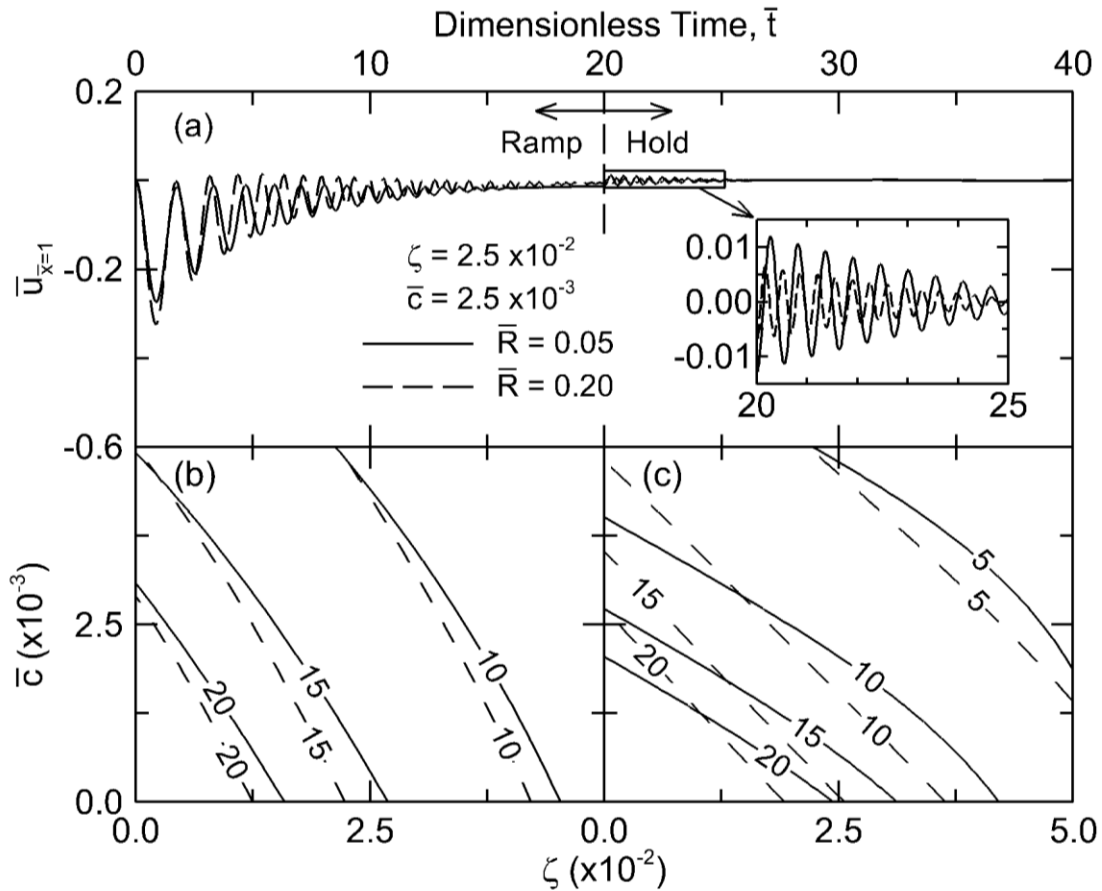


Figure 34: (a) Effect of varying the dimensionless hub radius, $\bar{R}$, on the dimensionless tip displacement of the beam, $\bar{u}_{\bar{x}=1}$, for $\zeta = 2.5 \times 10^{-2}$ and $\bar{c} = 2.5 \times 10^{-3}$, where the inset figure presents a larger view of the simulation results from $\bar{t} = 20$ to $25$. Contour plots of the dimensionless vibration settling times during the (b) ramp ($\bar{t}_{s,r}$) and (c) hold ($\bar{t}_{s,h}$) periods are presented for the two dimensionless hub radii on the $\bar{c} - \zeta$ damping parameter plane.

100

The results of the parametric variation of $\bar{R}$ with damping values of $\zeta = 2.5 \times 10^{-2}$ and $\bar{c} = 2.5 \times 10^{-3}$ are shown in Figure 34, and it is evident from the trends in Figure 34a that the simulated response during the ramp period when $\bar{R} = 0.05$ settles slightly faster and has a smaller amplitude of vibration than the case with $\bar{R} = 0.20$. For a constant beam length, an increase in $\bar{R}$ results in a greater rotational body force acting on the beam. This, in turn, results in a larger initial deflection of the beam's free end, causing higher magnitude vibrations during the ramp period, as exemplified for $\bar{R} = 0.20$ in Figure 34a. The response for $\bar{R} = 0.05$ settles to a deformed amplitude with negligible vibration by $\bar{t} = 10$, resulting in a large initial beam deflection at the start of the hold period that is significantly greater than the case with $\bar{R} = 0.20$. However, the vibrations in both cases, $\bar{R} = 0.05$ and $\bar{R} = 0.20$, settle towards zero at approximately the same rate (shown by the inset in Figure 34a). In addition, the frequency of vibration when $\bar{R} = 0.20$ is much greater than the case with $\bar{R} = 0.05$, demonstrating an effect of greater spin-stiffening forces on the beam at higher $\bar{R}$. In general, the trends in Figure 34a demonstrate that an increase in $\bar{R}$ results in higher initial displacements and lower settling times during the ramp period, and lower vibration magnitudes and settling times are observed for increasing $\bar{R}$ during the hold period due to the spin-stiffening effects on the beam.

Figure 34b and Figure 34c present the contours of $\bar{t}_{s,r}$ and $\bar{t}_{s,h}$ during the ramp and hold periods, respectively, in terms of the two damping parameters, $\zeta$ and $\bar{c}$, for a parameter variation of $\bar{R}$. The overall trends are similar to those exhibited in Figure 33b and Figure 33c, where the settling times decrease at higher damping values and there is a non-linear trend in $\bar{t}_{s,r}$ and $\bar{t}_{s,h}$ with respect to the damping parameters. The contours in Figure 34b show greater distinction than those in Figure 33b, indicating that the parameter variation of the dimensionless hub radius has a greater effect during the ramp period than the variation of the slenderness ratio.

Additionally, for a given value of the settling time, the contours for the two values of $\bar{R}$ are seen in Figure 34b and Figure 34c to intersect at different locations throughout the damping parameter space, signifying that each damping parameter combination will have varying effectiveness at different values of $\bar{R}$. During the hold period (Figure 34c), the results illustrate lower settling times with increasing $\bar{R}$ for $\zeta \gtrsim 1.75 \times 10^{-2}$, and higher settling times with increasing $\bar{R}$ for smaller values of viscous damping, $\zeta$. In addition, contours of the same values of $\bar{t}_{s,h}$ are further apart at higher values of both damping parameters, $\zeta$ and $\bar{c}$ (Figure 34c), demonstrating that the effect of varying $\bar{R}$ is more significant as either material damping value is increased.
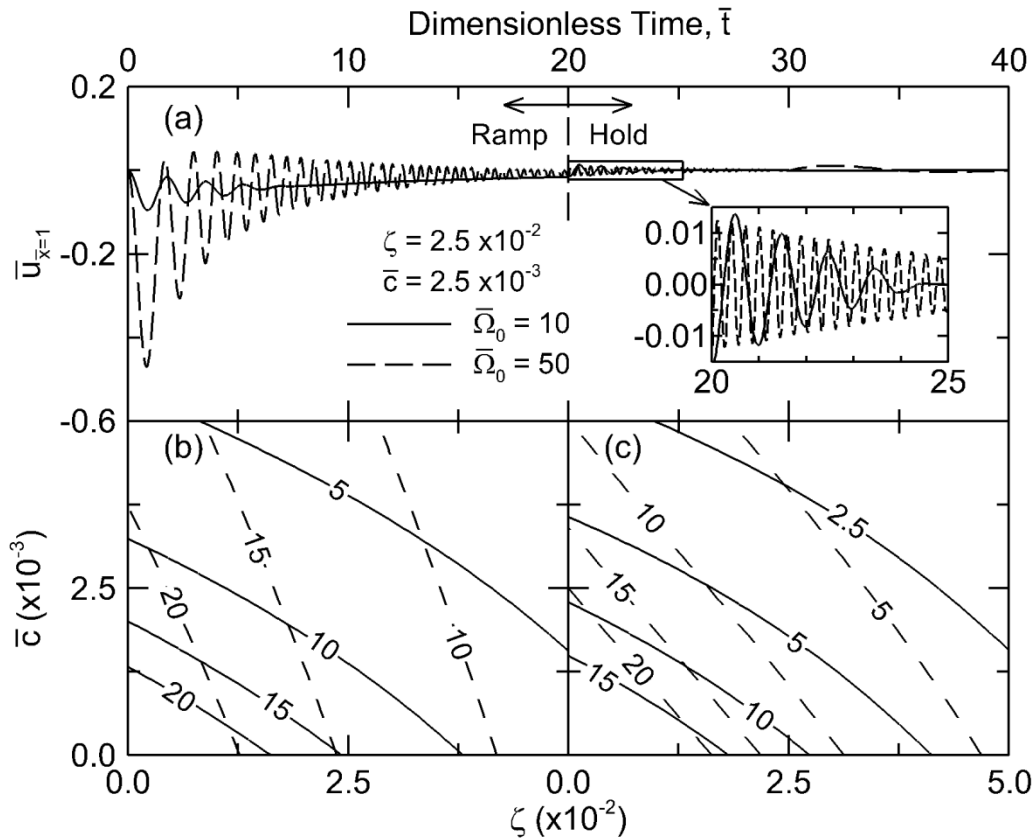


Figure 35: (a) Effect of varying the dimensionless steady-state angular speed, $\bar{\Omega}_0$, on the dimensionless tip displacement of the beam, $\bar{u}_{\bar{x}=1}$, for $\zeta = 2.5 \times 10^{-2}$ and $\bar{c} = 2.5 \times 10^{-3}$, where the inset figure presents a larger view of the simulation results from $\bar{t} = 20$ to $25$. Contour plots of the dimensionless vibration settling times during the (b) ramp ($\bar{t}_{s,r}$) and (c) hold ($\bar{t}_{s,h}$) periods are presented for the two dimensionless angular speeds on the $\bar{c} - \zeta$ damping parameter plane.

The effects of the angular speed profile parameterized in terms of $\bar{\Omega}_0$ and $\bar{t}_0$ on the dimensionless tip displacement of the beam are illustrated in Figure 35 and Figure 36. Figure 35a shows that for $\bar{\Omega}_0 = 50$, the rapid increase in angular speed during the ramp period results in a significantly larger vibration magnitude and settling time than the case of $\bar{\Omega}_0 = 10$. In addition, the frequency of vibrations in the response during the ramp period is seen to increase considerably for $\bar{\Omega}_0 = 50$ compared to $\bar{\Omega}_0 = 10$, clearly demonstrating the increased effect of spin-stiffening at higher $\bar{\Omega}_0$ values. In the inset of Figure 35a, it is evident that the initial tip displacements at the beginning of the hold period for both cases are approximately equal;
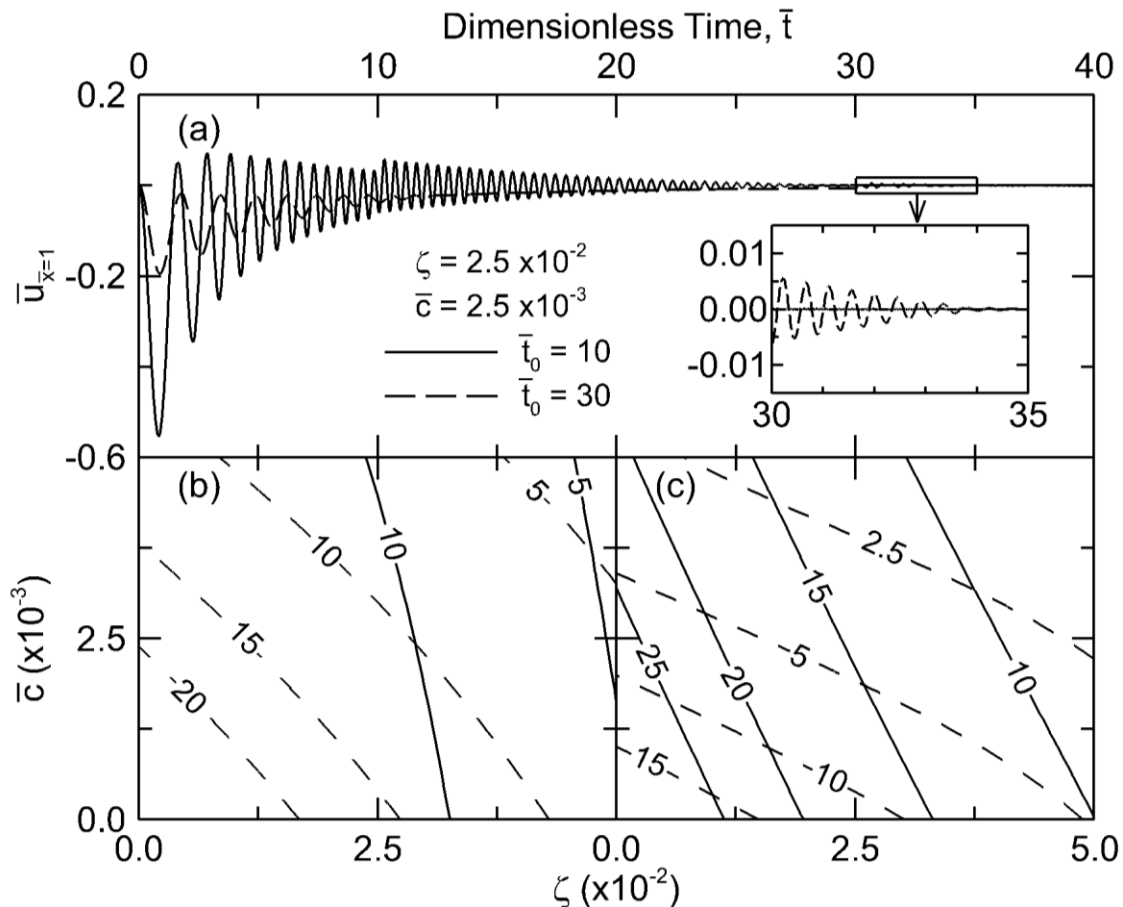


Figure 36: (a) Effect of varying the dimensionless ramp time, $\bar{t}_0$, on the dimensionless tip displacement of the beam, $\bar{u}_{\bar{x}=1}$, for $\zeta = 2.5 \times 10^{-2}$ and $\bar{c} = 2.5 \times 10^{-3}$, where the inset figure presents a larger view of the simulation results from $\bar{t} = 30$ to $35$. Contour plots of the dimensionless vibration settling times during the (b) ramp ($\bar{t}_{s,r}$) and (c) hold ($\bar{t}_{s,h}$) periods are presented for the two dimensionless ramp times on the $\bar{c} - \zeta$ damping parameter plane.

103

however, the vibrations are quickly reduced to almost zero in the case of $\bar{\Omega}_0 = 10$, whereas the vibrations settle much slower in the case of $\bar{\Omega}_0 = 50$, resulting in an increase in the dimensionless settling time at the larger dimensionless angular velocities.

Figure 36a shows the dynamic response of the beam for the parametric variation of $\bar{t}_0$. In general, the trends in Figure 36a are similar to those in Figure 35a, except that the effects of increasing $\bar{t}_0$ are similar to those of decreasing $\bar{\Omega}_0$. It is evident that the magnitude of the response throughout the majority of the simulation is greater for $\bar{t}_0 = 10$ compared to $\bar{t}_0 = 30$. In addition, the trends in Figure 36a show that the frequency of the response increases more rapidly throughout the ramp period with decreasing $\bar{t}_0$ due to the effect of spin-stiffening. The similarity of the trends in Figure 35a and Figure 36a is a result of the relationship of $\bar{\Omega}_0$ and $\bar{t}_0$ to the slope of the angular speed profile, or equivalently the angular acceleration of the beam during the ramp period. From inspection of Figure 30b, it is evident that the slope of the speed profile is directly proportional to $\bar{\Omega}_0$ and inversely proportional to $\bar{t}_0$, indicating that when $\bar{\Omega}_0$ is increased or $\bar{t}_0$ is decreased the slope of the speed profile becomes steeper. In turn, as the slope of the angular speed profile—or, equivalently, the angular acceleration—increases, the vibration magnitudes and settling times will increase because of the greater transverse forces acting on the beam, as exemplified by the simulation trends shown in Figure 35a and Figure 36a. Therefore, the rotating composite beam will generally experience lower magnitude vibrations and decreased settling times at low values of $\bar{\Omega}_0$ and high $\bar{t}_0$ parameters.

The contour plots in Figure 35b–c and Figure 36b–c demonstrate the effect of damping on the response of the rotating beam for different dimensionless angular speed profiles. At the lower value of $\bar{\Omega}_0 = 10$ in Figure 35b–c, or the higher value of $\bar{t}_0 = 30$ in Figure 36b–c, the contour lines are less steep on the $\bar{c} - \zeta$ plane indicating that, in general, an increase in $\bar{c}$—equivalently an

increase in the energy dissipation due to the presence of CNTs—will have a greater effect on reducing the vibration of the rotating beam under these conditions. As a result, a slight increase in the coulomb damping has a significant effect on reducing the $\bar{t}_{s,r}$ and $\bar{t}_{s,h}$ values, whereas a much greater increase in the viscous parameter is necessary to achieve a similar reduction in the settling times. In Figure 35b, the spacing between the contour lines increases at the larger value of $\bar{\Omega}_0 = 50$, indicating the need for more damping in order to reduce the settling time during the ramp period, as the steady-state dimensionless angular speed increases. Additionally, the results in Figure 35c demonstrate that lower settling times will occur during the hold period for similar damping values, as the steady-state angular velocity is decreased.

The trends in Figure 36b for the parameter variation of $\bar{t}_0$ are similar to those in Figure 35b and illustrate that the settling time during the ramp period, $\bar{t}_{s,r}$, decreases at the higher $\bar{t}_0$ value of 30 and increases when the ramp time is reduced. During the hold period (Figure 36c), the maximum $\bar{t}_{s,h}$ values for $\bar{t}_0 = 10$ are relatively larger than the maximum settling times of the other design cases presented in Figure 33–Figure 35 for similar damping values as a result of the high transverse acceleration loads applied to the beam during the rapid ramp, which causes larger initial beam displacements and greater vibration magnitudes. In general, the results in Figure 35 and Figure 36 demonstrate that the slope of the angular speed profile and the steady state angular speed have a significant effect on the response of the rotating composite beam, and as $\bar{\Omega}_0$ is increased or $\bar{t}_0$ is decreased, the system requires more damping to achieve similar $\bar{t}_{s,r}$ and $\bar{t}_{s,h}$ values.

The use of the simulations for an actual application is examined by considering the parameters of the helicopter rotor vibration control study in [81]. To this end, Figure 37a and Figure 37b present the contour plots of the $\bar{t}_{s,r}$ and $\bar{t}_{s,h}$ values during the ramp and hold periods, respectively, on a parameter space of coulomb and viscous damping, for a composite beam described by
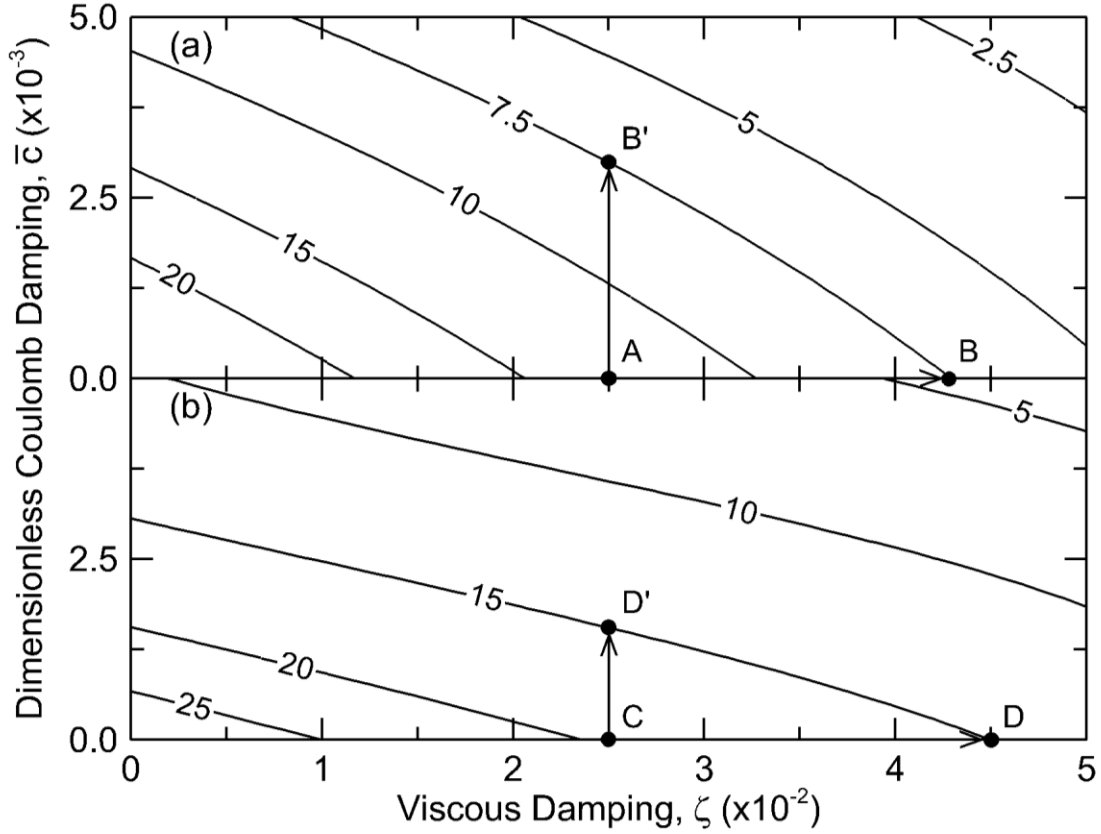
Figure 37: Contours of the dimensionless settling times during (a) ramp ($\bar{t}_{s,r}$) and (b) hold ($\bar{t}_{s,h}$) periods on the on the $\bar{c} - \zeta$ damping parameter plane for the conditions mimicking the helicopter rotor vibration control study in [81]: $\alpha = 300$, $\bar{R} = 0.10$, $\bar{\Omega}_0 = 30$, and $\bar{t}_0 = 20$.

$\alpha = 300$ and $\bar{R} = 0.1$ with a speed profile defined by $\bar{\Omega}_0 = 30$ and $\bar{t}_0 = 20$ that closely match the parameters in [81]. For a fiber-reinforced composite beam with no CNTs and with a viscous damping of $\zeta = 2.5 \times 10^{-2}$, the dimensionless settling times during the ramp and the hold periods are $\bar{t}_{s,r} \approx 13$ and $\bar{t}_{s,h} \approx 19$, denoted by the Points A and C in Figure 37a and Figure 37b, respectively. The design plots in Figure 37 provide for exploring the options for reducing the dimensionless settling times of the rotating composite beam by increasing either the viscous or coulomb damping parameters of the material. For example, to decrease the settling time during the ramp by approximately 42% from $\bar{t}_{s,r} = 13$ to $\bar{t}_{s,r} = 7.5$ in a composite with no carbon nanotubes ($\bar{c} = 0$), the viscous damping ($\zeta$) would need to be increased by approximately $1.8 \times 10^{-2}$ (Point

106

B in Figure 37a). Alternatively, the same decrease in settling time may be achieved without altering the viscous damping of $\zeta = 2.5 \times 10^{-2}$ by introducing a coulomb damping parameter of $\bar{c} \approx 3 \times 10^{-3}$, (Point B' in Figure 37a) corresponding to the addition of about one weight percent CNTs into the matrix of the composite based on the measurements in [78]. Similar trends are demonstrated for the settling time reduction during the hold period in Figure 37b, where an increase in the viscous damping parameter of $\zeta \approx 2 \times 10^{-2}$ (Point D in Figure 37b) is required to reduce $\bar{t}_{s,h}$ by 21% from 19 to 15 in a composite with no carbon nanotubes ($\bar{c} = 0$), compared to an increase in the coulomb damping value of $\bar{c} = 2 \times 10^{-3}$, while keeping $\zeta = 2.5 \times 10^{-2}$ (Point D' in Figure 37b) to achieve the same damping enhancement. Additionally, the results in Figure 37a and Figure 37b indicate that as the value of $\bar{c}$ is increased to $5 \times 10^{-3}$, or equivalently about two weight percent matrix-embedded CNTs according to the measurements in [78], the settling times will be reduced during the ramp and hold periods by an average of 60% over the baseline beam without CNTs. In general, Figure 37 demonstrates how the numerical simulations and the resulting trends in Figure 33–Figure 36 may be applied to explore the effects of damping augmentation provided to rotating composite beams through the addition of CNTs to the composite matrix.

This chapter presented a numerical model of the effects of CNT-based damping in a rotating fiber-reinforced composite beam using a stick-slip coulomb damping term to describe the frictional behavior at the nanotube-matrix interface as the material is deformed. This model is extended to incorporate the effects of strain-dependent damping and higher complexity rotating composite structures in Chapter 6.

### 5.4  Nomenclature used in Chapter 5

$a$        hub radius [$m$]

$A$        cross-sectional area [$m^2$]

$c$        coulomb damping coefficient [$m$]

$E$        modulus of elasticity [$Pa$]

$F$        force [$N$]

$I$        moment of inertia [$m^4$]

$L$        beam length [$m$]

$s$        stretch deformation [$m$]

$t$        time [$s$]

$T$        kinetic energy [$J$]

$u$        transverse deformation [$m$]

$U$        strain energy [$J$]

$v$        axial deformation [$m$]

$x$        x-direction coordinate [$m$]

$y$        y-direction coordinate [$m$]

$z$        z-direction coordinate [$m$]


**Greek symbols**

$\alpha$        slenderness ratio

$\beta$        eigenvalue of first transverse vibration mode

$\zeta$        viscous damping coefficient

$\rho$        density [$kg/m^3$]

$\Omega$       angular speed [*rad/s*]


**Subscripts/Superscripts**

‾       dimensionless value

^       weighting function

$_0$       constant parameter

**Chapter 6:  Numerical Simulation of CNT-based Damping in Rotating Composite Structures**

This last portion of this dissertation presents the results of numerical simulations exploring the effect of CNT damping, angular speed, and geometric variation on the dynamic response of various rotating composite structures. The numerical model is first validated and subsequently used to quantify the performance of CNT-damped composites in terms of the structures maximum tip displacement and vibration settling time.

**6.1  Three-Dimensional Rotating Beam Model**

The fundamental goal of this portion of the dissertation is to investigate the effects of CNT damping on rotating composite structures subject to various angular speed profiles using the finite element method. To this end, Figure 30a presents a general schematic of the rotating structure configuration, illustrated using a simple rectangular beam of length $L$ attached to a rotating hub of radius $R$. The base of the beam is rigidly connected to the hub and is described by cantilever boundary conditions. A Cartesian coordinate system is defined at the base of the beam with the origin lying at the center of beam's base as indicated in Figure 30a. The rotation of the structure is oriented around the vertical central axis (positive z-direction) of the hub and is described by the angular speed, $\Omega$, with the coordinate system rotating at the same speed. A schematic of the dimensional angular speed profile specified at the base of the beam is shown in Figure 30c, consisting of a 'ramp' period where the speed is increased linearly from zero and a 'hold' period where the speed is held constant. The ramp period is defined by the steady-state angular speed, $\Omega_0$, and the time to reach this final speed (i.e. the ramp time), $t_0$, as denoted in Figure 30c.

As a first-order modeling approach, the composite beam is considered to be isotropic with homogeneous properties, where the issues of orthotropic and heterogeneous composite material

properties will be addressed in future iterations of the current model. The governing physics of the

solid rotating beam are described by the conservation of momentum equation [91], written as

$$\rho \frac{\partial^2 u}{\partial t^2} - \nabla \cdot \left( \frac{EI}{A} \nabla u \right) - (F_v + F_c + F_r) = 0 \tag{38}$$

where $\rho$, $E$, $I$, and $A$ are the density, modulus, moment of inertia, and cross-sectional area of the

specific geometry of study, respectively, $u$ is the displacement vector of the structure, and $F_v$, $F_c$,

and $F_r$ are the viscous, structural coulomb, and rotational body force vectors, respectively. The

viscous damping model is applied to describe the composite material damping without CNTs, and

the effect of the matrix-embedded CNTs is described by the structural coulomb friction model

based on the assumption of stick-slip action between the CNT-resin interface [54,78]. Using a first

mode assumption, the viscous and coulomb friction damping models can be expressed as body

forces [99,100], written, respectively, as:

$$F_v = \delta_v \rho \omega_1 \frac{\partial u}{\partial t} \tag{39}$$

$$F_c = \delta_c \rho \omega_1^2 |u| sgn\left( \frac{\partial u}{\partial t} \right) \tag{40}$$

where the subscripts $v$ and $c$ represent viscous and coulomb damping, respectively, $\delta$ is the

material loss factor, $\omega_1$ is the first natural frequency of the structure, and $sgn()$ is the signum

function which returns the sign of its argument. The values for the material loss factor in Equation

39 and Equation 40 are obtained from experimental damping measurements of CNT-infused,

carbon-fiber reinforced composite beams with a fiber volume fraction of 0.58 presented in Chapter

4.3 and [79], simplified as

$$\delta_v = 0.0359 \varepsilon^{0.08} \tag{41}$$

$$\delta_c = 0.0359 \left[ (\alpha^{0.172} + 1) \varepsilon^{(0.0492 + 0.0308 e^{-1.11\alpha})} - \varepsilon^{(0.08)} \right] \tag{42}$$

where $\varepsilon$ is the material strain and $\alpha$ is the CNT weight percentage loading within the composite matrix. These two equations are valid for material strain values ranging from 0 to 0.05 percent and CNT weight percentage loadings from zero to two weight percent, which fall within the range of parameters used in the current numerical simulations. It is evident from inspection of Equation 41 and Equation 42 that each damping function increases monotonically with increasing strain, and that the predicted damping in Equation 42 is zero when $\alpha = 0$ and increases at higher CNT weight percentage values. Together, Equation 39–Equation 42 describe the strain-dependent damping loads which affect the beam during the transient simulation cases and allow the effect of various CNT weight percentage loadings to be explored on the resulting beam dynamics.

To account for the effects of rotation on the composite structure, the geometry is modeled in a rotating frame of reference and results in a body load vector expressed in general as

$$F_r = \rho \left( \Omega e \times (\Omega e \times u) + \frac{\partial \Omega}{\partial t} e \times u + 2\Omega e \times \frac{\partial u}{\partial t} \right) \tag{43}$$

where the subscript $r$ denotes rotation and $e$ is a unit-length vector describing the axis of rotation. In the current simulation, each geometry is considered to rotate around the z-axis in a counter-clockwise fashion when looking in the negative z-direction from above the system, and therefore $e = (0,0,1)$. The first term in Equation 43 represents the centrifugal force, the second term is the Euler force arising from the angular acceleration of the system, and the last term is referred to as the Coriolis force. To complete the necessary modeling requirements, the rotating structure is considered to be cantilevered at its base at a fixed distance from the axis of rotation, $R$, representing the radius of a centrally rotating hub, as illustrated in Figure 30a. These boundary conditions are given by

$$u(t, x = R, y, z) = 0 \tag{44}$$

$$\frac{\partial u}{\partial x}(t, x = R, y, z) = \frac{\partial u}{\partial y}(t, x = R, y, z) = \frac{\partial u}{\partial z}(t, x = R, y, z) = 0 \tag{45}$$
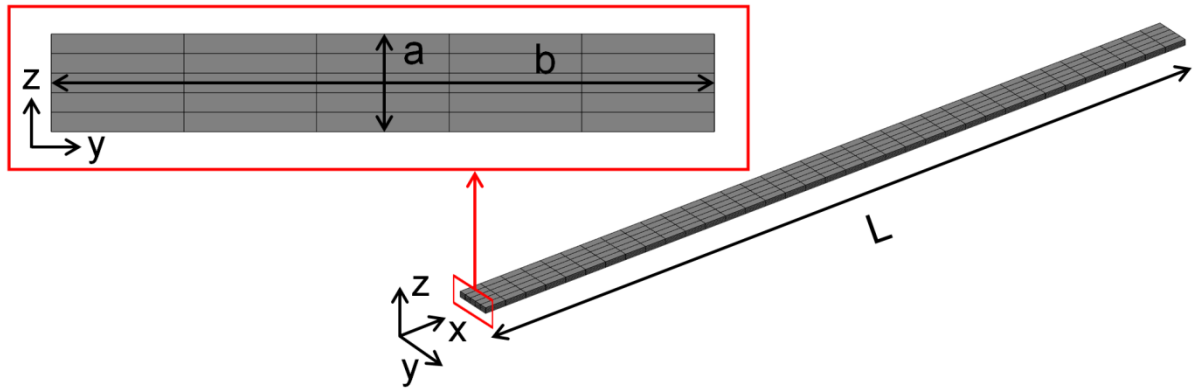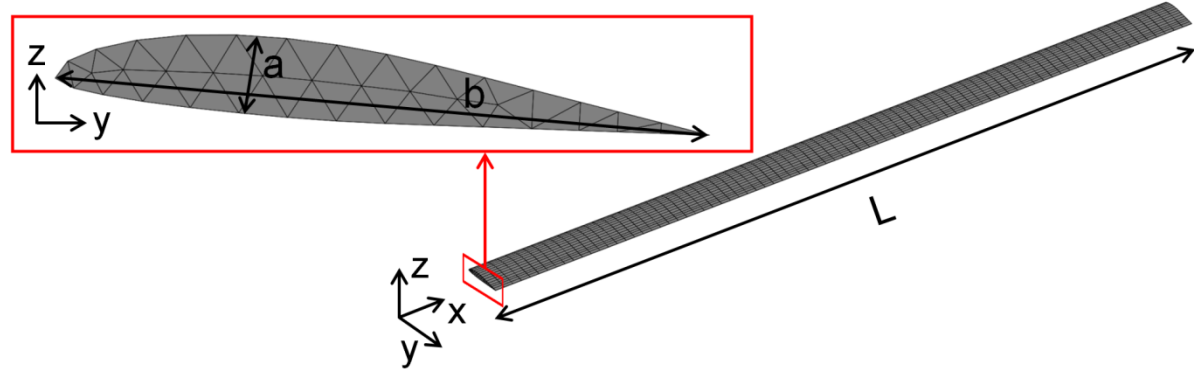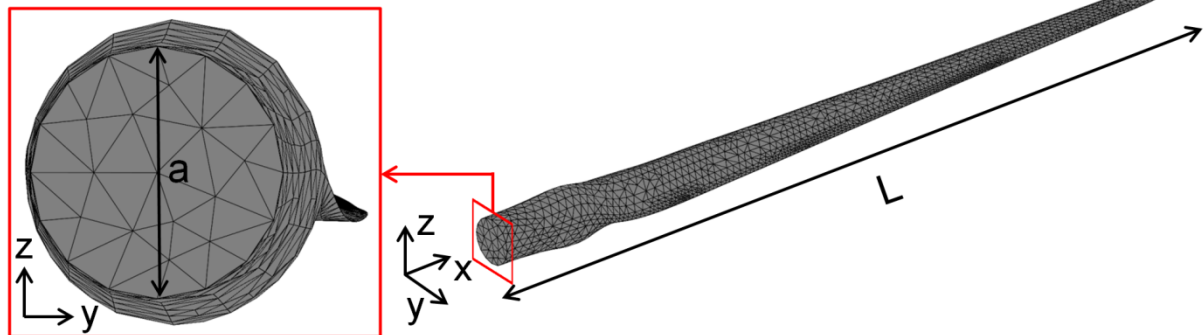
Figure 38: Geometry and mesh of the (a) simple beam, (b) Boeing VR7 helicopter rotor, and (c) NREL 5 MW wind turbine blade. The thickness, $a$, width, $b$, and length, $L$, of each geometry are also labeled.

and the remaining surfaces of the geometry are specified as free boundaries. In addition, each structure is considered to be initially at rest, written as:

$$\boldsymbol{u}(t = 0, x, y, z) = 0 \tag{46}$$

$$\frac{\partial \boldsymbol{u}}{\partial t}(t=0,x,y,z)=0 \tag{47}$$

where Equation 38–Equation 47 provide a full mathematical description of the physics of the rotating composite beam.

Three different rotating composite structures are studied separately according to the model developed above, and the various geometries and associated meshes are depicted in Figure 38: (a) a simple rectangular cantilever beam, (b) a helicopter rotor, and (c) a wind turbine blade. The geometry length, $L$, thickness, $a$, and width, $b$, of each structure is indicated in Figure 38 and the values of these geometric parameters are detailed in Table 5. A full three-dimensional isometric view of each geometry is presented along with a two-dimensional view looking down the x-axis from $x = 0$ to illustrate each respective structure. The simple beam is modeled according to the experimental study in [79] and is meshed with 875 hexahedral elements. A Boeing VR7 airfoil design is used to create the geometry for the helicopter rotor [88,121], and is meshed with 4,320 prism elements. The wind turbine blade geometry is modeled according to the NREL 5 MW offshore baseline wind turbine which uses various Delft University (DU) and national advisory committee for aeronautics (NACA) airfoils over the length of the structure [89,121–124], and is meshed with 11,300 tetrahedral elements.

Equation 38–Equation 47 are applied to these different composite structures and solved with the commercially available finite element (FE) software package COMSOL© (Burlington, MA)

Table 5: Parameter values describing the three composite structures considered in the study.

| Geometry | Length, $L$ [$m$] | Thickness, $a$ [$m$] | Width, $b$ [$m$] | Hub Radius, $R$ [$m$] | Natural Frequency, $\omega_1$ [$Hz$] |
|---|---|---|---|---|---|
| Simple Beam | 0.295 | 0.00187 | 0.0126 | 0.0700 | 22.1 |
| Helicopter Rotor | 5.00 | 0.120 | 0.250 | 0.250 | 4.19 |
| Wind Turbine Blade | 60.0 | 3.52 | N/A | 1.50 | 0.689 |

using the SPOOLES solver [125] with an absolute tolerance of $1 \times 10^{-5}$, the backwards differentiation formula (BDF) time-stepping algorithm [91], and Green-Lagrange strains which take into account the geometric nonlinearity of the structural dynamics [126]. Mesh and time step convergence studies are conducted to verify the calculated solutions are independent of the discretization. Each of the three structures are considered to be connected to a central rotating hub with cantilever boundary conditions at the base of the beam, as is illustrated in Figure 30a and described above. A parametric study is conducted to explore the relative effects of CNT weight percentage loading, angular speed profile, and geometric values on the numerical simulation results of each composite structure, presented below.

## 6.2  Model Validation

Using the numerical model developed in Chapter 6.1, an initial eigenfrequency study is undertaken to determine the natural frequency values and mode shapes of the different composite structures compared to published results in the literature, where the composite material is modeled with a modulus, $E$, of 59 *GPa* and a density, $\rho$, of 1450 *kg/m³*. The natural frequency values, $\omega_1$, and the normalized mode shapes describing the first transverse mode of vibration for the stationary (i.e. $\Omega = 0$) simple beam, helicopter rotor, and wind turbine are shown in Figure 39a, Figure 39b, and Figure 39c, respectively. Both the simple beam and the helicopter rotor have a constant cross-section along the x-direction, and therefore the mode shape in each case behaves similar to an ideal Euler-Bernoulli beam [99]. Conversely, the geometry of the wind turbine is more complicated with a thick base that tapers when moving towards the tip of the beam in the positive x-direction. This results in a mode shape with the majority of the displacement occurring at the free end of the beam, differing significantly from the mode shapes of the simple beam and the helicopter rotor.

115
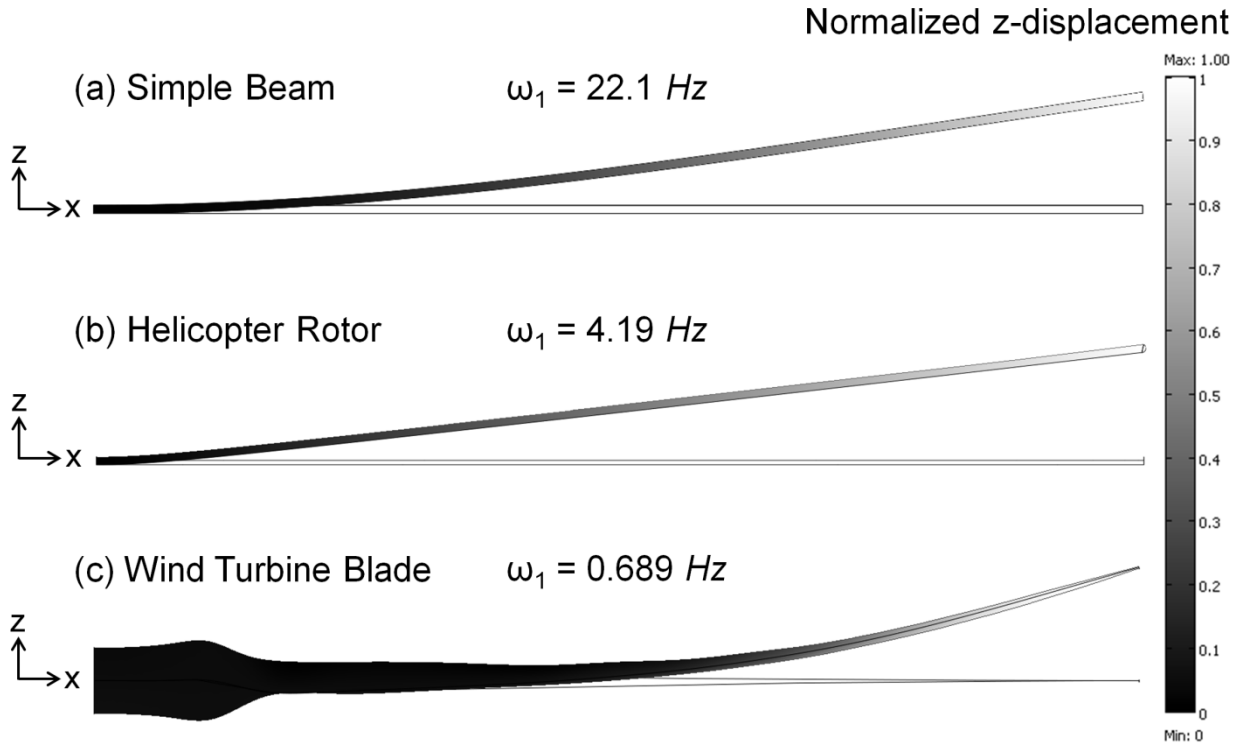
Figure 39: Geometry and mesh of the (a) simple beam, (b) Boeing VR7 helicopter rotor, and (c) NREL 5 MW wind turbine blade. The thickness, $a$, width, $b$, and length, $L$, of each geometry are also labeled.

From the first transverse natural frequency values of each structure noted in Figure 39, it is evident that $\omega_1 = 22.1$ for the simple beam, which is an order of magnitude higher than the helicopter rotor with $\omega_1 = 4.19$, which in turn is an order of magnitude greater than the value of $\omega_1 = 0.689$ for the wind turbine blade, a trend reflecting the difference in the cross-sectional geometry and the length of the different structures considered.

The effect of the steady-state angular speed, $\Omega_0$, on the numerical predictions of the first two transverse natural frequency values of each fiber-reinforced composite structure without CNTs (i.e. $\alpha = 0\%$) is presented in Figure 40 as the dashed line with empty square markers, compared to various results found in the literature denoted by the solid lines. It is evident from the trends in Figure 40 that, in general, the first two transverse natural frequencies increase as the angular speed

116
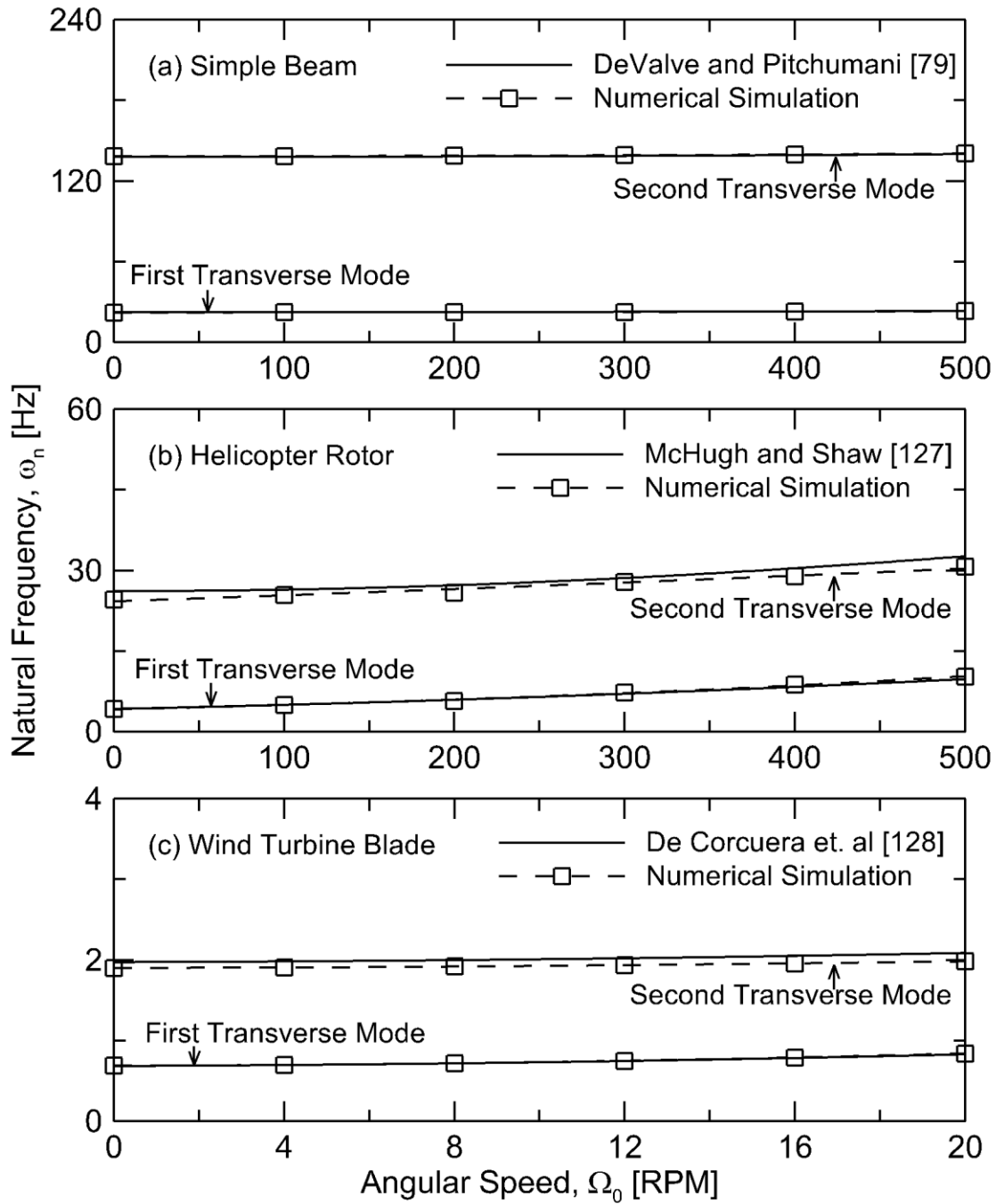
Figure 40: Comparison of the first and second transverse natural frequency values as a function of angular speed, $\Omega_0$, using the current numerical model shown with the dashed line and empty square markers for the (a) simple beam, (b) helicopter rotor, and (c) wind turbine blade compared with various results from the literature indicated with a solid line.

is increased from zero for each of the composite structures studied, referred to as the spin-stiffening effect [107]. Note that the values of $\Omega_0$ are different for the parameter sweep of each geometry, reflecting the practical operating ranges of the various structures. The numerical simulations of the simple beam are shown in Figure 40a, where the values in the first mode, $\omega_1$, range from 22.1 *Hz* at $\Omega_0 = 0$ *RPM* to 23.0 *Hz* at $\Omega_0 = 500$ *RPM*. In the second transverse mode, the numerical simulations predict values of $\omega_2$ ranging from 138–140 *Hz* when the angular speed is amplified from 0 to 500 *RPM*, demonstrating a larger increase in the second natural frequency than the augmentation observed in the first natural frequency over the same range of $\Omega_0$. The numerical simulations agree well with the experimental measurements presented in Figure 40a [79], with an average difference of less than 0.5% between the data for each individual mode.

Figure 40b presents the results of the helicopter rotor simulations, and for angular speed values of 0–500 *RPM* the values of $\omega_1$ and $\omega_2$ range from 4.19–10.2 *Hz* and 24.6–30.7 *Hz*, respectively. Here, the natural frequency values in both transverse modes increase by approximately 6 *Hz* as $\Omega_0$ is increased to 500 *RPM*. The numerical results of the helicopter rotor show good agreement with similar experimental trends presented in Figure 40b [127], with an average deviation of approximately 1% between the data in the first mode and 6% in the second mode. The simulations of the wind turbine blade are shown in Figure 40c for angular speed values of 0–20 *RPM*, and the frequencies range from 0.689–0.839 *Hz* and 1.90–1.98 *Hz* for $\omega_1$ and $\omega_2$, respectively. This data demonstrates good agreement with the analytical calculations presented in Figure 40c [128], where comparatively the current model predicts $\omega_1$ and $\omega_2$ values within 1% and 5%, respectively. The results presented in Figure 40 demonstrate that the current model predicts values consistent with analytical and experimental data in the literature for each respective composite structure,

supporting the validity of the numerical simulations reported throughout the remainder of this study.

## 6.3 Parametric Study

An example case of the numerical simulation results predicting the dynamic displacement at the free end of the simple beam (i.e. the tip displacement), $u_{x=L}$, is presented in Figure 41, using an angular speed profile defined by moderate excitation conditions of $\Omega_0 = 500\ RPM$ and $t_0 = 2$ $s$. Note that the absolute value of the tip displacement is reported to better illustrate the decay
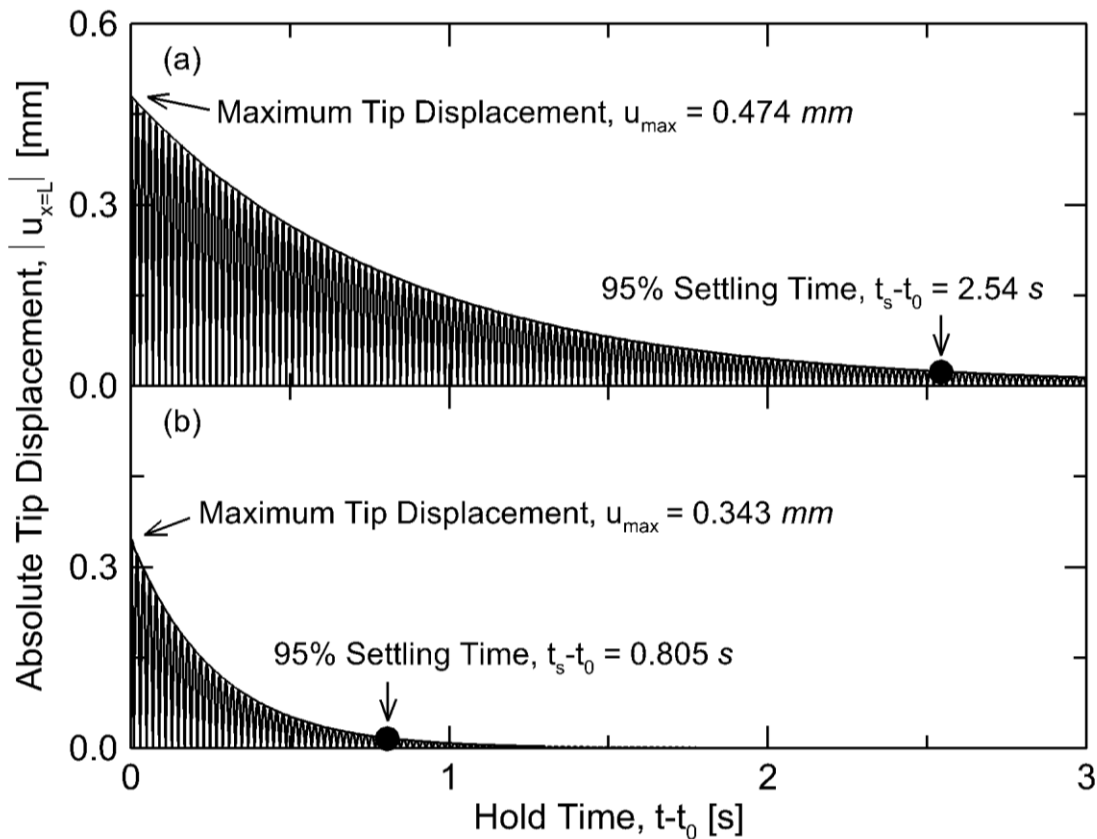


Figure 41: The absolute value of the displacement at the tip of the simple beam, $|u_{x=L}|$, during the hold period using $\Omega_0 = 500\ RPM$ and $t_0 = 2\ s$ for CNT weight percentage loadings of (a) $\alpha = 0\%$ and (b) $\alpha = 2\%$. The decay envelope of the vibrations are noted in each case with an exponential fit line and the filled circles represent the 95% settling times, $t_s - t_0$, for each respective simulation during the hold period. The respective maximum tip displacement, $u_{max}$, in each case is also noted.

119

envelope of the vibration data, and that the data in this figure—as well as the data presented throughout the rest of this work—is reported from the start of the hold period at $t = t_0$ (defined in Figure 30c) in order to best compare the different simulations as a function of steady-state angular speed, $\Omega_0$. The results in Figure 41a demonstrate the response of the beam without matrix-embedded CNTs, or equivalently $\alpha = 0\%$. In this case, the response has a maximum tip displacement, $u_{max}$, of 0.474 *mm* at the beginning of the hold period and 2.54 *s* elapse before the vibrations settle to 95% of their original value at $t_0$, defined as the *hold period settling time*, $t_s - t_0$, hereafter referred to as simply the *settling time*. Using the same composite structure and angular speed profile as the simulation in Figure 41a, Figure 41b presents the numerical results considering the addition of two weight percent CNTs ($\alpha = 2\%$) to the matrix of the composite beam. The response of the beam in this case shows a significant decrease in $u_{max}$ and $t_s$ compared to the results with $\alpha = 0\%$ in Figure 41a, where the maximum tip displacement is reduced by almost 28% compared to the baseline beam without CNTs and similarly the settling time is reduced by approximately 69%. The trends in Figure 41 serve as an illustration of the simulation results for the simple beam considering CNT damping effects. The graphical results for the helicopter rotor and the wind turbine blade geometries are similar in nature and are omitted for brevity, where for similar excitation conditions the values of $u_{max}$ and $t_s$ are decreased by 23% and 65%, respectively, for the helicopter rotor and by 21% and 48%, respectively, for the wind turbine blade with the addition of two weight percent CNTs.

Next, a parametric study is performed on each of the three different composite structures by varying the angular speed profile, CNT weight percentage loading, and geometry thickness to length ratio. The results are quantified by the normalized maximum tip displacement, $u^*$, and the normalized settling time, $t_s^*$, defined as $u^* = \frac{u_{max}}{L}$ and $t_s^* = \frac{t_s - t_0}{t_0}$ which allow a relative
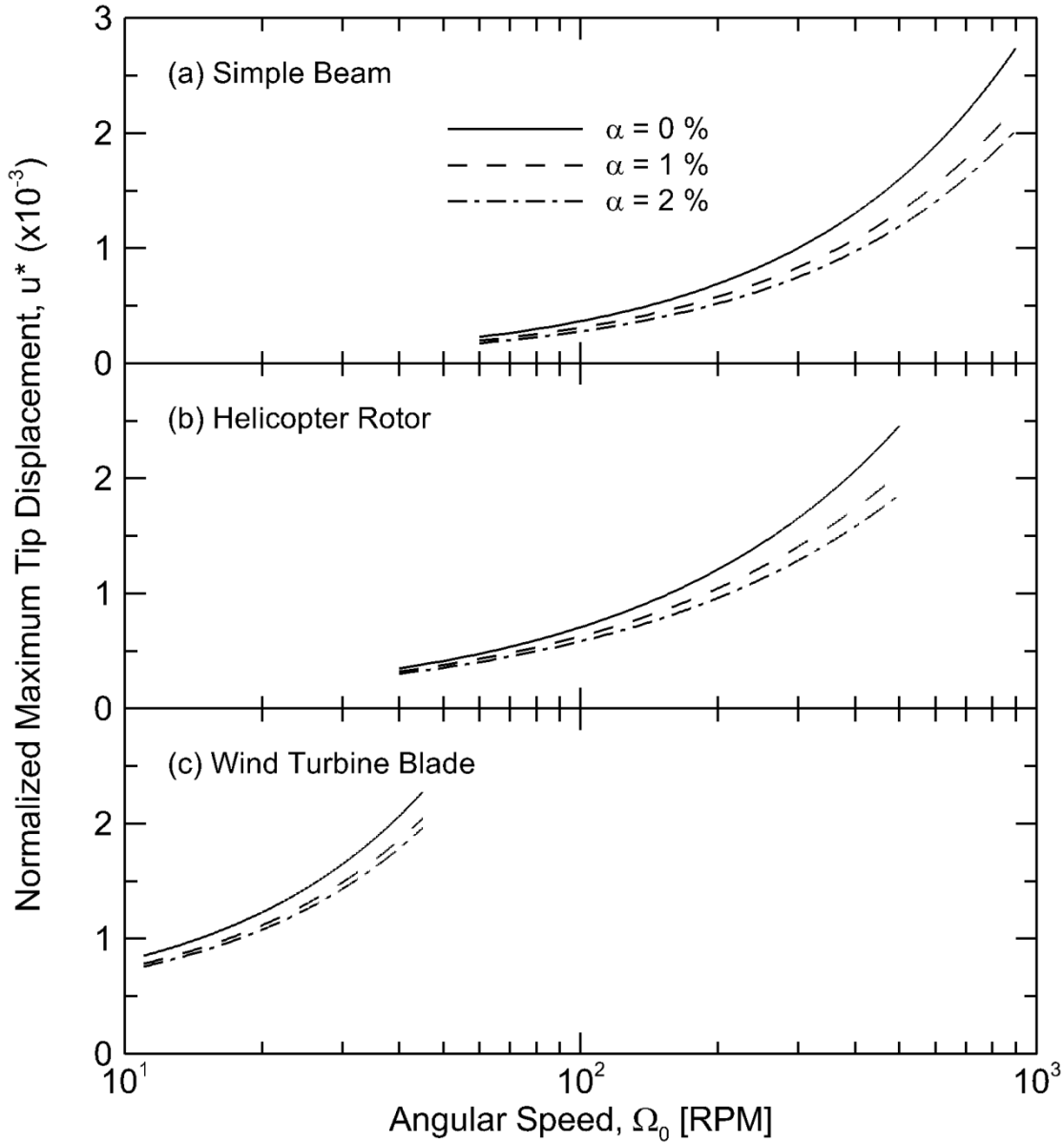
Figure 42: Normalized maximum tip displacement, $u^*$, ranging from 0 to $3 \times 10^{-3}$ for the (a) simple beam, (b) helicopter rotor, and (c) wind turbine blade during the hold period as a function of angular speed, $\Omega_0$, and various levels of CNT weight percentage loading, $\alpha$.

comparison to be made across all three geometries at similar scales, as presented in Figure 42–Figure 46 below.

The numerical results detailing the normalized maximum tip displacement, $u^*$, as a function of steady-state angular speed, $\Omega_0$, for various levels of CNT weight percentage loading, $\alpha$, are

121

presented for the simple beam, helicopter rotor, and wind turbine blade in Figure 42a, Figure 42b, and Figure 42c, respectively. For these numerical simulations the angular speed is varied while the ramp time, $t_0$, for each structure is held constant, where the values for $t_0$ are chosen based on estimated practical operating scenarios: In the case of the simple beam $t_0 = 2\ s$, $t_0 = 15\ s$ for the helicopter rotor, and $t_0 = 60\ s$ in the wind turbine blade simulations. Note that, although the geometry length scales differ significantly between each of the different composite structures, the values of the normalized maximum tip displacement for each structure fall within the range of 0 to $3 \times 10^{-3}$ for the different studied $\Omega_0$ values. From the trends in Figure 42 it is evident that $u^*$ increases at higher values of $\Omega_0$ for each geometry, which is due to the elevated loads on the composite as a result of the more rapid acceleration of the structure at higher steady-state angular speed values. In addition, as the CNT weight percentage loading within the composite matrix is increased, $u^*$ decreases across all values of $\Omega_0$, where this trend is most noticeable at higher angular speed values. Note that for each composite structure, the reduction in normalized maximum tip displacement from $\alpha = 0\%$ to $\alpha = 1\%$ is larger than the reduction in $u^*$ from $\alpha = 1\%$ to $\alpha = 2\%$. This trend suggests that the improvement in performance through reduction in $u^*$ by virtue of CNT damping is non-linear with respect to the CNT weight percentage loading, and that the benefits of adding more CNTs to the composite matrix (i.e. increasing $\alpha$) may eventually become inconsequential at the higher $\alpha$ values.

Figure 43 presents the normalized maximum tip displacement as a function of ramp time, $t_0$, considering a CNT weight percentage loading of $\alpha = 2\%$ for the simple beam, the helicopter rotor, and the wind turbine blade. The simulation results in Figure 43 present a variation in the ramp time of each respective geometry while the angular speed is held constant: the simple beam is driven at $\Omega_0 = 500\ RPM$, a value of $\Omega_0 = 200\ RPM$ is used for the helicopter rotor, and the
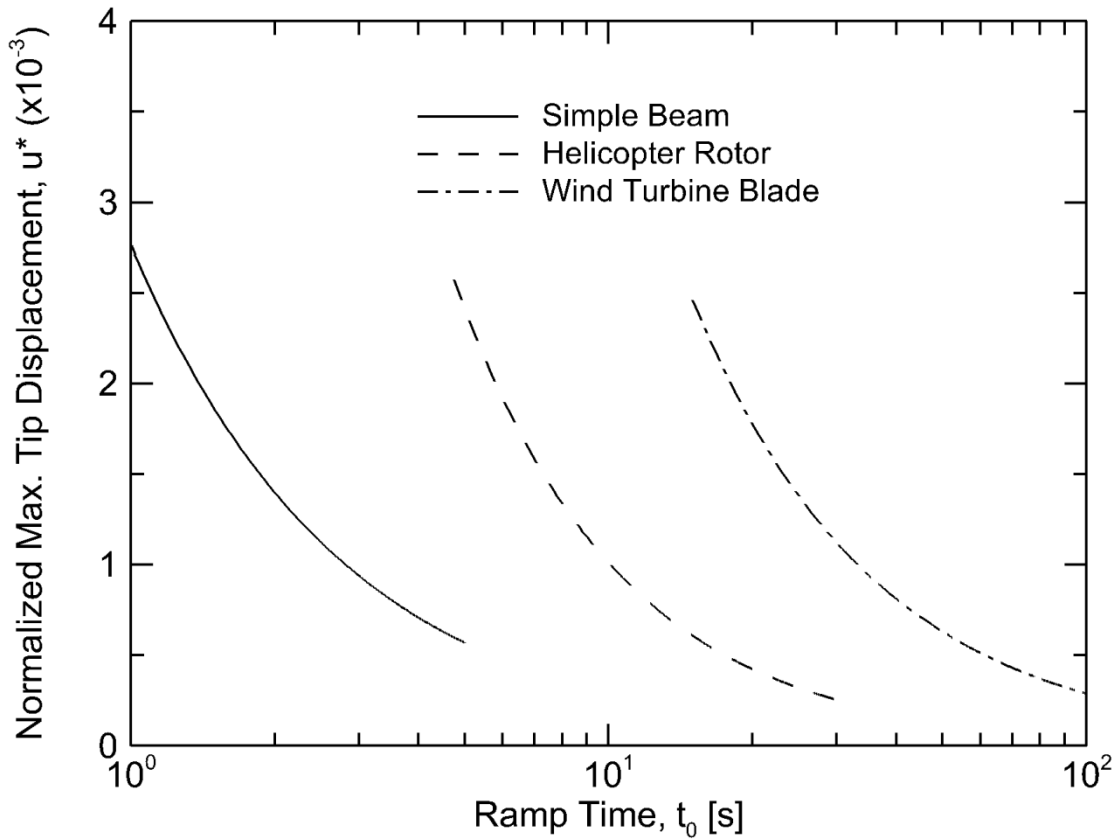
Figure 43: Normalized maximum tip displacement, $u^*$, of the (a) simple beam, (b) helicopter rotor, and (c) wind turbine blade during the hold period as a function of ramp time, $t_0$, for a CNT weight percentage loading of $\alpha = 2\%$.

wind turbine is rotated at $\Omega_0 = 8$ *RPM*. It is evident from the graphs in Figure 43 that $u^*$ decreases at higher values of $t_0$, a trend that, in general, is similar to the results with decreasing $\Omega_0$ presented in Figure 42. As is noted in the discussion of Figure 42, the increase in the acceleration of the structure during the ramp period results in larger loads on the material, which in turn causes higher deformations of the structure. It follows from inspection of the angular speed profile definition illustrated in Figure 30c that the acceleration will intensify with increasing $\Omega_0$ or decreasing $t_0$. Thus, it is evident that the predicted maximum tip displacement trends are similar when varying $\Omega_0$ with constant $t_0$ or with varying $t_0$ with constant $\Omega_0$, as shown in Figure 42 and Figure 43,

respectively. Therefore, the parameter variation of the angular speed profile throughout the remainder of the study is restricted to a variation of $\Omega_0$ at constant $t_0$ for succinctness.

The normalized settling times, $t_s^*$, of the vibrations in the different composite structures are shown in Figure 44 as a function of angular speed and CNT weight percentage loading. The
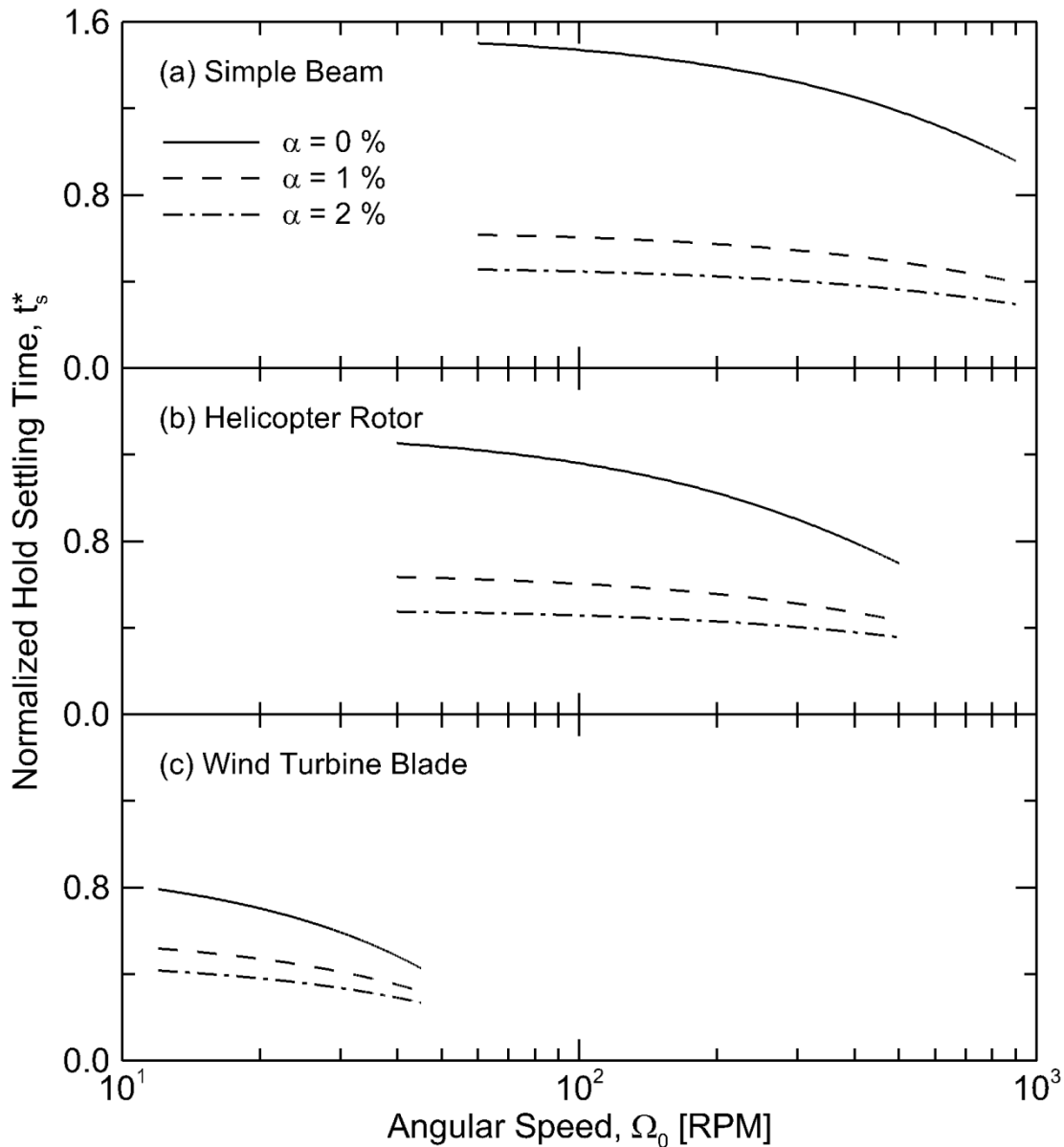


Figure 44: Normalized 95% settling time, $t_s^*$, for the (a) simple beam, (b) helicopter rotor, and (c) wind turbine blade during the hold period as a function of angular speed, $\Omega_0$, and various levels of CNT weight percentage loading, $\alpha$.

numerical simulation results with $t_0 = 2\ s$ for the simple beam are illustrated in Figure 44a, Figure 44b presents the helicopter rotor data using $t_0 = 15\ s$, and the wind turbine blade results with $t_0 = 60\ s$ are shown in Figure 44c. Note that the time scales used in the simulations of the different geometries are significantly different, however the data falls within 0 to 1.6 when normalized by the respective ramp time in each case. Generally, the $t_s^*$ values are largest in the case of the simple beam at constant $\alpha$ (Figure 44a), the $t_s^*$ data for the helicopter rotor is noticeably less than the simple beam results (Figure 44b), and the wind turbine settling times are the lowest of the three cases (Figure 44c), suggesting that the normalized settling times are longest for relatively shorter composite structures with higher natural frequencies. Comparable to the trends in Figure 42, it is evident that the CNT weight percentage loading has a significant effect on the structure's dynamic response, resulting in much lower values of $t_s^*$ as $\alpha$ is increased. Also, the decrease in the normalized settling time is greater from $\alpha = 0\%$ to $\alpha = 1\%$ than from $\alpha = 1\%$ to $\alpha = 2\%$, suggesting a nonlinear performance improvement of the structural dynamics in terms of decreasing $t_s^*$ with increasing CNT weight percent, a trend also noted in the $u^*$ results shown in Figure 42.

To explore the effect of varying the composite structure's geometry on the resulting values of $u^*$ and $t_s^*$ as a function of angular speed and CNT weight percent loading, a geometric thickness ratio is defined as $a^* = \frac{a_0}{a}$ where $a$ is the original thickness of the geometry as noted in Table 5 and $a_0$ is the thickness of the geometrically altered structure. For example, considering that the simple beam is described by $a = 1.87 \times 10^{-3}$, a geometrically altered beam characterized by $a^* = 0.5$ would have an actual thickness that is half of the original thickness, or $a_0 = 9.35 \times 10^{-4}$. This parametric variation is conducted using each of the three composite structures at values of $a^* = 0.5$ and $a^* = 2$. Since the trends in each case are similar, only the wind turbine blade simulations are presented for brevity as shown in Figure 45. The $u^*$ values for the wind turbine

125
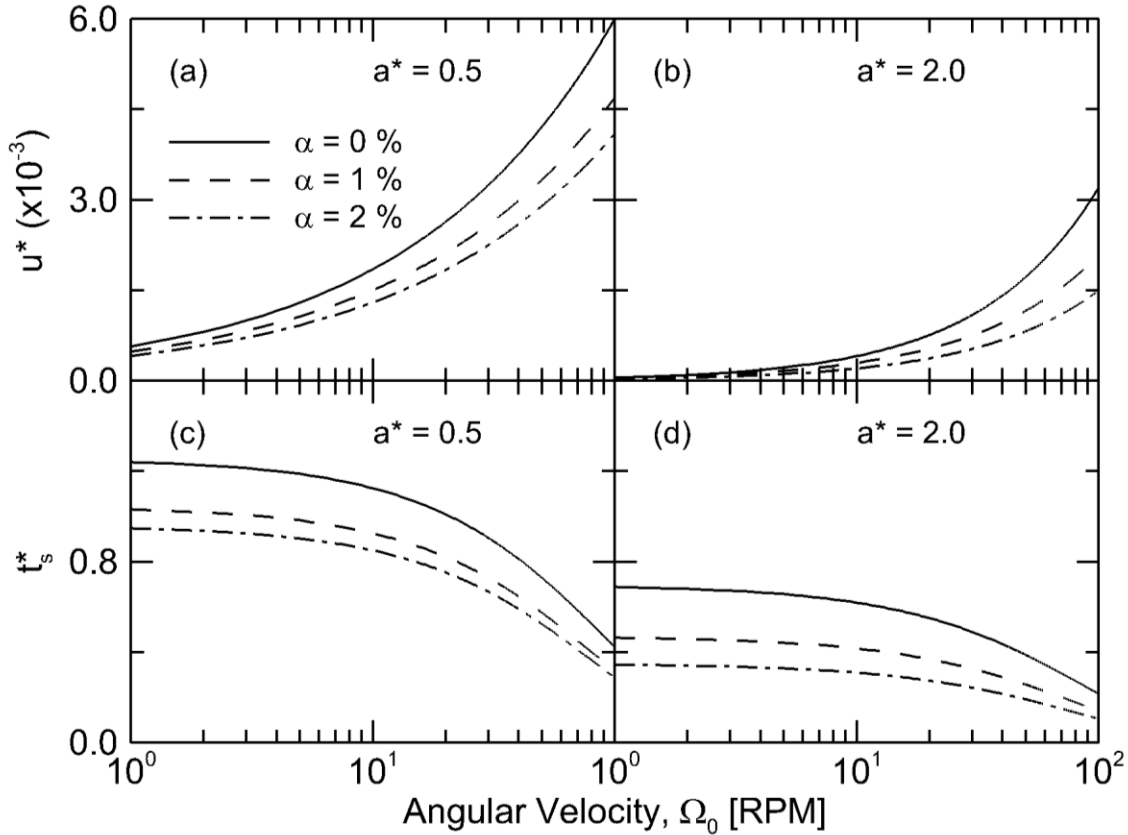
Figure 45: Normalized maximum tip displacement, $u^*$, for the wind turbine blade with a geometric thickness ratio, $a^*$, of (a) 0.5 and (b) 2.0, and normalized 95% settling time, $t_s^*$, for the simple beam with varying thickness values of $a^* =$ (c) 0.5 and (d) 2.0 as a function of angular speed, $\Omega_0$, and various levels of CNT weight percentage loading, $\alpha$.

blade with $a^* = 0.5$ and $a^* = 2$ are shown in Figure 45a and Figure 45b, respectively, and Figure 45c and Figure 45d present the values of $t_s^*$ for $a^* = 0.5$ and $a^* = 2$, respectively. In general, the trends in Figure 45 demonstrate that the numerical simulations predict values for both $u^*$ and $t_s^*$ which are greater for the thinner turbine blade with $a^* = 0.5$ (Figure 45a and Figure 45c) than for the beam with $a^* = 2$ (Figure 45b and Figure 45d) across all values of CNT weight percentage loading. This result indicates that the more slender blade is less able to resist the higher loads caused by angular acceleration, resulting in larger initial displacements of the beam and longer settling times. The trends in Figure 45 also demonstrate that the addition of CNTs to the
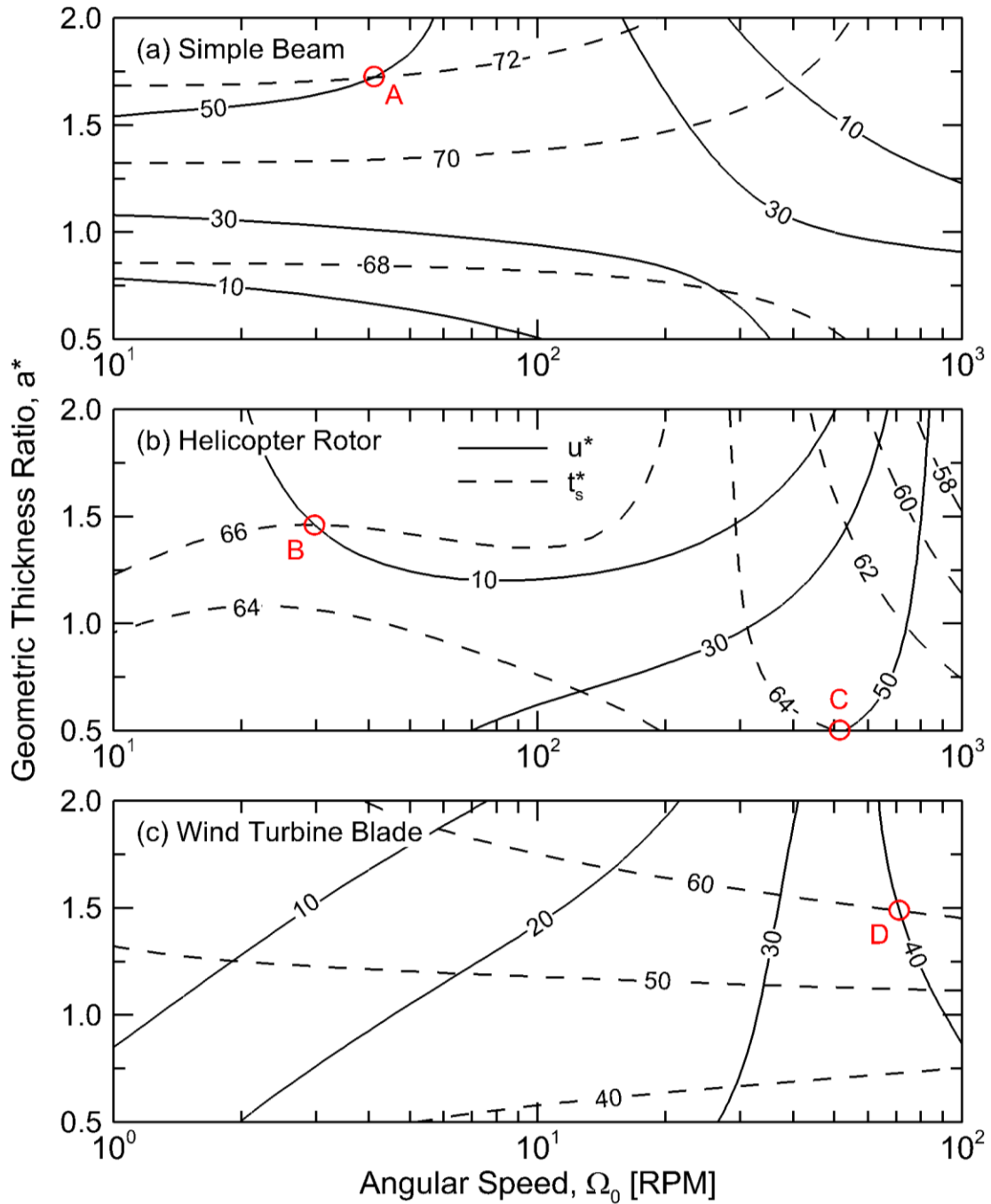
Figure 46: Contour plots of the average percentage decrease in maximum tip displacement, $u^*$, and settling time, $t_s^*$, shown by the solid and dashed lines, respectively, when incorporating two weight percent CNTs ($\alpha = 2\%$) in the composite matrix compared to the baseline composite without nanotubes ($\alpha = 0\%$) for the (a) simple beam, (b) helicopter rotor, and (c) wind turbine blade as a function of angular speed, $\Omega_0$, and the geometry thickness ratio, $a^*$.

composite matrix remains effective at reducing the displacements and settling times of the wind turbine blade for both thickness ratio cases. Again, as is noted in the discussion of Figure 42 and Figure 44 above, there is an apparent nonlinear increase in performance gains when increasing from 0 to 1 weight percent CNTs when compared to the increase from 1 to 2 weight percent CNTs. However, the difference in the results when $\alpha = 1\%$ versus $\alpha = 2\%$ remains significant, and future studies may address a cost-benefit analysis to determine an optimal CNT loading parameter.

Based on the results presented thus far, the improvement in performance by incorporating CNT damping in each composite structure is quantified by calculating the percentage decrease in $u^*$ and $t_s^*$, respectively, when the CNT loading is increased from zero to two weight percent. Contour maps of these percentage performance gains are presented for the simple beam, helicopter rotor, and wind turbine blade in Figure 46a, Figure 46b, and Figure 46c, respectively, as a function of the geometric thickness ratio, $a^*$, and angular speed, $\Omega_0$. The trends displayed by the contour lines of each structure are diverse, reflecting the various geometric complexities, length scales, and natural frequencies of each case. In Figure 46a for the simple beam, the decrease in $u^*$ and $t_s^*$ are maximized at approximately 50% (solid line) and 72% (dashed line), respectively, both occurring at a low angular speed of $\Omega_0 \approx 40$ *RPM* and a high $a^*$ value of $\approx 1.7$ (Point A in Figure 46a). For the helicopter rotor in Figure 46b, the percentage decrease in $t_s^*$ is similar to the trend in Figure 46a and is maximized at 66% (dashed line) for low to moderate angular velocities and high $a^*$ values, corresponding to a decrease in $u^*$ of 10% at $a^* \approx 1.5$ and $\Omega_0 \approx 30$ *RPM* (Point B in Figure 46b). However, the $u^*$ contour lines for the helicopter rotor show a different trend and demonstrate a maximum decrease of about 50% (solid line) for high angular speeds across all values of $a^*$, exhibited at $\Omega_0 \approx 500$ *RPM* and $a^* \approx 0.5$ for a decrease in $t_s^*$ of 64% (Point C in Figure 46b). In Figure 46c, the contours for the wind turbine geometry show that the decrease in $u^*$ is greatest at

40% (solid line) for a geometric thickness ratio greater than approximately 0.8 and high values of $\Omega_0$. In addition, the settling times are improved by up to 60% (dashed line) at high values of $a^*$ and moderate to high angular speeds. For example, the design Point D in Figure 46c at $\Omega_0 \approx 70\ RPM$ and $a^* \approx 1.5$ corresponds to a decrease in the maximum amplitude of 40% (solid line) and a decrease in the settling time of 60% (dashed line) by the addition of 2% CNT.

The trends shown in Figure 46 demonstrate that the addition of two weight percent CNTs to the composite matrix of each geometry has a significant impact on the structure's performance, decreasing the maximum tip displacement by 10–50% and the settling time by 40–72% across all simulation cases. In general, the $t_s^*$ values show a minor variation across the parameter sweep for each different structure, changing by about 4%, 8%, and 20% for the simple beam (Figure 46a), helicopter rotor (Figure 46b), and wind turbine blade (Figure 46c), respectively, between the different simulation cases. In contrast, the performance improvement in $u^*$ varies from 50 to 10 percent for the simple beam and helicopter rotor and from 40 to 10 percent for the wind turbine blade across the same parameter space, indicating that the maximum tip displacement has a greater dependence on the CNT weight percentage loading over the studied ranges of $\Omega_0$ and $a^*$. Figure 46 may be applied as a first-order design tool for developing operating ranges and geometric parameters of rotating composite structures with material damping augmentation from matrix-embedded CNTs.

This chapter developed a mathematical model of a rotating, cantilevered geometry and presented a parametric study of different rotating composite structures considering the effects of geometric variation, diverse angular velocities, and various levels of CNT damping. The conclusions drawn from this research along with the previous studies detailed in Chapter 2–Chapter 5 are presented in Chapter 7 to summarize the findings in this dissertation on composites

technology regarding void formation in composite molding processes and structural damping in fiber-reinforced composites with nanoscale reinforcements.

## 6.4 Nomenclature used in Chapter 6

$A$        cross-sectional area $[m^2]$

$a$        thickness of geometry $[m]$

$b$        width of geometry $[m]$

$E$        modulus of elasticity $[Pa]$

$I$        moment of inertia $[m^4]$

$L$        length of geometry $[m]$

$R$        hub radius $[m]$

$\boldsymbol{u}$        beam displacement vector $[m]$

$t_0$        ramp time $[s]$

$t_s$        settling time $[s]$


*Greek symbols*

$\alpha$        weight percent CNT loading $[\%]$

$\delta$        material damping loss factor

$\varepsilon$        strain $[\%]$

$\rho$        density $[kg/m^3]$

$\omega_n$        transverse natural frequency $[Hz]$

$\Omega$        angular speed $[RPM]$

$\Omega_0$        steady-state angular speed $[RPM]$

**Chapter 7: Conclusions and Future Work**

The presented studies provide significant contributions to composites technology in the areas of void formation prediction in composites processing and damping augmentation in fiber-reinforced composites using nanoscale reinforcement. Overall, the presented studies provide simulation tools for the improvement of composites manufacturing and insight into advanced composite material design for rotating composite structures through matrix-embedded CNTs.

**7.1 Numerical Simulation of Void Formation in LCM Processes**

In the first part of this dissertation, an analytical series solution was developed for the longitudinal fluid flow through aligned rigid fibers which was used to establish a relationship between the dimensionless permeability, $\bar{\kappa}$, the fiber volume fraction, $v_f$, the relative fiber arrangement, and the fiber packing angle. The results are valid for all fiber volume fractions, $v_f$, including the fiber packing limit. The analytical model together with the coefficients in Table 1 and Table 2 serve to obtain the values of the longitudinal flow permeability in simulation of resin flow through aligned fibrous media, providing a method for predicting the local longitudinal permeability of fiber tows in preform materials used in composites manufacturing.

Next, a numerical model was presented to investigate dual scale resin flow through two commercially-available nested plain weave preform architectures, considering capillary effects within each individual fiber bundle. The results of the numerical simulations were applied to illustrate the air entrapment locations within the fiber preform along with a quantitative prediction of the evolution and final size of the entrapped air voids. The steady state average and maximum void entrapment volumes were compared across different Reynolds and Capillary numbers, along with a description of the associated processing time needed for complete mold fill. Processing

under the competing considerations of simultaneously minimizing the final void content and the processing time were presented and the impact of processing choices on the resulting volume of air entrapment were discussed. Further, it was shown that simulation of the three dimensional flow through an exact plain weave preform architecture in nested configuration may be achieved in a computationally efficient manner without loss of accuracy through the assemblage of flow simulations through multiple two-dimensional planar cross sections.

## 7.2  CNT Damping in Fiber-Reinforced Composite Structures

The second portion of this dissertation presented an investigation of the damping enhancement provided to fiber reinforced composites from matrix embedded CNTs. The experimental study explored different weight percentages and types of CNTs along with a systematic examination of the ultrasonic processing time of the CNT-resin mixture in order to maximize the damping effect in the final composite. Stationary damping measurements were taken using dynamic mechanical analysis (DMA) and traditional modal analysis techniques to explore CNT-damping effects in composites with different fiber volume fractions, and a 133% increase in damping was observed in a carbon fiber reinforced composite with $v_f = 0.46$ and two weight percent SWCNTs. The final portion of the study focused on measuring the damping in rotating composite beams in order to study the effect of rotation on CNT-infused composite materials. It was found that CNTs may be increasingly effective at augmenting the damping as the angular velocity is increased, reflecting the strain-dependent nature of the CNT damping phenomenon. These results provide greater insight into the design of CNT-infused composites for applications such as helicopter rotors or wind turbines, which are currently fabricated from composite materials and would benefit from the reduction of vibrations through a passive damping mechanism such as matrix-embedded CNTs.

The dissertation also developed a numerical model, formulated using the Euler-Bernoulli beam equation in a rotating frame and solved using the finite element method, to describe the effects of CNT-based damping in a rotating fiber-reinforced composite beam. The model considered viscous damping of the matrix material along with the energy dissipation from the matrix-embedded CNTs in the composite, expressed using a stick-slip coulomb damping term describing the frictional behavior at the nanotube-matrix interface as the material is deformed. The model was validated with data from the literature and a systematic study of the governing dimensionless parameters was conducted to investigate the effects of the beam geometry, angular speed, and viscous and coulomb damping parameters on the dynamic response and vibration settling time of a rotating composite beam. An application of the numerical model was presented by considering the typical parameters of a helicopter rotor blade, to demonstrate the performance gains that may be achieved by employing matrix-embedded CNTs in the design. The simulations show that a dimensionless coulomb damping factor on the order of $10^{-3}$, that can be achieved with 1-2% by weight of CNT, can reduce the vibration settling time of a rotating composite beam by an average of 40–60%.

Lastly, this dissertation presented a parametric study on rotating composite structures considering the effects of geometric variation, diverse angular velocities, and various levels of CNT damping. A mathematical model of a rotating, cantilevered geometry was developed and the finite element method was applied to simulate three different composite structures, specifically a simple beam, a helicopter rotor, and a wind turbine blade. The dynamic results of the numerical simulations were quantified in terms of the normalized maximum tip displacement and the normalized settling time. These metrics were used to elucidate the effects of each parameter on the resulting structural dynamics, focusing primarily on the influence of CNT damping. To complete this portion of the dissertation, contour plots for each composite structure were presented to

133

summarize the percentage improvement in performance when incorporating two weight percent CNTs in the composite matrix, where the maximum tip displacements were found to improve by up to 50% and the settling times were improved by up to 72%.

## 7.3 Future Work

In future studies involving the longitudinal permeability prediction of aligned rigid fiber bundles, the model may be extended to include capillary forces in the governing physics to better quantify the capillary effects on the analytical longitudinal permeability predictions. The twisting of fiber bundles may also be included in this model to better reflect conditions found in physical woven fibrous preforms. Improvements may be made to the numerical void prediction model by including the effects of cure kinetics in the fluid modeling, and additional preform geometries may also be considered to widen the base of understanding about the location of voids in different preform fabrics. The model may also be extended to look at downstream flow field effects, the flow close to the mold edges, and more complex mold cavities found in physical composite manufacturing scenarios.

Future experimental work with matrix-embedded CNTs in fiber-reinforced composite materials may address the effects of different fiber materials (e.g. glass), various fabric types (e.g. unidirectional, random, etc.), and higher CNT weight percentage loadings on the resulting damping measurements. Further investigation may be undertaken to better understand how rotation affects the physics of the overall composite material and specifically the CNT-matrix interface, and how this interaction may be exploited to an engineering design advantage. The current model of the rotating composite beam considering CNT damping may be extended to include the effects of orthotropic and heterogeneous material properties to better simulate the composite material

effects on the structural dynamics of each geometry. In addition, higher modes of vibration and the associated modal damping parameters may be included in the governing equations to improve the accuracy of the current numerical model, and the effects of higher CNT weight percentage loadings within the composite material may also be considered.

## Bibliography

[1]     G. W. Jackson and D. F. James, "The permeability of fibrous porous media," *Canadian Journal of Chemical Engineering*, vol. 64, no. 3, pp. 364–374, 1986.

[2]     A. S. Sangani and C. Yao, "Transport processes in random arrays of cylinders. II. Viscous flow," *Physics of Fluids*, vol. 31, no. 9, p. 2435, 1988.

[3]     M. V Bruschke and S. G. Advani, "Flow of generalized Newtonian fluids across a periodic array of cylinders," *Journal of Rheology*, vol. 37, no. 3, p. 479, May 1993.

[4]     J. Happel, "Viscous flow relative to arrays of cylinders," *AIChE Journal*, vol. 5, no. 2, pp. 174–177, Jun. 1959.

[5]     E. M. Sparrow and A. L. Loeffler, "Longitudinal laminar flow between cylinders arranged in regular array," *AIChE Journal*, vol. 5, no. 3, pp. 325–330, Sep. 1959.

[6]     J. E. Drummond and M. I. Tahir, "Laminar viscous flow through regular arrays of parallel solid cylinders," *International Journal of Multiphase Flow*, vol. 10, no. 5, pp. 515–540, Oct. 1984.

[7]     C. Y. Wang, "Longitudinal flow through an array of rectangular cylinders," *IMA Journal of Applied Mathematics*, vol. 58, no. 2, pp. 111–120, Apr. 1997.

[8]     C. Y. Wang, "Longitudinal flow past cylinders arranged in a triangular array," *Applied Mathematical Modelling*, vol. 23, no. 3, pp. 219–230, Mar. 1999.

[9]     S. Toll, "A solution technique for longitudinal Stokes flow around multiple aligned cylinders," *Journal of Fluid Mechanics*, vol. 439, pp. 199–216, 2001.

[10]    R. Pitchumani and B. Ramakrishnan, "A fractal geometry model for evaluating permeabilities of porous preforms used in liquid composite molding," *International Journal of Heat and Mass Transfer*, vol. 42, no. 12, pp. 2219–2232, Jun. 1999.

[11]    B. Ramakrishnan and R. Pitchumani, "Fractal permeation characteristics of preforms used in liquid composite molding," *Polymer Composites*, vol. 21, no. 2, pp. 281–296, Apr. 2000.

[12]    S. Zhao and A. Povitsky, "Method of fundamental solutions for partial-slip fibrous filtration flows," *International Journal for Numerical Methods in Fluids*, vol. 61, no. 3, pp. 255–274, Sep. 2009.

[13]    N. D. Ngo and K. K. Tamma, "Microscale permeability predictions of porous fibrous media," *International Journal of Heat and Mass Transfer*, vol. 44, no. 16, pp. 3135–3145, Aug. 2001.

[14]    F. Zhou, N. Kuentzer, P. Simacek, S. G. Advani, and S. M. Walsh, "Analytic characterization of the permeability of dual-scale fibrous porous media," *Composites Science and Technology*, vol. 66, no. 15, pp. 2795–2803, Dec. 2006.

[15]    K. Han, C. W. Lee, and B. P. Rice, "Measurements of the permeability of fiber preforms and applications," *Composites Science and Technology*, vol. 60, no. 12–13, pp. 2435–2441, Sep. 2000.

[16]    A. Shojaei, "An experimental study of saturated and unsaturated permeabilities in resin transfer molding based on unidirectional flow measurements," *Journal of Reinforced Plastics and Composites*, vol. 23, no. 14, pp. 1515–1536, Sep. 2004.

[17]    E. Rodriguez, F. Giacomelli, and A. Vazquez, "Permeability-porosity relationship in RTM for different fiberglass and natural reinforcements," *Journal of Composite Materials*, vol. 38, no. 3, pp. 259–268, Feb. 2004.

[18]    A. Endruweit, K. S. Matthys, J. Peiro, and A. C. Long, "Effect of differential compression on in-plane permeability tensor of heterogeneous multilayer carbon fibre preforms," *Plastics, Rubber and Composites*, vol. 38, no. 1, pp. 1–9, Feb. 2009.

[19]    K. P. Brennan and D. E. Walrath, "Macroscale simulation of fiber bed impregnation utilizing microscale material properties," *Journal of Reinforced Plastics and Composites*, vol. 29, no. 8, pp. 1248–1266, May 2009.

[20]    K. P. Brennan, B. Straka, and D. E. Walrath, "Investigation of a simple tensorial permeameter," *Polymer Composites*, vol. 31, no. 3, pp. 434–442, 2010.

[21]    V. Antonucci, M. Esposito, M. R. Ricciardi, M. Raffone, M. Zarelli, and M. Giordano, "Permeability characterization of stitched carbon fiber preforms by fiber optic sensors," *Express Polymer Letters*, vol. 5, no. 12, pp. 1075–1084, Oct. 2011.

[22]    S. Sharma and D. A. Siginer, "Permeability measurement methods in porous media of fiber reinforced composites," *Applied Mechanics Reviews*, vol. 63, no. 2, p. 020802, 2010.

[23]    M. Li, S. Wang, Y. Gu, Z. Zhang, Y. Li, and K. Potter, "Dynamic capillary impact on longitudinal micro-flow in vacuum assisted impregnation and the unsaturated permeability of inner fiber tows," *Composites Science and Technology*, vol. 70, no. 11, pp. 1628–1636, Oct. 2010.

[24]    L. S. Han and A. A. Cosner, "Effective thermal conductivities of fibrous composites," *Journal of Heat Transfer*, vol. 103, no. 2, p. 387, 1981.

[25]    R. C. Averill and G. P. Carman, "Analytical modeling of micromechanical stress variations in continuous fiber-reinforced composites," in *IUTAM Symposium*, 1991, pp. 27–61.

[26]  S. G. Advani, *Flow and Rheology in Polymer Composites Manufacturing*. Elsevier Science, 1994, p. 626.

[27]  C. DeValve and R. Pitchumani, "An analytical model for the longitudinal permeability of aligned fibrous media," *Composites Science and Technology*, vol. 72, no. 13, pp. 1500–1507, Aug. 2012.

[28]  W. B. Young, "The effect of surface tension on tow impregnation of unidirectional fibrous preform in resin transfer molding," *Journal of Composite Materials1*, vol. 30, no. 11, pp. 1191–1209, 1996.

[29]  E. Bayramli and R. L. Powell, "Impregnation dynamics of carbon fiber tows," *Journal of Composite Materials*, vol. 26, no. 10, pp. 1427–1442, Jan. 1992.

[30]  K. M. Pillai, "Modeling the unsaturated flow in liquid composite molding processes: A review and some thoughts," *Journal of Composite Materials*, vol. 38, no. 23, pp. 2097–2118, Dec. 2004.

[31]  F. Trochu, E. Ruiz, V. Achim, and S. Soukane, "Advanced numerical simulation of liquid composite molding for process analysis and optimization," *Composites Part A: Applied Science and Manufacturing*, vol. 37, no. 6, pp. 890–902, Jun. 2006.

[32]  C. H. Park and L. Woo, "Modeling void formation and unsaturated flow in liquid composite molding processes: a survey and review," *Journal of Reinforced Plastics and Composites*, vol. 30, no. 11, pp. 957–977, Aug. 2011.

[33]  K. M. Pillai, "Governing equations for unsaturated flow through woven fiber mats. Part 1. Isothermal flows," *Composites Part A: Applied Science and Manufacturing*, vol. 33, no. 7, pp. 1007–1019, Jul. 2002.

[34]  R. S. Parnas, *Liquid Composite Molding*. Hanser Publishers, 2000, p. 170.

[35]  M. E. Foley, "Modeling the effect of fiber diameter and fiber bundle count on tow impregnation during liquid molding processes," *Journal of Composite Materials*, vol. 39, no. 12, pp. 1045–1065, Jun. 2005.

[36]  B. Gourichon, C. Binetruy, and P. Krawczak, "A new numerical procedure to predict dynamic void content in liquid composite molding," *Composites Part A: Applied Science and Manufacturing*, vol. 37, no. 11, pp. 1961–1969, Nov. 2006.

[37]  N. Patel and J. Lee, "Modeling of void formation and removal in liquid composite molding. Part II: Model development and implementation," *Polymer Composites*, vol. 17, no. 1, pp. 104–114, Feb. 1996.

[38] L. Labat, J. Bréard, S. Pillut-Lesavre, and G. Bouquet, "Void fraction prevision in LCM parts," *The European Physical Journal Applied Physics*, vol. 16, no. 2, pp. 157–164, Nov. 2001.

[39] H. Jinlian, L. Yi, and S. Xueming, "Study on void formation in multi-layer woven fabrics," *Composites Part A: Applied Science and Manufacturing*, vol. 35, pp. 595–603, 2004.

[40] M. A. A. Spaid and F. R. Phelan, "Modeling void formation dynamics in fibrous porous media with the lattice Boltzmann method," *Composites Part A: Applied Science and Manufacturing*, vol. 29, no. 7, pp. 749–755, Jul. 1998.

[41] E. Ruiz, V. Achim, S. Soukane, F. Trochu, and J. Breard, "Optimization of injection flow rate to minimize micro/macro-voids formation in resin transfer molded composites," *Composites Science and Technology*, vol. 66, no. 3–4, pp. 475–486, Mar. 2006.

[42] C. H. Park, A. Lebel, A. Saouab, J. Bréard, and W. Il Lee, "Modeling and simulation of voids and saturation in liquid composite molding processes," *Composites Part A: Applied Science and Manufacturing*, vol. 42, no. 6, pp. 658–668, Jun. 2011.

[43] J. S. U. Schell, M. Deleglise, C. Binetruy, P. Krawczak, and P. Ermanni, "Numerical prediction and experimental characterisation of meso-scale-voids in liquid composite moulding," *Composites Part A: Applied Science and Manufacturing*, vol. 38, no. 12, pp. 2460–2470, Dec. 2007.

[44] C. Soutis, "Carbon fiber reinforced plastics in aircraft construction," *Materials Science and Engineering: A*, vol. 412, no. 1–2, pp. 171–176, Dec. 2005.

[45] A. M. K. Esawi and M. M. Farag, "Carbon nanotube reinforced composites: Potential and current challenges," *Materials & Design*, vol. 28, no. 9, pp. 2394–2401, Jan. 2007.

[46] M. O. L. Hansen, J. N. Sørensen, S. Voutsinas, N. Sørensen, and H. A. Madsen, "State of the art in wind turbine aerodynamics and aeroelasticity," *Progress in Aerospace Sciences*, vol. 42, no. 4, pp. 285–330, Jun. 2006.

[47] J.-S. Jang, J. Varischetti, and J. Suhr, "Strain dependent energy dissipation in multi-scale carbon fiber composites containing carbon nanofibers," *Carbon*, vol. 50, no. 11, pp. 4283–4277, May 2012.

[48] B. Wetzel, F. Haupert, and M. Q. Zhang, "Epoxy nanocomposites with high mechanical and tribological performance," *Composites Science and Technology*, vol. 63, no. 14, pp. 2055–2067, Nov. 2003.

[49] E. T. Thostenson, Z. Ren, and T.-W. Chou, "Advances in the science and technology of carbon nanotubes and their composites: a review," *Composites Science and Technology*, vol. 61, no. 13, pp. 1899–1912, Oct. 2001.

[50] M. Moniruzzaman and K. I. Winey, "Polymer nanocomposites containing carbon nanotubes," *Macromolecules*, vol. 39, no. 16, pp. 5194–5205, Aug. 2006.

[51] R. F. Gibson, E. O. Ayorinde, and Y.-F. Wen, "Vibrations of carbon nanotubes and their composites: A review," *Composites Science and Technology*, vol. 67, no. 1, pp. 1–28, 2007.

[52] H. Rajoria and N. Jalili, "Passive vibration damping enhancement using carbon nanotube-epoxy reinforced composites," *Composites Science and Technology*, vol. 65, no. 14, pp. 2079–2093, 2005.

[53] K. Lau and D. Hui, "The revolutionary creation of new advanced materials - carbon nanotube composites," *Composites Part B: Engineering*, vol. 33, no. 4, pp. 263–277, 2002.

[54] J. Suhr and N. A. Koratkar, "Energy dissipation in carbon nanotube composites: a review," *Journal of Materials Science*, vol. 43, no. 13, pp. 4370–4382, Apr. 2008.

[55] N. A. Koratkar, J. Suhr, A. Joshi, R. S. Kane, L. S. Schadler, P. M. Ajayan, and S. Bartolucci, "Characterizing energy dissipation in single-walled carbon nanotube polycarbonate composites," *Applied Physics Letters*, vol. 87, pp. 1–3, 2005.

[56] J. Zhu, J. Kim, H. Peng, J. L. Margrave, V. N. Khabashesku, and E. V. Barrera, "Improving the dispersion and integration of single-walled carbon nanotubes in epoxy composites through functionalization," *Nano Letters*, vol. 3, no. 8, pp. 1107–1113, Aug. 2003.

[57] J. A. Kim, D. G. Seong, T. J. Kang, and J. R. Youn, "Effects of surface modification on rheological and mechanical properties of CNT/epoxy composites," *Carbon*, vol. 44, no. 10, pp. 1898–1905, Aug. 2006.

[58] J. Che, W. Yuan, G. Jiang, J. Dai, S. Y. Lim, and M. B. Chan-Park, "Epoxy composite fibers reinforced with aligned single-walled carbon nanotubes functionalized with generation 0−2 dendritic poly(amidoamine)," *Chemistry of Materials*, vol. 21, no. 8, pp. 1471–1479, Apr. 2009.

[59] M. T. Byrne and Y. K. Gun'ko, "Recent advances in research on carbon nanotube-polymer composites.," *Advanced materials (Deerfield Beach, Fla.)*, vol. 22, no. 15, pp. 1672–88, Apr. 2010.

[60] X. Zhou, K. W. Wang, and C. E. Bakis, "The investigation of carbon nanotube based polymers for improved structural damping," *Smart Structures and Materials*, vol. 5386, pp. 162–173, 2004.

[61] R. L. Dai and W. H. Liao, "Fabrication, testing, and modeling of carbon nanotube composites for vibration damping," *Journal of Vibration and Acoustics*, vol. 131, no. 5, pp. 1–9, 2009.

[62] R. M. Lin and C. Lu, "Modeling of interfacial friction damping of carbon nanotube-based nanocomposites," *Mechanical Systems and Signal Processing*, vol. 24, no. 8, pp. 2996–3012, 2010.

[63] R. F. Gibson, "A review of recent research on mechanics of multifunctional composite materials and structures," *Composite Structures*, vol. 92, no. 12, pp. 2793–2810, Nov. 2010.

[64] E. A. Lass, N. A. Koratkar, P. M. Ajayan, B. Q. Wei, and P. Keblinski, "Damping and stiffness enhancement in composite systems with carbon nanotubes films," in *Material Research Society Symposium*, 2003, pp. 371–376.

[65] N. A. Koratkar, B. Wei, and P. M. Ajayan, "Multifunctional structural reinforcement featuring carbon nanotube films," *Composites Science and Technology*, vol. 63, no. 11, pp. 1525–1531, 2003.

[66] M. Damu, A. Lumsdaine, and M. Parsons, "Topology optimization of carbon nanotube reinforced composite laminated structures for vibration damping," in *SPIE Conference on Smart Structures and Materials 2005: Damping and Isolation*, 2005, pp. 188–195.

[67] M. Ray and R. Batra, "A single-walled carbon nanotube reinforced 1-3 piezoelectric composite for active control of smart structures," *Smart Materials and Structures*, vol. 16, no. 5, pp. 1936–1947, 2007.

[68] J. Suhr, N. A. Koratkar, P. Keblinski, and P. M. Ajayan, "Viscoelasticity in carbon nanotube composites," *Nature Materials Letters*, vol. 4, pp. 134–137, 2005.

[69] S. N. Mahmoodi, S. E. Khadem, and N. Jalili, "Theoretical development and closed-form solution of nonlinear vibrations of a directly excited nanotube-reinforced composite cantilevered beam," *Arch Appl Mech*, vol. 75, no. 2–3, pp. 153–163, 2006.

[70] M. V Kireitseu, D. Hui, and G. R. Tomlinson, "Advanced shock-resistant and vibration damping of nanoparticle-reinforced compisite material," *Composites Part B: Engineering*, vol. 39, no. 1, pp. 128–138, 2008.

[71] M.-K. Yeh and T.-H. Hsieh, "Dynamic properties of sandwich beams with MWNT/polymer nanocomposites as core materials," *Composites Science and Technology*, vol. 68, no. 14, pp. 2930–2936, 2008.

[72] R. L. Dai and W. H. Liao, "Modeling of carbon nanotube composites for vibration damping," in *Proceedings of SPIE*, 2007, vol. 6528, pp. 652809–652809–10.

[73] X. Zhou, E. Shin, K. W. Wang, and C. E. Bakis, "Interfacial damping characteristics of carbon nanotube-based composites," *Composites Science and Technology*, vol. 64, no. 15, pp. 2425–2437, 2004.

[74]  M. V Kireitseu, G. R. Tomlinson, A. V Ivanenko, and L. V Bochkareva, "Dynamics and vibration damping behavior of advanced meso/nanoparticle-reinforced composites," *Mechanics of Advanced Materials and Structures*, vol. 14, no. 8, pp. 603–617, 2007.

[75]  J. Suhr, N. A. Koratkar, and P. Ajayan, "Damping characterization of carbon nanotube thin films," in *SPIE Conference on Smart Structures and Materials 2004: Damping and Isolation*, 2004, pp. 153–161.

[76]  S. U. Khan, C. Y. Li, N. A. Siddiqui, and J.-K. Kim, "Vibration damping characteristics of carbon fiber-reinforced composites containing multi-walled carbon nanotubes," *Composites Science and Technology*, vol. 71, no. 12, pp. 1486–1494, 2011.

[77]  M. Tehrani, M. Safdari, S. W. Case, and M. S. Al-Haik, "Using multiscale carbon fiber/carbon nanotubes composites for damping applications," in *ASME 2011 Conference on Smart Materials, Adaptive Structures, and Intelligent Systems*, 2011, pp. 1–5.

[78]  R. J. Johnson, J. Tang, and R. Pitchumani, "Characterization of damping in carbon-nanotube filled fiberglass reinforced thermosetting-matrix composites," *Journal of Materials Science*, vol. 46, no. 13, pp. 4545–4554, Feb. 2011.

[79]  C. DeValve and R. Pitchumani, "Experimental investigation of the damping enhancement in fiber-reinforced composites with carbon nanotubes," *Carbon*, vol. In Review, 2013.

[80]  S. Murugan and R. Ganguli, "Aeroelastic stability enhancement and vibration supression in a composite helicopter rotor," *Journal of Aircraft*, vol. 42, no. 4, pp. 1013–1024, 2005.

[81]  U. Dalli and S. Yuksel, "Identification of flap motion parameters for vibration reduction in helicopter rotors with multiple active trailing edge flaps," *Shock and Vibration*, vol. 18, pp. 727–745, 2011.

[82]  T. K. Barlas and G. A. M. van Kuik, "Review of state of the art in smart rotor control research for wind turbines," *Progress in Aerospace Sciences*, vol. 46, no. 1, pp. 1–27, 2010.

[83]  D. Patt, L. Liu, J. Chandrasekar, D. S. Bernstein, and P. P. Friedmann, "Higher-harmonic-control algorithm for helicopter vibration reduction revisited," *Journal of Guidance, Control, and Dynamics*, vol. 28, no. 5, pp. 918–930, 2005.

[84]  H. Tan, L. Y. Jiang, Y. Huang, B. Liu, and K. C. Hwang, "The effect of van der Waals-based interface cohesive law on carbon nanotube-reinforced composite materials," *Composites Science and Technology*, vol. 67, no. 14, pp. 2941–2946, Nov. 2007.

[85]  Y. Huang and X. W. Tangpong, "A distributed friction model for energy dissipation in carbon nanotube-based composites," *Communications in Nonlinear Scientific Numerical Simulations*, vol. 15, no. 12, pp. 4171–4180, 2010.

[86] P. P. Friedmann and T. A. Millott, "Vibration reduction in rotorcraft using active control: A comparison of various approaches," *Journal of Guidance, Control, and Dynamics*, vol. 18, no. 4, pp. 664–673, 1995.

[87] J. Chung and H. H. Yoo, "Dynamic analysis of a rotating cantilever beam by using the finite element method," *Journal of Sound and Vibration*, vol. 249, no. 1, pp. 147–164, Jan. 2002.

[88] D. Weaver, K. McAlister, and J. Tso, "Control of VR-7 dynamic stall by strong steady blowing," *Journal of Aircraft*, vol. 41, no. 6, pp. 1404–1413, Nov. 2004.

[89] Y. Bazilevs, M. C. Hsu, I. Akkerman, S. Wright, K. Takizawa, B. Henicke, T. Spielman, and T. E. Tezduyar, "3D simulation of wind turbine rotors at full scale. Part I: Geometry modeling and aerodynamics," *International Journal for Numerical Methods in Fluids*, vol. 65, no. 1–3, pp. 207–235, 2011.

[90] B. R. Munson, D. F. Young, and T. H. Okiishi, *Fundamentals of Fluid Mechanics*. Wiley, 2005, p. 816.

[91] E. Kreyszig, *Advanced Engineering Mathematics*, 9th ed. Hoboken, NJ: John Wiley & Sons, Inc., 2006.

[92] C. W. Hirt and B. D. Nichols, "Volume of fluid (VOF) method for the dynamics of free boundaries," *Journal of Computational Physics*, vol. 39, no. 1, pp. 201–225, Jan. 1981.

[93] J. U. Brackbill, D. B. Kothe, and C. Zemach, "A continuum method for modeling surface tension," *Journal of Computational Physics*, vol. 100, no. 2, pp. 335–354, Jun. 1992.

[94] Y. W. Zhang and A. Faghri, "Numerical simulation of condensation on a capillary grooved structure," *Numerical Heat Transfer Part A: Applications*, vol. 39, no. 3, pp. 227–243, 2001.

[95] R. I. Issa, B. Ahmadi-Befrui, K. R. Beshay, and A. D. Gosman, "Solution of the implicitly discretised reacting flow equations by operator-splitting," *Journal of Computational Physics*, vol. 93, no. 2, pp. 388–410, Apr. 1991.

[96] O. Ubbink, "Numerical prediction of two fluid systems with sharp interfaces," Imperial College of Science, Technology and Medicine, London, 1997.

[97] J. S. Leclerc and E. Ruiz, "Porosity reduction using optimized flow velocity in Resin Transfer Molding," *Composites Part A: Applied Science and Manufacturing*, vol. 39, no. 12, pp. 1859–1868, Dec. 2008.

[98] V. Rohatgi, N. Patel, and J. Lee, "Experimental investigation of flow-induced microvoids during impregnation of unidirectional stitched fiberglass mat," *Polymer Composites*, vol. 17, no. 2, pp. 161–170, Apr. 1996.

[99] D. J. Inman, *Engineering Vibration, Second Edition*. Prentice Hall, 2000, p. 621.

[100] P. Macioce, "Viscoelastic Damping 101," *Sound and Vibration*, vol. 37, no. 4, pp. 8–10, 2003.

[101] E. Reynders, "System identification methods for (operational) modal analysis: Review and comparison," *Archives of Computational Methods in Engineering*, vol. 19, no. 1, pp. 51–124, Feb. 2012.

[102] P. Mohanty and D. J. Rixen, "Operational modal analysis in the presence of harmonic excitation," *Journal of Sound and Vibration*, vol. 270, no. 1–2, pp. 93–109, Feb. 2004.

[103] L. Hermans and H. Van der Auweraer, "Modal testing and analysis of structures under operational conditions: industrial applications," *Mechanical Systems and Signal Processing*, vol. 13, no. 2, pp. 193–216, 1999.

[104] M. Dohler, P. Andersen, and L. Mevel, "Operational modal analysis using fast stochastic subspace identification method," in *Proceedings of the 30th International Modal Analysis Conference (IMAC)*, 2012, pp. 1–7.

[105] R. Brincker and P. Andersen, "Understanding stochastic subspace identification," in *Proceedings of the 24th International Modal Analysis Conference (IMAC)*, 2006, pp. 1–6.

[106] X. Xie, Y. Mai, and X. Zhou, "Dispersion and alignment of carbon nanotubes in polymer matrix: A review," *Materials Science and Engineering: R: Reports*, vol. 49, no. 4, pp. 89–112, May 2005.

[107] A. D. Wright, C. E. Smith, R. W. Thresher, and J. L. C. Wang, "Vibration modes of centrifugally stiffened beams," *Journal of Applied Mechanics*, vol. 49, no. 1, pp. 197–202, 1982.

[108] N. Granick and J. E. Stern, "Material damping of aluminum by a resonant-dwell technique," Greenbelt, Maryland, 1965.

[109] W. E. Baker, W. E. Woolam, and D. Young, "Air and internal damping of thin cantilever beams," *International Journal of Mechanical Sciences*, vol. 9, pp. 743–766, 1967.

[110] J. M. Lee and K. G. McConnell, "Experimental cross-verification of damping in three metals," *Experimental Mechanics*, vol. 15, no. 9, pp. 347–353, 1975.

[111] K. Gupta and S. P. Singh, "Damping measurements in fiber reinforced composite rotors," *Journal of Sound and Vibration*, vol. 211, no. 3, pp. 513–520, 1998.

[112] J. Kielb and R. Abhari, "Experimental study of aerodynamic and structural damping in a full-scale rotating turbine," *ASME Journal of Engineering for Gas Turbines and Power*, vol. 125, pp. 102–112, 2001.

[113] H. H. Yoo, R. R. Ryan, and R. A. Scott, "Dynamics of flexible beams undergoing overall motions," *Journal of Sound and Vibration*, vol. 181, no. 2, pp. 261–278, Mar. 1995.

[114] Z. Fan, P. Tsakiropoulos, and A. P. Miodownik, "A generalized law of mixtures," *Journal of Materials Science*, vol. 29, no. 1, pp. 141–150, 1994.

[115] G. Sauer and M. Wolf, "Finite element analysis of gyroscopic effects," *Finite Elements in Analysis and Design*, vol. 5, pp. 131–140, 1989.

[116] C. Johnson, *Numerical Solution of Partial Differential Equations by the Finite Element Method*. Mineola, New York: Dover Publications, 2009, p. 288.

[117] J. Yu and A. Craggs, "3-D solid finite element modeling of rotating shafts," in *Proceedings of the International Modal Analysis Conference*, 1997, vol. 11, no. 8–10, pp. 1488–1494.

[118] S. K. Clark, *Dynamics of Continuous Elements (Prentice-Hall international series in dynamics)*. Prentice Hall, 1972, p. 272.

[119] J. Chung and G. M. Hulbert, "A time integration algorithm for structural dynamics with improved numerical dissipation: the generalized-α method," *Journal of applied mechanics*, vol. 60, no. 2, pp. 371–375, 1993.

[120] G.-P. Cai, J.-Z. Hong, and S. X. Yang, "Model study and active control of a rotating flexible cantilever beam," *International Journal of Mechanical Sciences*, vol. 46, no. 6, pp. 871–889, Jun. 2004.

[121] M. S. Selig, "UIUC Airfoil Coordinates Database," 2012. [Online]. Available: http://www.ae.illinois.edu/m-selig/ads/coord_database.html#X. [Accessed: 01-Jun-2012].

[122] J. Jonkman, S. Butterfield, W. Musial, and G. Scott, "Definition of a 5-MW reference wind turbine for offshore system development," Golden, Colorado, 2009.

[123] W. A. Timmer and R. P. J. O. M. van Rooij, "Summary of the Delft University wind turbine dedicated airfoils," *ASME Journal of Solar Energy Engineering*, vol. 125, pp. 488–496, 2003.

[124] T. Lutz, A. Wolf, W. Wurz, and J.-G. Jeremiasz, "Design and verification of an airfoil with trailing-edge flap and unsteady wind-tunnel tests," Stuttgart, Germany, 2011.

[125] C. Ashcraft, R. Grimes, D. Pierce, and D. Wah, "The user manual for SPOOLES, release 2.0: An object oriented software library for solving sparse linear systems of equations." Boeing Shared Services Group, Seattle, WA 28124 USA, 1998.

[126] P. Pedersen, "Analytical stiffness matrices with Green-Lagrange strain measure," *International Journal for Numerical Methods in Engineering*, vol. 62, no. 3, pp. 334–352, Jan. 2005.

[127] F. J. McHugh and J. Shaw, "Helicopter vibration reduction with higher harmonic blade pitch," *Journal of the American Helicopter Society*, pp. 26–35, 1978.

[128] A. D. de Corcuera, A. Pujana-Arrese, J. M. Ezquerra, E. Segurola, and J. Landaluze, "H∞ based control for load mitigation in wind turbines," *Energies*, vol. 5, no. 4, pp. 938–967, Apr. 2012.